POLITECNICO DI MILANO

Scuola di Ingegneria Industriale e dell'Informazione

Corso di Laurea Magistrale in
Ingegneria Energetica

Modeling soot emissions in Diesel Engines by means of semi-empirical approaches and a combustion model based on detailed chemistry

Relatore: Prof. Tommaso LUCCHINI

Tesi di Laurea di:

Stefano MARANTA Matr. 801015

Chiara TANELLI Matr. 799623

Anno Accademico 2013 - 2014

Stefano Maranta, Chiara Tanelli: *Modeling soot emissions in Diesel Engines by means of semi-empirical approaches and a combustion model based on detailed chemistry* |
Tesi di Laurea Magistrale in Ingegneria Energetica, Politecnico di Milano.
Tesi redatta con LaTeX
Aprile 2015.

Politecnico di Milano: www.polimi.it

Scuola di Ingegneria Industriale e dell'Informazione: www.ingindinf.polimi.it

Contents

List of Figures

List of Tables

Abstract

In this work, three semi-empirical soot models, namely the models proposed by Moss, Lindstest-Leung and Wen, have been implemented in the Lib-ICE library, developed for internal combustion engine simulations by the ICE group of Politecnico di Milano and based on the open-source CFD code OpenFOAM. The pre-existing Representative Interactive Flamelet (RIF) combustion model, developed for Diesel combustion, has been extended to account for the flamelet equations for soot with source terms evaluated according to the selected soot models.

Validation was first carried out in a constant volume vessel for different ambient conditions (temperature, oxygen concentration and density), which reproduce the typical operating conditions of a Diesel engine, comparing computed results with data provided by Sandia National Laboratories. Then the models have been tested in a single cylinder research engine derived from a 2-L series PSA engine with different injection strategies obtained by incrementing the fuel mass of the post injection event and keeping the total fuel mass injected constant.

The simulations carried-out in the constant volume show that two of the implemented models, are able to correctly predict soot trends. Encouraging results have been obtained with an improved RIF model, the Eulerian Particle Flamelet model, which better describe the features of Diesel combustion compared to a single flamelet approach. Unfortunately, no such good results have been achieved for engine simulations. The main presumed reason for this behaviour is that the spray model cannot reproduce the correct air/fuel mixture, proving that for an accurate prediction of soot, all the previous processes that occur in Diesel combustion must be carefully modelled.

Key words: CFD, soot, RIF, combustion, Diesel

Sommario

Lo scopo di questo lavoro consiste nell'implementazione dei tre modelli semi-empirici proposti da Moss, Lindstedt-Leung e Wen per la previsione del soot prodotto in una combustione Diesel. Tali modelli sono stati integrati nella Lib-ICE, libreria basata sul codice open-source OpenFOAM e sviluppata dal gruppo ICE del Politecnico di Milano per la simulazione di motori a combustione interna. Il pre-esistente modello di combustione basato sulla cosiddetta flamelet assumption e denominato Representative Interactive Flamelet (RIF) è stato modificato per includere le equazioni per il soot con i termini sorgente definiti secondo i modelli sopra elencati.

Una prima validazione di questi modelli è stata effettuata in camera a volume costante per differenti condizioni ambiente (temperatura, concentrazione di ossigeno e densità), prossime a quelle operative effettive di un motore Diesel. I risultati ottenuti sono stati confrontati con le rilevazioni sperimentali eseguite dai Sandia National Laboratories. Successivamente, i modelli sono stati testati su un motore monocilindro derivato dalla serie 2-L del motore PSA con differenti strategie d'iniezione ottenute incrementando la massa di combustibile della post-iniezione, mantendo invariata la massa totale iniettata.

Dalle simulazioni in camera a volume costante si è potuto osservare che tutti i modelli, ad esclusione di quello di Wen, predicono correttamente l'andamento del soot al variare delle condizioni operative. Risultati promettenti sono stati ottenuti usando un modello di combustione RIF avanzato, chiamato Eulerian Particle Flamelet, in grado di meglio riprodurre la struttura della fiamma tipica della combustione Diesel rispetto a un modello più semplice a singolo flamelet. Purtroppo, risultati altrettanto buoni non sono stati raggiunti per le simulazioni nel motore e si presume che ciò sia principalmente dovuto alla difficoltà del modello di spray di combustibile di riprodurre la corretta miscela aria/combustibile, evidenziando la necessità di un'attenta modellizzazione di tutti i processi coinvolti nella combustione Diesel per poter avere previsioni accurate di soot.

Parole chiave: CFD, soot, RIF, combustione, Diesel

Introduction

In the last decade, the European automotive market share of Diesel vehicles has seen a growing trends and today it is settled at more than 50%. The main reason of Diesel engine success is due to its high efficiency energy conversion, reliability and durability, high driveability and low production and maintenance costs. Unfortunately, the Diesel spray combustion is affected by significant in-cylinder emissions due to rich and lean mixture zones leading to large amounts of soot and nitrogen oxides.

Recently, a more stringent legislation for pollutant emissions has led towards a deeper understanding of combustion and emission phenomena in order to develop new in-cylinder strategies and aftertreatement devices. This research work is carried out on two different but related fronts: on one hand, experimental measurements provide data for diesel engine relevant conditions and, on the other, Computational Fluid Dynamics (CFD) simulations represent a backup for industrial research and development and help experimental research in understanding the physical processes, especially those unlikely measurable.

The Engine Combustion Department of the Sandia National Laboratories (SNL) has maintained the Energy Combustion Netwok (ECN) with the aim to provide a common platform for the comparison of numerical as well as experimental activities from different groups worldwide focusing on well defined target conditions. Recently, accurate in-cylinder soot data has been provided by new diagnostic devices and techniques.

On modeling side, several approaches have been developed for soot formation and oxidation but the most widely used are the semi-empirical correlations. Indeed, these models are intuitive as they trace the physics of soot but can be used for conditions close to those that they have been developed for. Nonetheless, the applicability domain can be extended by setting the values of reaction rates constants for the new conditions simulated. Two-equations soot models are largely used for CFD applications, where transport equations for the soot mass and number density are resolved and among these the most prominent are the models of Moss [1], Lindstedt-Leung [2, 3] and Brookes [4].

Independently from the kind of model used, modeling of soot formation and oxidation, particularly in Diesel engines, is an extremely challenging task, as soot processes are heavily affected by previous processes, e.g. liquid spray atomization, fuel evaporation, fuel/oxidizer mixing, autoignition and flame characteristics and soot precursor evolution. Therefore, for an accurate prediction of soot behaviour all the aforementioned processes must be accurately described. To account for detailed chemistry, necessary to correctly predict the species involved in soot formation and oxidation, the flamelet approach for Diesel spray turbulent combustion modeling

seems to be the most adequate. In particular, the Representative Interactive Flamelet (RIF) model allows to account in detail for both fluid dynamics and chemistry since the respective time scales are decoupled and to consider turbulence-chemistry interaction too.

The object of this work is to simulate soot formation and oxidation at Diesel engine conditions. The semi-empirical soot models of Moss, Lindstedt and Brookes in the version modified by Wen [5] have been implemented in the Lib-ICE library, developed for internal combustion engine simulations by the ICE group of Politecnico di Milano and based on the open-source CFD code OpenFOAM. The pre-existing RIF model has been extended to account for the two flamelet equations for soot with source terms evaluated according the the soot model listed above.

The validation of the soot models has been first carried out in constant volume vessel by varying operating conditions, namely ambient temperature, oxygen concentration and density, and by comparing computed results with measured values provided by ECN. Indeed, experimental and modelling investigations have shown that there are negligible differences between the fuel Diesel vaporization, autoignition and combustion processes occurring in the combustion vessel at engine operating conditions and those in the real Diesel engine [6].

Then, the validation has been performed in a single cylinder research engine derived from a 2-L series PSA engine with different injection stategies obtained by increasing the fuel mass of the post injection event and keeping the total fuel mass injected constant.

This work is organized in seven chapters. In chapter 1, phenomenological descriptions of Diesel spray combustion based on the conceptual model of Dec [7] and soot processes are provided. The last part of this chapter focuses on formation and oxidation of soot in Diesel engine and on parameters that influences those processes. Chapter 2 presents the Diesel engine combustion modeling used in the simulations performed with a brief highlight on RIF model. In chapter 3 the semi-empirical soot model of Moss, Lindstedt-Leung and Brookes-Wen and the soot flamelet equations are described. In chapter 4, the CFD library implemented for soot in the Lib-ICE framework, together with the RIF solver, is presented. Chapter 5 describes the experimental devices and data and the CFD case set-up. In chapters 6 and 7, results of the soot model validations respectively in the constant volume vessel and in the research engine are discussed.

Chapter 1

Phenomenological description of the soot processes

This chapter deals with the phenomenological description of the soot processes. First, Diesel combustion fundamentals are presented, since the way wherewith soot is formed and oxydized is tightly related to the kind of combustion regime. Then, a general description of the soot fundamentals is given, followed by an insight of soot in Diesel engine, with a focus on the influence of the lift-off length and of the main ambient factors (temperature, oxygen concentration and density).

1.1 Diesel combustion fundamentals

In Diesel engines, the fuel is directly injected in the combustion chamber as the piston approaches top dead centre (TDC). The compression heats the air to such a high temperature that auto-ignites the fuel when it is injected. For this reason, Diesel engines are also named as *direct injection compression-ignited* (DICI) engines. Modern strategies of Diesel combustion, for example HCCI and PCCI, that aim to increase the efficiency and especially to reduce pollutants formation, work with the same principle although the injection of the fuel can be anticipated or delayed compared to conventional Diesel combustion [8].

Due to the presence of direct spray injection of liquid fuel, Diesel combustion is an extremely complex process consisting of many interactive physical processes: formation, atomization, penetration and diffusion of the spray; evaporation of the liquid fuel, interaction and mixing of gaseous fuel with the charge air and fuel oxidation chemistry. Thus, until a few years ago, prior to the relatively recent advent of advanced laser diagnostics, it was very difficult to investigate and to make detailed measurements of the events occurring within a reacting Diesel fuel jet [7]: methods that were utilized (high-speed backlight, schlieren and natural flame-emission cinematography and sampling probe data) have limited spatial resolution, are not species specific and are not quantitative. Therefore it was difficult to obtain a deep understanding of Diesel combustion from which to derive a conceptual model.

It is out of this work to explain the processes involving spray formation and all the related aspects. Nevertheless, it must be remarked that they have a relevant influence with respect to the evolution of combustion and especially the formation of

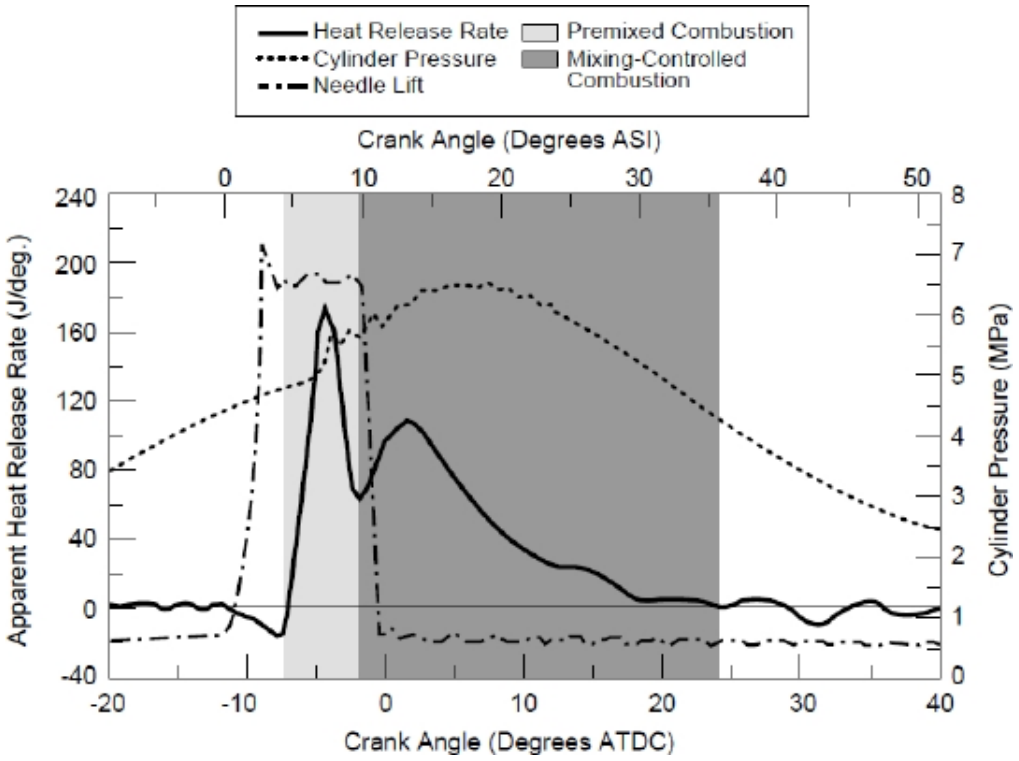

Figure 1.1. Ensamble-average of cylinder pressure, apparent heat release rate and injection needle lift for DI Diesel combustion reproduced from [7].

soot [9–15].

It is worth to describe how Diesel combustion occurs, presenting a conceptual model developed by Dec [7] in 1997, and focusing on processes that affect the formation and oxidation of soot. The conceptual model was the first to be derived by combining a wide variety of data on the Diesel combustion and emissions formation processes (vapour-fuel/air mixture images, PAH distribution images, relative soot concentrations, relative soot-particle distributions, images of the diffusion flame structure and natural-chemiluminescence images of the autoignition) obtained from multiple laser-based planar imaging and natural-flame emission diagnostics. The model applies to conventional Diesel conditions, having a single injection, little or no EGR, absence of flame/wall interaction and swirl and a negative dwell (time from the end of injection to ignition) with fuel injected shortly before TDC. Fuel injection is typically long enough that much of the fuel burns during mixing-controlled combustion, so that the jet experiences a significant "quasi-steady" period, when combustion and injection happens at the same time. However, the model can be extended to different conditions, i.e. low temperature combustion (LTC) conditions [8].

First, plots of the cylinder pressure, injector needle lift and apparent heat release rate (AHRR) for the operating conditions which refers the conceptual model have been reported in fig. 1.1.

Diesel combustion is commonly divided in two phases. Referring to the heat release rate curve, the initial sharp rise and fall is due to the rapid combustion of the fuel vaporised and premixed with air during the ignition delay period, and it is commonly named the *premixed burn*. The second and more wide pick is due to the

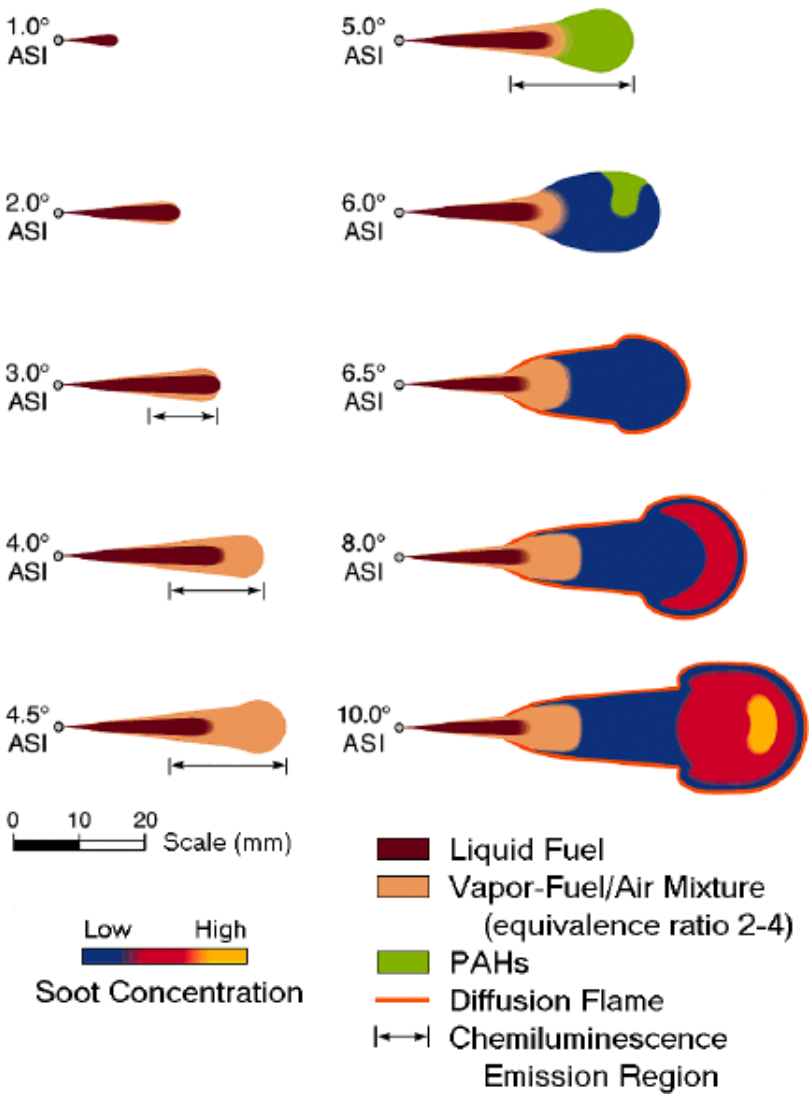

Figure 1.2. Schematic temporal sequence of DI Diesel combustion evolution from the SOI to the start of the mixing-controlled burn reproduced from [7]. The crank angle degree ASI is given at the side of each schematic.

mixing-controlled combustion, known as *mixing-controlled burn*. During this phase, fuel burns as enters the combustion chamber and combustion is regulated by the diffusion processes. The amount of energy release can be graduate with the control of the injection.

Figure 1.2 represents the conceptual model with a temporal sequence of schematics from the start of injection to the first part of the mixing-controlled burn.

The evolution of the flame structure is now briefly presented, focusing on soot evolution. In conventional DICI Diesel engines, fuel is injected at high pressures ($\sim$ 100 MPa) and, due to the break-up processes [13], forms a conical spray of droplets spreading from the hole of injector. Thus, the model provides a liquid fuel region (dark brown region in fig. 1.2) at the injector, but downstream air is entrained and fuel vaporizes. The thermal energy provided by the entrained in-cylinder gas heats and vaporizes the liquid fuel by this point. At 3°ASI the liquid fuel reaches

its maximum penetration, called the *liquid length* because the hot air entrained into the jet has been sufficient to vaporize all the fuel. For high-pressure Diesel injection, vaporization is limited by mixing (i.e. entrainment of hot air), not by droplet atomization and vaporization processes [8]. A region of fuel vapour forms along the edges of liquid spray and, after liquid length is reached, it continues to penetrate into the combustion chamber. The penetrating vapour develops a head-vortex (4.5°ASI) made by a roughly uniform rich fuel/air mixture with equivalence ratios ranging from about 2 to 4. After about 4.5°ASI chemiluminescence occurs, initially as weak signal, especially from regions along the edges of the spray and probably due in some cases to the phenomenon of the so called *cool flames* [16]; then, by 4.5°ASI, most of the chemiluminescence comes from the large region of vapour-fuel/air mixture in the leading portion of the jet. This indicates that auto-ignition, distributed throughout all this region, takes place, fuel breaks down and large poly-cyclic aromatic hydrocarbons (PAHs), soot precursors, appear (green and blue region in fig. 1.2). At this time the heat release curve increases and the premixed burn occurs volumetrically in the fuel rich region of the jet.

Since this combustion is rich, it produces small particles of soot and some fuel remains unconsumed. These rich products, mixing with the surrounding air, generate a thin diffusion flame (orange line in fig. 1.2) at the jet periphery positioned where the mixture is nearly stoichiometric and it extends upstream to a fixed distance from the nozzle tip, termed the *lift-off length* (LOL). As the diffusion flame is formed, larger particles of soot are detected in a thin layer around the jet periphery. As the premixed burn proceeds, soot concentration increases a lot in the leading edge of the jet due to the turbulent transport of particles produced by the diffusion flame. In the head vortex particles are also bigger than those formed along the diffusion flame.

With the transition to the mixing controlled burn, when the last premixed air is consumed, the structure of the jet does not change much. Figure 1.3 presents the image of conceptual model of mixing-controlled combustion prior to the end of injection.

It is interesting to observe that in this phase a rich premixed combustion remains just downstream of maximum liquid penetration. This combustion is similar to the initial premixed burn but is a little richer (equivalence ratio of 3 to 5) because the presence of the diffusion flame reduces the liquid length and the entrainment of air. It produces small particles of soot that grow moving towards the leading portion of the jet, along with the particles produced by the diffusion flame and transported inward in the head vortex. The diffusion flame is the only source of high OH radical concentrations [16] and, when soot reaches the flame, it is oxidized by the OH, which is the principal soot oxidizer.

1.2 Soot fundamentals

Soot is a solid substance consisting of roughly eight parts of carbon and one part hydrogen [17], although there is not a unique chemical and physical structure [3]. Just formed, soot particles have a C/H ratio lower than one but as soot evolves, it loses the greater part of hydrogen. Soot density is reported from different works varying from about 1.8 g/cm^3 to 2 g/cm^3 [14, 18].

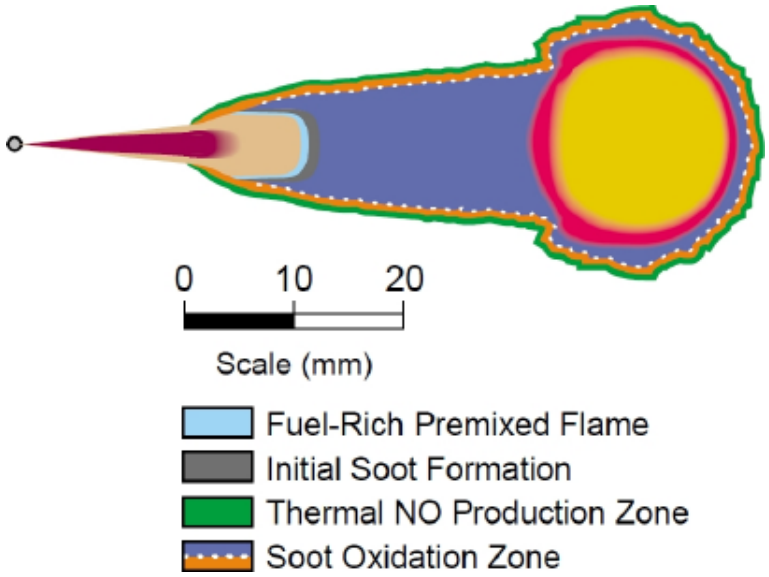

Figure 1.3. A schematic of the conceptual model for the quasi-steady (prior the end of injection) mixing-controlled reproduced from [7]. The color coding not shown in this figure is the same as that given in fig. 1.2.

Soot is formed from unburned fuel, which nucleates from the vapour phase to a solid phase in fuel-rich regions at elevated temperature during pyrolysis or combustion of hydrocarbons. It is by now widely accepted that PAHs play a determinant role in its formation. It is obvious that the conversion of a hydrocarbon fuel molecule containing few carbon atoms into a solid carbonaceous agglomerate with some millions of carbon atoms is an extremely complicated phenomenon that involves a highly large number of chemical and physical processes [3]. Particulate matter (PM) discharged from Diesel engine is composed not only of soot, but typically less than 50% consists of other liquid or solid phase materials that are collected when exhaust gases pass through the filter (un/partially burned fuel/lubricant oil, bound water, wear metals and fuel-derived sulphate and nitrate) [13, 19, 20].

Net amount of soot formed is the result of competition between soot formation and oxidation [21]. Six processes are commonly identified in the description of net soot formation: pyrolysis with soot precursors generation, nucleation, coalescence, particle surface reactions, namely growth and oxidation, and particle agglomeration. Fig. 1.4 depicts schematically these processes for a premixed flame; oxidation is not shown since it operates at any stage of the sequence.

In non-homogeneous mixtures, e.g. diffusion flames, all chemical processes sketched roughly in figure are overlaid by the mixing of fuel and oxidizer. The interaction of mixing and chemical reactions under turbulent conditions is an additional problem connected with the technical application of combustion [3]. Thermodynamics alone cannot adequately describe soot formation phenomena since soot is formed beyond regimes where it is thermodynamically stable relative to the oxides of carbon. It is inherently a kinetically limited process [21].

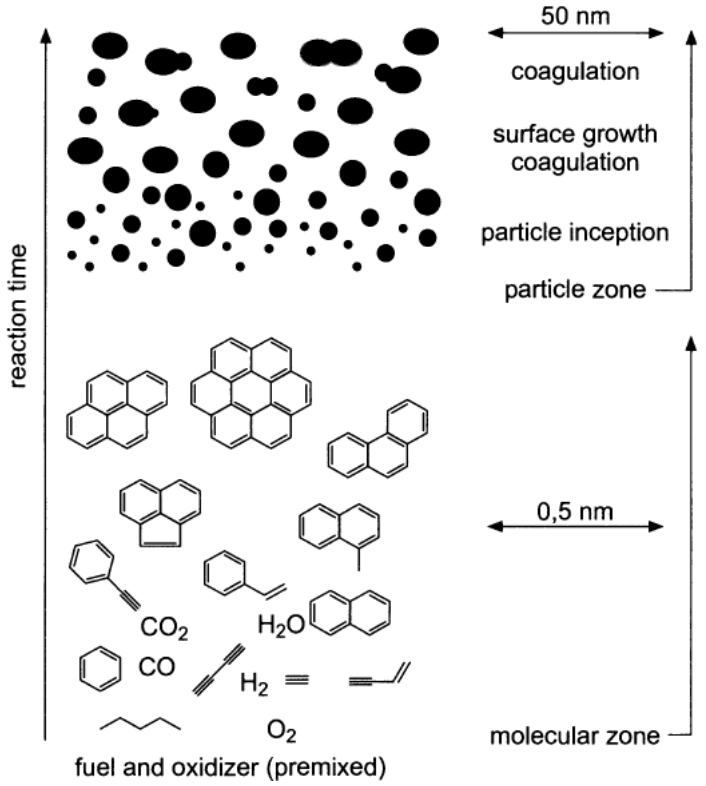

Figure 1.4. The schematic reaction path leading to soot formation in premixed flames reproduced from [3].

1.2.1 Fuel pyrolysis and formation of soot particles precursors

As hydrocarbons pyrolyse, they primarily produce smaller hydrocarbons, in particular acetylene (C_2H_2), and radicals, but Haynes and Wagner [22] list also C_2H_4, CH_4, C_3H_6 and C_6H_6 as typical pyrolysis products in laminar diffusion flames. The initial step in the production of soot is the formation of the first aromatic ring from these pyrolysed aliphatic hydrocarbons, that is the rate limiting step in the reaction sequence to larger aromatics [23] and determines the amount of soot formed. Indeed, experimental measurements have shown that fuels containing a certain amount of aromatics produce more soot since aromatics rings are already present [5]. First ring formation is subjected to dispute in literature and has alternative routes that depend on temperature and initial fuel type. It is not the matter of this work to deepen the chemistry of aromatic rings formation and their growth to PAHs. Therefore, only the two pathways that seem to have a dominant role will be presented: the first one merely involve the propargyl radical (C_3H_3), a very stable hydrocarbon radical, whereas the second considers the acetylene (C_2H_2), the most abundant "building block" [23]:

$$C_3H_3 + C_3H_3 \rightarrow \text{benzene or phenyl} + H \tag{1.1}$$

$$C_3H_3 + C_2H_2 \rightarrow c{-}C_5H_5. \tag{1.2}$$

In general, in addition to this route of cyclization of chain molecules into rings structures, Bryce et al. [24] propose other two routes: a direct path where aromatic

rings dehydrogenate at low temperature and break-up and recyclization of rings at higher temperature.

When the first aromatic rings are formed, they growth to larger PAHs through the H-abstraction-C_2H_2-addition (HACA) sequence, in which, thanks to reaction with H radical, aromatic rings dehydrogenate and the addition of a gaseous acetylene molecule increases the size of aromatic structure (for more details see [3, 14, 23, 25]. There are many other reactions and species that are involved in the growth of aromatics, especially beyond four aromatic rings, resulting in soot particles of different structure and size [14].

1.2.2 Particle nucleation

Nucleation or soot particle inception is the formation of primary identifiable solid particles ($\simeq$1.5-2 nm), named usually nuclei. This process is probably the least understood among the ones involved in the soot formation. In general, it may be considered that nuclei appear as PAHs add sufficient mass and their structure extends in three dimensional space. Frenklach [23] retains that above a certain size, PAHs collide each other and form dimers or trimers and so on and this marks the outset of solid phase. In this way it takes into account not only the amount of soot mass but also particles size and the time scale of soot inception phenomena.

Nucleation temperature varies according to different works from 1300 K to 1600 K [17]. Soot nuclei formed give a negligible contribution to the total soot mass produced, but do have a significant influence on the mass added later, because they provided active sites for surface growth.

1.2.3 Surface growth

Total soot mass formed is almost exclusively determined by surface reactions: growth and oxidation. It is widely accepted that acetylene is the principal gaseous species reacting at the particle surface, although other species (aromatics and PAHs) may play a role. The hypothesis of chemical similarity has been advanced by Frenklach [23]. According to it, processes of growth for PAHs and soot particle are analogous, namely the surface growth is assumed to be governed by the HACA mechanism. Abstraction of H atoms produces active sites with surface radicals that then react with acetylene but also with oxidizing agents. It is interesting to observe that surface growth rates are lower for larger particle [23], a phenomenon named *soot surface ageing*. This can be attributed to decrease in number of active sites probably due to the phenomenon called *surface migration* [23].

1.2.4 Coalescence and agglomeration

Once soot particles are formed, they collide each other to make larger particles. Experimental observations have shown than initially particles have spherical shape but later they acquire a fractal one. For this reason particle coagulation is divided into coalescent growth and agglomeration. During these phases, soot mass remain constant while the number of particles decreases.

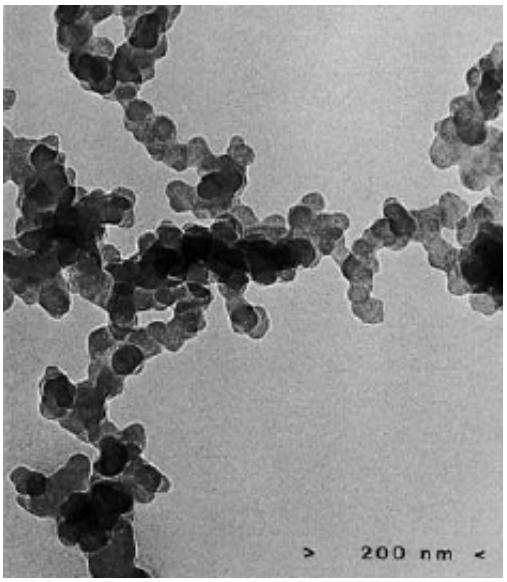

Figure 1.5. Photograph of a mature soot particle in a non-premixed flames reproduced from [28].

During coalescence, particles are yet small and two roughly spherical particles combine to form a single spherically shaped particle. The frequency of collisions determine the rate of coagulation, that assuming mono-disperse spherical particles, can be written as [26]:

$$\left(\frac{\partial n_{soot}}{\partial t}\right)_{coag} = \frac{1}{2} K n_{soot}^2 \tag{1.3}$$

where n_{soot} is the number density of soot particles and K is the coagulation rate constant. The expression of K depends on Knudsen number (ratio of the mean free path to the particle radius). With regard to soot particle coagulation, typically it is assumed that Knudsen number is high and coagulation is said to be in the free molecular regime [27], although this assumption is questionable, especially for high-pressure combustion [23]. In this case, the coagulation rate constant takes the form [26]:

$$K = 16 r^2 y \left(\frac{\pi \kappa T}{m}\right)^{\frac{1}{2}} \tag{1.4}$$

where r is the radius of the particles, κ is the Boltzmann constant, m is the particle mass, and y is a correction coefficient for inter-particle forces. When soot particles mature, agglomeration occurs [23, 28]. Primary particles stick together forming chain-like structures but maintaining their spherical form, as can be seen in figure 1.5. Deeper explanation of these processes can be found in [21, 23, 29].

Primary particle in exhaust gases from Diesel engines vary in size from 20 to 70 nm while chain-like structures sizes typically range from 100 nm to 2 µm [17].

1.2.5 Oxidation

As it was previously discussed, oxidation occurs during all phases of soot formation. Actually, it seems that oxidation of aromatic radicals happens in a different way

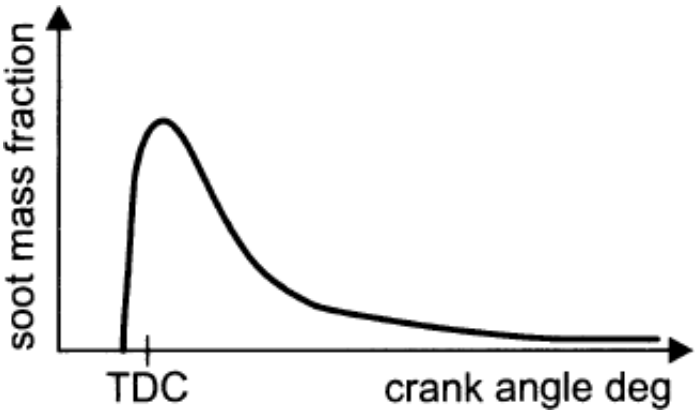

Figure 1.6. Qualitative soot history in DI Diesel engine reproduced from [14].

from that of soot. Indeed, oxidation of aromatics is principally due to O_2 attack, whilst oxidation by OH is rather unimportant [23]. For what concerns soot particles, although this process is still poorly understood, OH radical is retained the most important oxidizing agent [30–32], especially under fuel-rich and stoichiometric conditions (and thus on the fuel side of a diffusion flame), while under lean conditions soot is oxidized by both OH and O_2 [17].

Oxidation is a surface process, in which at first the oxidizer reacts with the radical active site (absorption) and then products (likely CO) leave the surface (desorption).

Few studies state that soot oxidation takes place at temperatures greater than 1300 K [17] and about 10-20% of all OH collisions with soot particles effectively produces a surface reaction. It is important to underline how both pyrolysis/nucleation and oxidation rates increase with temperature, but oxidation rate increases faster. This explains why, with increasing temperature in premixed flame, the soot yield reduces. This is not true for diffusion flames in which the lack of oxygen at the fuel side limits the increase of oxidation rate.

1.3 Soot in DI Diesel engines

After soot is formed and its oxidation has started as a result of entrained air in the rich zones, decrease in temperature below 1300 K-1400 K, due to the expansion and valves opening, and in concentrations of OH-radicals and O-atoms causes an interruption of the oxidation of soot. Figure 1.6 shows a typical trend of soot mass fraction within a Diesel engine. Normally, at least 90% and often up to 99% of the formed soot is oxidized again such that the soot concentration in the exhaust gas is only a small fraction of the maximum in-cylinder concentration during combustion [14].

A kinetic analysis conducted by Flynn et al. [33] showed how products of fuel pyrolysis are small, partially burned fragments of hydrocarbons of C4 or smaller in size like C_2H_2, C_2H_4 and C_3H_3. After about 0.1 ms, first indications of soot small particles occur over this entire volumetric region, suggesting the early soot is formed in a rich premixed reaction. During this time all processes conducting to nucleation of soot described before take place. As these rich products form the thin diffusion flame at the perimeter, larger soot particles and a higher soot concentration are

detected along the sides of the jet and especially in the recirculating head vortex where particles have time to grow to a very large size. This is because, as soot and unburned fuel move downstream in the jet, increase in temperature due to the diffusion flame, accelerates the reaction rates of surface growth. The higher concentration of soot in the transient head of the jet was noticed in many other experimental observations [6, 34].

Figure 1.7 shows simultaneous luminosity images and planar laser induced incandescence (PLII) images acquired at specific times after the start of injection (ASI) at the top and time-resolved KL profiles, proportional to the soot volume fraction (f_v) (see chapt. 5), and the combustion vessel pressure rise at the bottom. In the luminosity and PLII images reference lines at axial distances of 18.3 mm and 50 mm respectively indicate the time-averaged, quasi-steady lift-off length (dashed vertical line) and the axial position of the laser beam for extinction measurements (solid vertical line). It is worth to explain the KL profiles in the light of soot evolution shown in PLII images. The KL rapid increase occurs between 0.9 ms and 1.3 ms when the wider soot region of the penetrating tip of the jet passes the extinction measurements location. After the head of the jet gets over the 50 mm axial position, the KL value drops and varies about a mean value until the end of injection, suggesting that a quasy-steady state has been reached. Fluctuations of KL in this quasi-steady state are due to variations in the soot concentrations and in the width of the sooting region at the extinction measurement location. Moreover, from 2.5 ms ASI the length of the sooting region does not change, suggesting that after 2.5 ms ASI any soot formed in the fuel jet is completely oxidized by an axial location where the quasi-steady flame length has been established [6]. Other experimental observations show that no soot is visible outside of the OH envelope indicating that soot is oxidized before exiting the flame [35].

After end of injection, Dec et al. in [36] have shown that jet is divided into smaller and smaller structures made by soot surrounded by OH. As combustion proceeds, OH distributes throughout the structures and typically OH signal prevails until all indication of soot is gone.

1.3.1 Influence of the lift-off length on soot formation

The lift-off length is the determinant characteristic of the flame structure in respect to soot formation. Upstream the lift-off length, charge air is entrained into the fuel jet forming a rich partially premixed mixture prior to any combustion. The equivalence ratio of this premixed region, that is the amount of oxygen entrained, is determined by the lift-off length and it has been observed that soot and rich products form here. When soot is not produced in the rich premixed zone, it is also not produced further downstream as the rich products react in the diffusion flame [17, 34, 37]. The more the lift-off length increases, the more the fuel-air mixture in premixed region becomes less fuel-rich (with equal EGR) forming a smaller amount of soot [6]. As LOL increases, more air is entrained in the jet and the premixed stage assumes a significant role in the overall combustion process. Several works have shown that if the average equivalence ratio at the lift-off length, Φ_H, is minor to 2, no soot is formed in the jet [6, 37–39].

At last, it is important to observe that, as it can be seen from fig. 1.7, the location,

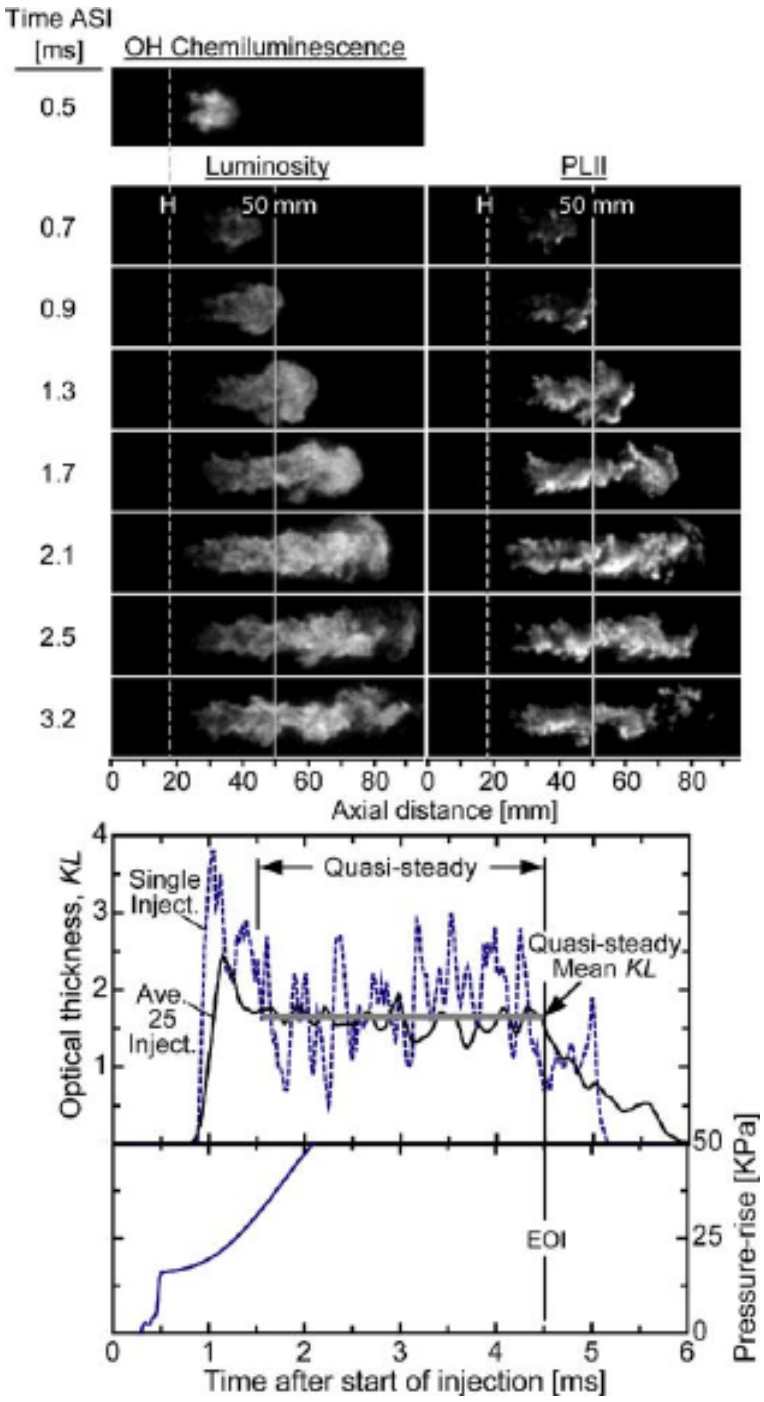

Figure 1.7. PLII images acquired at specific times after the start of injection (ASI) at the top and time-resolved KL profiles and the combustion vessel pressure-rise at the bottom reproduced from [6]. The lift-off length and x = 50 mm positions are shown on the images with vertical dashed and solid lines, respectively. KL measurements are shown for a single injection event as a dashed line and for the average of 25 separate injection events as a solid line. The mean KL value during the quasi-steady period of the fuel injection is represented by the horizontal solid gray line.

where the initial combustion and soot formation occur during the transient premixed combustion phase (0,5 ms), is slightly downstream of the quasi-steady LOL location. Thus, the equivalence ratio of the initial mixture burning during premixed burn has almost the same value of Φ_H during quasi-steady combustion. Fuel jets that produce no soot during transient period show the same behaviour at quasi-steady stage [6]. All parameters that influence lift-off length have consequently an indirect control on soot formation.

1.3.2 Ambient gas temperature

In fig. 1.8a the axial distribution of average f_v is shown for a Diesel jet in a constant-volume vessel at different ambient temperatures, with LOL (H) and Φ_H [6]. Increasing temperature causes a decrease in LOL, due to a major reactivity of the premixed gases which react closer to the injector, and an increase in the equivalence ratio at LOL. This determines a production of soot nearer to the injector in a fuel richer region and then a higher soot mass yield.

There is also a direct effect of temperature on soot chemistry. An increase in temperature of the sooting region, combined with a higher value of Φ_H, determines a rise of the soot formation rate but also a higher increase in oxidation rate, that is reflected by the shift of the f_v peak towards the injector. This suggest that soot oxidation dominates on soot formation further upstream for higher ambient temperature.

1.3.3 Ambient oxygen concentration

Studying the influence of ambient oxygen concentration on soot formation allows to understand how exhaust gas recirculation (EGR) [13] affects Diesel engine PM emissions, although, as mentioned before, processes of late soot oxidation during expansion stroke are crucial on net amount of engine-out PM [40].

Decreasing ambient oxygen concentration, LOL and flame length increase but the equivalence ratio at LOL location remains almost the same [17, 38–40]. This occurs because a longer LOL allows a higher air mass entrained in the fuel jet, compensating the smaller oxygen concentration. In fig. 1.8b trends of axial KL are shown for n-heptane in a constant-volume vessel obtained by Idicheria and Pickett [40]. They have observed that decreasing oxygen concentration causes a predominance of the soot formation over the soot oxidation for a longer distance from the injector, because of the decrease in flame temperature. Stretching and downstream shift of the soot-forming regions are likely due to the reduced rate of oxygen entrainment into the fuel jet, caused by a higher $(A/F)_{st}$. At same time the diminution in temperature causes a reduction in formation and oxidation rates with a KL peak gradually smaller. The overall result is that the total soot mass yield in the jet shows a non-linear trend with EGR: initially increases as O_2 decreases and then diminishes (the peak is near 15% O_2 condition). In conclusion, as discussed above, this is due to a competition between residence time, which increases when O_2 is decreased, and temperature, which decreases with decreasing O_2 [17, 40].

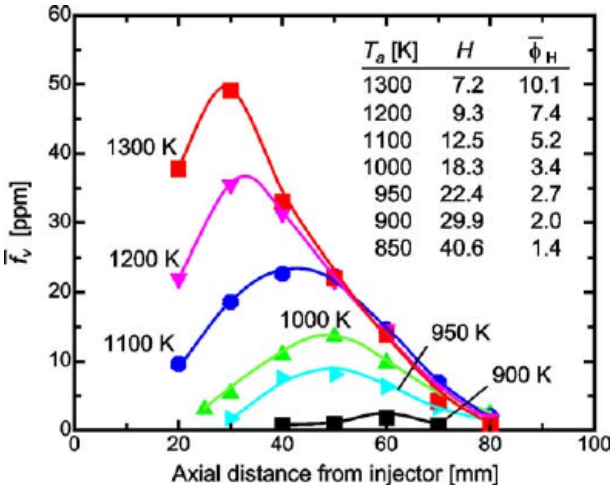

(a) Averaged soot volume fraction along the axis for different ambient temperatures.

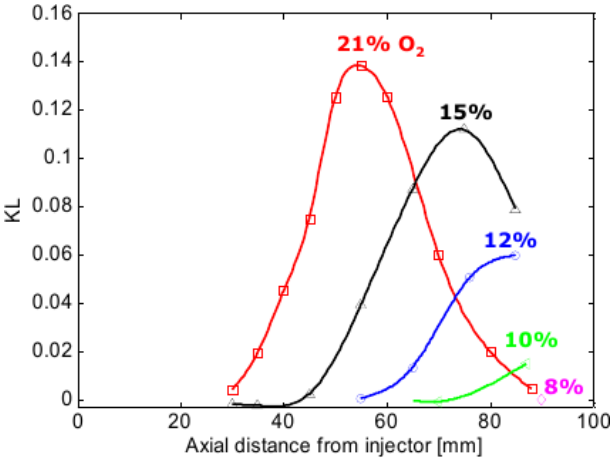

(b) Axial KL measurement at different ambient concentrations.

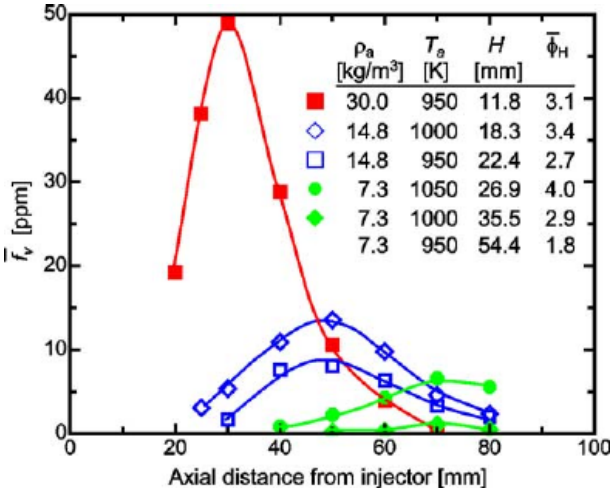

(c) Averaged soot volume fraction along the axis for different ambient densities.

Figure 1.8. Averaged soot axial measurments for different ambient conditions reproduced from [6]. The table on the top right corner indicate for each condition the corresponding LOL (H) in mm and the equivalent ratio at LOL location.

1.3.4 Ambient gas density

Increasing ambient density produces a strong reduction of the LOL [6, 34] but at the same time an increase in the rate of ambient gas entrainment [6, 17]. The net result is a decrease in the amount of air entrained at the lift-off length, i.e. an increment in Φ_H, as can be seen in figure 1.8c. A decrease in ambient gas density causes a large decrease in the peak soot volume fraction (and in total soot mass yield) for a fixed ambient temperature, since leaner mixture forms at LOL but also because lower density prevent rapid soot formation kinetics since collisions occur less frequently. This is proved by also the observation that the distance between LOL and the on-set of soot is reduced at higher densities [34]. A shift of soot processes farther downstream with decreasing density is noticed and this is due to the increase in LOL and the decrease in overall air entrainment. The latter factor explains also the increasing flame length with lower density. Finally, Pickett and Siebers have shown in [6] how there is a strong non-linear effect of density on soot. In fact the increase in soot with increasing ambient density is greater than would be expected due simply to the increase in total number density that occurs with increasing ambient gas density.

Chapter 2

Diesel engine combustion modeling

Before presenting the soot models used in this work, a brief description of how Diesel combustion is modelled is needed. Indeed, as it happens for physical phenomena outlined in the previous chapter, soot prediction relies on combustion calculations. Therefore, accurate combustion model represents the basis for valuable soot results.

In the first part, general governing equations for reacting flows are introduced, followed by a synthetic description of the employed computational method to account for turbulence-combustion interaction.

At last, the Representative Interactive Flamelet model which constitutes the frame for the implementation of the soot models is described.

2.1 Governing equations for combusting flows

The governing equations are mathematical statements of physical conservation laws of mass, momentum and energy and completely describe a physical system. The equation system for combusting flows differs from the usual Navier-Stokes equation system for non-reacting flows and equations themselves have different or additional terms. The peculiarity of reacting flows is a changeable composition according to chemical reaction rates. This is expressed by mass conservation equations for each species, causing an increase in the number of equations to be solved proportional to the number of species involved.

Before presenting the system of equations, it is worth to highlight that conservation equations are often written in a differential form and they are of a kind of transport equations with convective and diffusion terms. For a general scalar quantity φ, the transport equation assumes the following form:

$$\frac{\partial \rho\varphi}{\partial t} + \nabla \cdot (\rho\varphi\mathbf{u}) = \nabla \cdot (\Gamma \nabla\varphi) + S_\varphi \tag{2.1}$$

The terms on the left hand side are the rate of change term and the convective term, whereas on the right hand side diffusion term and source term are the first term and the second term respectively.

All conservation equations are referred to the gas phase. Since in Diesel combustion the spray evolution should be considered, source terms due to liquid/gas

interaction are present in the equations and they will be briefly explained later. The compact suffix notation of the conservation equations for three-dimensional, unsteady, compressible, reacting fluid flow is reported below:

$$\frac{\partial \rho}{\partial t} + \frac{\partial \rho u_i}{\partial x_i} = \rho \dot{S}_\rho^{\,\mathrm{evap}} \tag{2.2}$$

$$\frac{\partial \rho u_j}{\partial t} + \frac{\partial \rho u_i u_\mathrm{j}}{\partial x_i} = -\frac{\partial p}{\partial x_i} + \frac{\partial \tau_{ij}}{\partial x_i} + \rho g_\mathrm{j} + f_\mathrm{j}^{\,\mathrm{evap}} \qquad j = 1,2,3 \tag{2.3}$$

$$\frac{\partial \rho h}{\partial t} + \frac{\partial \rho u_i h}{\partial x_i} = \frac{Dp}{Dt} - \frac{\partial \dot{q}_i}{\partial x_i} + \tau_{ij}\frac{\partial u_i}{\partial x_j} + \dot{q}_\mathrm{evap} - \dot{q}_\mathrm{rad} \tag{2.4}$$

$$\frac{\partial \rho y_k}{\partial t} + \frac{\partial \rho u_i y_k}{\partial x_i} = \frac{\partial}{\partial x_i}\left(\rho D_k \frac{\partial y_k}{\partial x_i}\right) + \dot{\omega}_k \qquad k = 1, ..., N_{species} \tag{2.5}$$

In the set of equations above some source terms appear. $\dot{S}_\rho^{evap}$, f_j^{evap} e $\dot{q}_{evap}$ are source terms of mass, momentum and enthalpy respectively due to the presence of liquid phase and its evaporation. $\rho\bar{g}$ is a momentum source term due to the gravity acceleration and is different from zero only for the momentum component in the direction along which acceleration acts. $\dot{q}_\mathrm{rad}$ is the radiative loss and $\tau_\mathrm{ij}\frac{\partial u_\mathrm{i}}{\partial x_\mathrm{j}}$ is a dissipation term owing to viscous stress. $\dot{\omega}_k$ is the volumetric reaction rate of generation or destruction of species k due to chemical reactions. The energy flux $\dot{q}_\mathrm{i}$ includes a heat diffusion term expressed by Fourier's law and a second term associated with diffusion of species with different enthalpies [41]. Both in this last term and in the diffusive term in the species mass equations, the diffusion velocity of a species is replaced with Hirschfelder and Curtiss approximation, where D_k is an equivalent diffusion coefficient of species k in the rest of mixture [41].

Assuming thermodynamic equilibrium, whereby the state of a substance is described by two state variable by means of equations of state, and a Newtonian fluid, for which the viscous stress is proportional to the gradient of velocity component, the system presented above is mathematically closed.

2.2 Computational method for turbulent combustion

The present study deals with turbulent combustion which results from the two-way interaction of chemistry and turbulence. On one hand, turbulence is influenced by high heat release rates which cause strong flow accelerations through the flame front and by severe changes in kinematic viscosity due to significant temperature variations. On the other hand, turbulence modifies the flame structure and enhances chemical reaction rates; particularly, in jet diffusive flames, turbulence is responsible for lift-off and blow-off phenomena, which occur for very high injection velocity.

A direct solution of the governing equations for turbulent combustion requires demanding computational costs; moreover, for most engineering problems, it is unnecessary to solve for turbulent fluctuations in detail. Therefore, approaches which resolve for mean quantities have been developed and widely used.

2.2.1 Reynolds Averaged Navier Stokes equations

In the present study, a Reynolds Averaged Navier Stokes (from now on abbreviated with RANS) approach is used. The RANS equations are obtained by averaging the instantaneous balance equations, defining a generic flow property $\varphi(t)$ as the sum of a steady mean quantity Φ and a time varying fluctuating component $\varphi'(t)$ with zero mean value:

$$\varphi(t) = \bar{\varphi} + \varphi'(t) \tag{2.6}$$

There are two possible methods for averaging equations: the Reynolds averaging, for constant density flows, and the Favre averaging, for variable density flows. If the Reynolds averaging is used for compressible flow, such as combusting flows, several terms due to correlation between density and velocity fluctuations appear, which have to be modelled. So, a mass-weighted average is preferred and the associated procedure is known as Favre averaging:

$$\varphi(t) = \tilde{\varphi} + \varphi''(t) \tag{2.7}$$

where

$$\tilde{\varphi} = \frac{\overline{\rho\varphi}}{\bar{\rho}} \tag{2.8}$$

With applying the latter averaging procedure to the instantaneous balance equations, the RANS equations follow:

$$\frac{\partial \bar{\rho}}{\partial t} + \frac{\partial \bar{\rho}\tilde{u}_i}{\partial x_i} = \bar{\rho}\widetilde{\dot{S}}_{\rho}^{\text{evap}} \tag{2.9}$$

$$\frac{\partial \bar{\rho}\tilde{u}_j}{\partial t} + \frac{\partial \bar{\rho}\tilde{u}_i\tilde{u}_\text{j}}{\partial x_i} = -\frac{\partial \bar{p}}{\partial x_j} + \frac{\partial \bar{\tau}_{ij}}{\partial x_i} - \frac{\partial \widetilde{\bar{\rho}u_j''u_i''}}{\partial x_i} + \bar{\rho}g_\text{j} + \tilde{f}_\text{j}^{\text{evap}} \qquad j = 1,2,3 \tag{2.10}$$

$$\frac{\partial \bar{\rho}\tilde{h}}{\partial t} + \frac{\partial \bar{\rho}\tilde{u}_i\tilde{h}}{\partial x_i} = \frac{\overline{Dp}}{Dt} - \frac{\partial \bar{\dot{q}}_i}{\partial x_i} - \frac{\partial \widetilde{\bar{\rho}u_i''h''}}{\partial x_i} + \widetilde{\dot{q}}_{\text{evap}} - \widetilde{\dot{q}}_{\text{rad}} \tag{2.11}$$

$$\frac{\partial \bar{\rho}\tilde{y}_k}{\partial t} + \frac{\partial \bar{\rho}\tilde{u}_i\tilde{y}_k}{\partial x_i} = -\frac{\partial \widetilde{\bar{\rho}u_i''y_k''}}{\partial x_i} + \widetilde{\dot{\omega}}_k \qquad k = 1,...,N_{species} \tag{2.12}$$

2.2.2 Closure models

Except for continuity equation, extra terms appear in the averaged flow equations, due to the interactions between various turbulence fluctuations. The accuracy and validity of the system's solution is therefore strictly limited by the closure models describing turbulence and combustion. The majority of these models are based on the physical effect of turbulence on mean flow properties: the presence of vortex eddy motions enhances transportation and mixing of momentum and energy and thus the associated unclosed terms are considered as source terms.

The term $\widetilde{u_j'' u_i''}$ is known as Reynolds stress because it represents the turbulent transport of momentum which accelerates slower moving fluid layers and decelerate faster ones. This term is generally modelled with Boussinesq approximation, which considers the Reynolds stress proportional to the mean rates of deformation:

$$\widetilde{\bar{\rho} u_j'' u_i''} = -\mu_t \left(\frac{\partial \tilde{u}_j}{\partial x_i} + \frac{\partial \tilde{u}_i}{\partial x_j} - \frac{2}{3} \delta_{ij} \frac{\partial \tilde{u}_k}{\partial x_k} \right) + \frac{2}{3} \bar{\rho} k \tag{2.13}$$

where μ_t is the turbulent or eddy viscosity, $k = \sum_{k=1}^{3} \frac{1}{2} \widetilde{u_j'' u_i''}$ is the turbulent kinetic energy and δ_{ij} is the Kronecker delta.

Turbulent transport of enthalpy, species mass and other scalar quantities can be modeled similarly with gradient diffusion assumption:

$$\widetilde{\bar{\rho} u_i'' \varphi''} = \Gamma_t \frac{\partial \tilde{\varphi}}{\partial x_i} \tag{2.14}$$

where Γ_t is the turbulent or eddy diffusivity.

In this work, the Reynolds analogy is adopted, which relates the value of the turbulent diffusivity with that of the turbulent viscosity through the turbulent Prandtl number, for enthalpy equation, or Schmidt number, for species mass fraction equations, defined as

$$\sigma_t = \frac{\mu_t}{\Gamma_t}. \tag{2.15}$$

Here $\mathrm{Pr_t}$ is set to 0.85.

It is now necessary to calculate μ_t. There are different approches but that used in this study is the two-equations model proposed by Jones and Launder, which is very popular for its semplicity and its cost effectiveness. The turbulent viscosity is estimated as

$$\mu_t = \bar{\rho} C_\mu \frac{k^2}{\varepsilon} \tag{2.16}$$

where k is the turbulent kinetic energy, defined above, and ε is its dissipation rate. k and ε are calculated solving a two-equations system, which is the mathematical representation of the Kolmogorov cascade [41]:

$$\frac{\partial \bar{\rho} k}{\partial t} + \frac{\partial \bar{\rho} \tilde{u}_i k}{\partial x_i} = \frac{\partial}{\partial x_i} \left[\left(\mu + \frac{\mu_t}{\sigma_k} \right) \frac{\partial k}{\partial x_i} \right] - \widetilde{\rho u_j'' u_i''} \frac{\partial \tilde{u}_i}{\partial x_j} - \bar{\rho} \varepsilon \tag{2.17}$$

$$\frac{\partial \bar{\rho} \varepsilon}{\partial t} + \frac{\partial \bar{\rho} \tilde{u}_i \varepsilon}{\partial x_i} = \frac{\partial}{\partial x_i} \left[\left(\mu + \frac{\mu_t}{\sigma_\varepsilon} \right) \frac{\partial \varepsilon}{\partial x_i} \right] - C_{\varepsilon 1} \frac{\varepsilon}{k} \widetilde{\rho u_j'' u_i''} \frac{\partial \tilde{u}_i}{\partial x_j} - C_{\varepsilon 2} \bar{\rho} \frac{\varepsilon^2}{k} \tag{2.18}$$

The model constants required to be tuned, especially for compressible flows. The values used in this study are listed in the table 2.1.

Table 2.1. Constants for the k - ε model.

C_μ	σ_k	σ_ε	$C_{\varepsilon 1}$	$C_{\varepsilon 2}$
0.09	1	1.4	1.55	1.92

2.3 Modeling of turbulent combustion

The closure of RANS equations needs turbulence models to deal with turbulent fluctuations and turbulent combustion models to describe chemical species conversion and heat release. Whereas the first ones have been previously presented, in the next paragraph the turbulent combustion model used in the performed simulations, namely the Representative Interactive Flamelet (RIF) model, will be briefly explained.

2.3.1 The RIF model

The Representative Interactive Flamelet (RIF) model is a method based on the so called *flamelet assumption*, firstly developed by Peters [42], and which matches the solution of the RANS equations with that of the flamelet equations, that will be presented in the following. The decoupling of the flow field and mixing problem, represented by the system of RANS equations, and the chemistry problem, accounted by flamelet equations, allows the use of detailed chemical mechanisms and avoid averaging the reaction rate.

The laminar flamelet concept

In [42], Peters explains that the laminar flamelet concept covers a regime in turbulent combustion where chemistry, as compared to transport processes, is fast enough that it occurs in thin layers, called flamelets, embedded within the turbulent flow fields, i.e. the laminar flame structure is stretched and distorted by turbulent eddies but is preserved. Thus, the flame can be treated as an ensable of laminar counterflow diffusion flamelets where chemical reactions occur. According to [43], in diffusive flames the fast chemistry assumption is a correct approximation, since the overall reaction rate is limited by species diffusion towards the flame front.

Formally, the flamelet concept implies that the equations featuring flame structure can be transformed into a one-dimensional problem. An important quantity used to describe non-premixed combustion, specially the location of the flame surface, is the mixture fraction, Z. In an air-fuel system, Z is defined as the ratio of the mass of all elements originated from the fuel stream and the sum of both mass fluxes and it is therefore an index of the local fuel/air ratio. More accurate descriptions of the mixture fraction can be found in [42–44].

Introducing the conserved scalar Z, a new local coordinate system attached to flame can be determined. By definition, Z is locally normal to the reaction zone, almost corresponding to the stoichiometric mixture. Therefore, considering Z as one coordinate and the other two, y_2 and y_3, lying within the reaction zone, the conservation equations for species mass fraction and temperature can be transformed into the new coordinate system. An order of magnitude analysis of the transformed

terms shows that gradients along y_2 and y_2 are negligible, compared to those in Z direction. Thus, the resulting equations, called flamelet equations, appear in one dimensional form and their solutions, $T(Z,t)$ and $Y_i(Z,t)$, completely define the flame structure in the mixture fraction space. A simplified form of the flamelet equations, derived by Peters, are reported below:

$$\rho\frac{\partial Y_i}{\partial t} - \rho\frac{\chi}{2Le_i}\frac{\partial^2 Y_i}{\partial Z^2} = \dot{m}_i \tag{2.19}$$

$$\rho\frac{\partial T}{\partial t} - \rho\frac{\chi}{2}\frac{\partial^2 T}{\partial Z^2} - \rho\frac{\chi}{2c_p}\left(\sum_{i=1}^{N_s}\frac{c_{p_i}}{Le_i}\frac{\partial Y_i}{\partial Z} + \frac{\partial c_p}{\partial Z}\right)\frac{\partial T}{\partial Z} = \frac{1}{c_p}\left(\frac{\partial p}{\partial t} - \sum_{i=1}^{N_s}\dot{m}_i h_i\right) \tag{2.20}$$

where N_s is the number of species considered in the chemical mechanism, χ is the instantaneous scalar dissipation rate, which acts like an increased diffusion coefficient enhancing diffusive transport in mixture fraction space [44], $\dot{m}_i$ and Le_i are the chemical reaction rate and the Lewis number for the generic species i, respectively. In this study, Le_i is assumed to be 1 which means that thermal diffusivity is equal to the diffusion coefficient for each species. It is worth to evidence that there are no convective terms in the flamelet equations. This is due to the fact that all scalar quantities are transported by the same flow field and, hence, no convection relative to mixture fraction appears.

The flamelet parameters

The flamelet equations are a parabolic set of coupled partial differential equations. Therefore, a unique solution exists only if initial and boundary conditions and the time-dependent scalar dissipation rate are known. These factors, together with the pressure, are referred to as *flamelet parameters* and their values influence the solution of the flamelet equations.

The instantaneous scalar dissipation rate measures the gradient of Z and the molecular fluxes of species towards the flame and is defined by

$$\chi = 2D_Z\left(\frac{\partial Z}{\partial x_i}\right)^2 \tag{2.21}$$

where D_Z is the diffusion coefficient for the mixture fraction.

The scalar dissipation rate is the only parameter depending on spatial variables and represents the influence of flow field and mixing on flamelet structure. According to [41], it can be considered as the term which accounts for the departure from chemical equilibrium. Indeed, its reciprocal is a measure of diffusive time: for long diffusion time, i.e. low scalar dissipation rate, the chemical conditions are close to equilibrium, whilst a very high rate stands for extreme strained flame, near extinction.

Initial and boundary conditions are defined for composition and temperature. Composition is initialized in the mixture fraction field with pure mixing solution:

$$Y_i(Z) = (1-Z)Y_i^{air} + ZY_i^{fuel} \tag{2.22}$$

where Y_i^{air} is the mass fraction of species i in the air stream (usually only N_2, O_2, H_2O and CO_2 are considered) and Y_i^{fuel} is the mass composition of fuel stream. Y_i^{air}

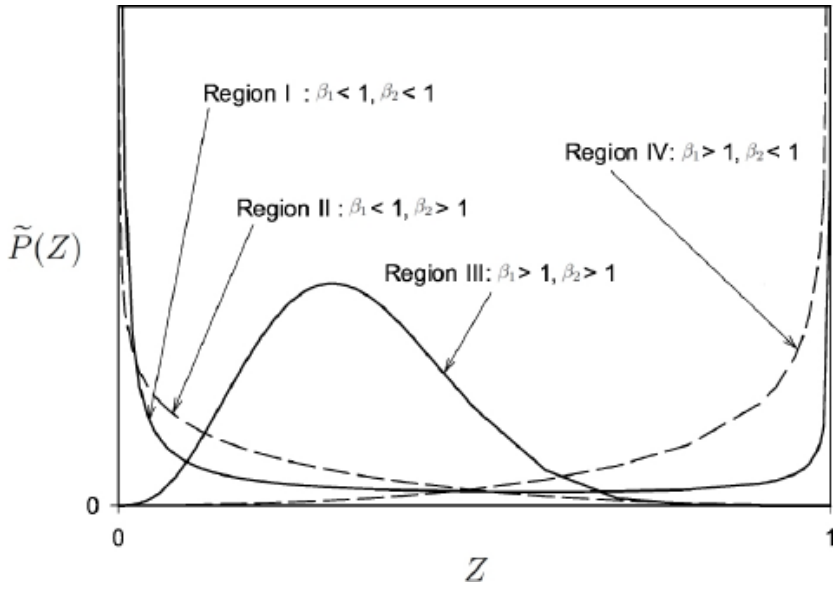

Figure 2.1. Qualitative configuration of the β-PDF with different values of β_1 and β_2.

and Y_i^{fuel} are the boundary conditions for composition and are kept fixed during the simulation.

Known the temperatures of fuel and air streams (the last one is eventually computed as the average of the physical domain), the sensible enthalpy distribution in the mixture fraction space is initialized as:

$$h_s(Z) = (1 - Z)h_s^{air} + Zs_s^{fuel} \tag{2.23}$$

The temperature profile in the Z-space is estimated from the local enthalpy and composition. In relation to boundary conditions, $\mathrm{T_{fuel}}$ is kept fixed throughout the simulation, whereas temperature on the air side changes according to $\frac{dp}{dt}$.

Coupling of the CFD code with the flamelet code

A flamelet based approach defines the time evolution of all reacting scalar as a function of Z. The Favre average composition in the physical domain can be assessed from composition in the Z-space by means of a probability density function of the mixture fraction. The PDF may be either a solution of transport equations or presumed by assuming structure and randomness of the flow field. In this work, as in many engineering studies, the presumed β-PDF is used, which is calculated as

$$\widetilde{P}(Z) = \frac{Z^{\beta_1 - 1}(1 - Z)^{\beta_2 - 1}}{\int_0^1 Z^{\beta_1 - 1}(1 - Z)^{\beta_2 - 1} dZ} \tag{2.24}$$

where β_1 and β_2 are parameters depending on $\widetilde{Z}$ and its variance, $\widetilde{Z''^2}$.

The β-PDF is chosen because it is able to account for the history of the flamelet, changing its shape according to the mixture evolution. Indeed, depending on the parameters β_1 and β_2, four different PDF configurations are possible, as depicted in 2.1.

The trend indicated as "Region I" is typical of a young flamelet, where the fuel stream and the oxidizer stream are still separated. Conversely an old flamelet has a PDF with a shape similar to the one named "Region III", where a peak at approximatively stoichiometric mixture indicates that fuel vapour and oxidizer are well mixed. The shapes "Region II" and "Region IV" are characteristic of low mixture fraction and large variance or large mixture fraction and low variance, respectively. In order to come through singularity and overflow problems, which may arise assessing beta-PDF, the numerical algorithm proposed by Lu et al. in [41] is used in this work.

In order to evaluate the β-PDF, it is necessary to solve transport equations for both $\widetilde{Z}$ and $\widetilde{Z''^2}$:

$$\frac{\partial \bar{\rho}\widetilde{Z}}{\partial t} + \frac{\partial \bar{\rho}\widetilde{u}_i\widetilde{Z}}{\partial x_i} = -\frac{\partial \bar{\rho}\widetilde{u_i''Z''}}{\partial x_i} + \bar{\rho}\widetilde{\dot{S}} \tag{2.25}$$

$$\frac{\partial \bar{\rho}\widetilde{Z''^2}}{\partial t} + \frac{\partial \bar{\rho}\widetilde{u}_i\widetilde{Z''^2}}{\partial x_i} = -\frac{\partial \bar{\rho}\widetilde{u_i''Z''^2}}{\partial x_i} - 2\big(\bar{\rho}\widetilde{u_i''Z''}\big)\frac{\partial \widetilde{Z}}{\partial x_i} - 2\bar{\rho}D\left(\frac{\widetilde{\partial Z''}}{\partial x_i}\right)^2 \tag{2.26}$$

As for RANS equations, models are needed for unclosed terms.

The turbulent transport term is modelled using a classical gradient assumption. The third term on RHS of equation (2.26) measures the decay of mixture fraction fluctuations and is expressed as

$$\widetilde{\chi} = 2D\left(\frac{\partial Z''}{\partial x_i}\right)^2 \tag{2.27}$$

It can be observed that the average scalar dissipation rate acts for Z the same role of epsilon for turbulent kinetic energy; therefore, this analogy is used to model $\widetilde{\chi}$ with a relation that expresses proportionality between scalar dissipation rate and turbulence dissipation time:

$$\widetilde{\chi} = C_\chi \frac{\varepsilon}{k}\widetilde{Z''^2} \tag{2.28}$$

where C_χ takes usually the value of 2.

Substituting all closure models, the resulting equations take the following form:

$$\frac{\partial \bar{\rho}\widetilde{Z}}{\partial t} + \frac{\partial \bar{\rho}\widetilde{u}_i\widetilde{Z}}{\partial x_i} = \frac{\partial}{\partial x_i}\left(\frac{\mu_t}{Sc_{t,Z}}\frac{\partial \widetilde{Z}}{\partial x_i}\right) + \bar{\rho}\widetilde{\dot{S}} \tag{2.29}$$

$$\frac{\partial \bar{\rho}\widetilde{Z''^2}}{\partial t} + \frac{\partial \bar{\rho}\widetilde{u}_i\widetilde{Z''^2}}{\partial x_i} = \frac{\partial}{\partial x_i}\left(\frac{\mu_t}{Sc_{t,Z''^2}}\frac{\partial \widetilde{Z''^2}}{\partial x_i}\right) + 2\frac{\mu_t}{Sc_{t,Z}}\left(\frac{\partial \widetilde{Z}}{\partial x_i}\right)^2 - \bar{\rho}\widetilde{\chi} \tag{2.30}$$

Once the composition in the flamelet space and the density-weighted PDF are known, the turbulent mean mass fractions can be computed integrating the flamelet solutions with the β-PDF, without solving any differential equation in the physical domain:

$$\widetilde{Y}_i(\mathbf{x}, t) = \int_0^1 \widetilde{P}(Z, \mathbf{x}, t) Y_i(Z, t) dZ \tag{2.31}$$

The scalar dissipation rate is itself subjected to turbulence; therefore, to account for turbulent fluctuations, a PDF for χ must be retained. In order to avoid double integration at every grid point, a very time consuming operation for unsteady

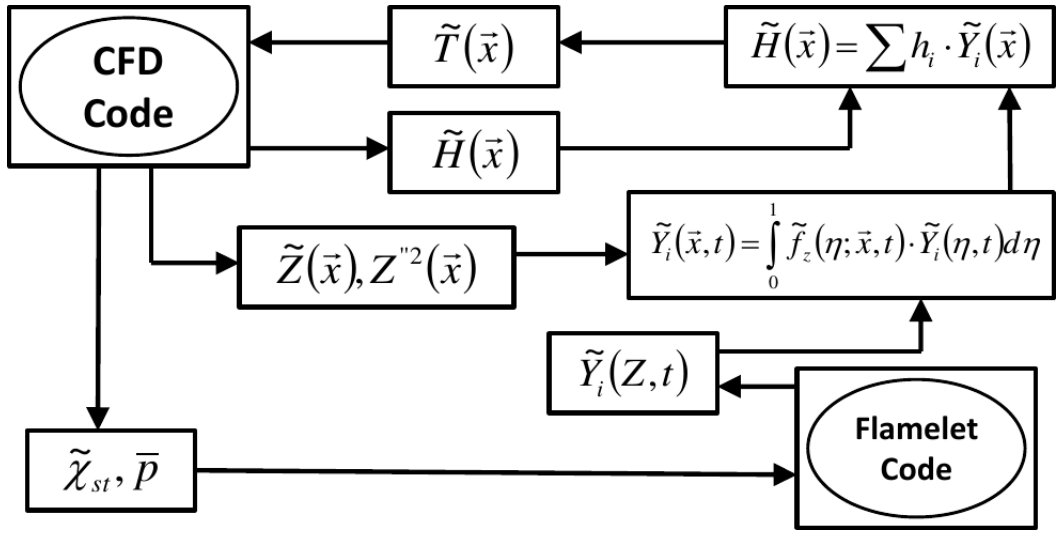

Figure 2.2. Coupling of the RANS equations with the flamelet equation performed by the Representative Interaction Flamelet model reproduced from [45].

flamelets, a conditional mean scalar dissipation rate is used in flamelet equations of this work. The mean scalar dissipation rate model will be discussed below.

Figure 2.2 shows how the RIF model couples the solution of the RANS equations with the flamelet code.

Firstly, the CFD code, with the equations for density, momentum, total enthalpy, turbulence, Z and its variance, is solved. In order to solve flamelet equations, pressure and the Z-dependence of the scalar dissipation rate must be known. According to [46], the pressure can be considered spatially constant. The scalar dissipation rate as a function of Z is expressed as

$$\chi(Z) = \widehat{\chi}_{st} \frac{f(Z)}{f(Z_{st})} \tag{2.32}$$

where χ_{st} is the surface average value for the scalar dissipation rate at stoichiometric mixture fraction computed as proposed by Pitsch in [47] and $f(Z)$ has an erfc-profile [48].

After calculating these flamelet parameters, the flamelet code solves for the unsteady flamelet equations and evaluates the composition in the Z-space with time steps that are much smaller than the CFD ones; in this way, fluid dynamics and chemistry problems are effectively decoupled. The turbulent mean mass fractions $\widetilde{Y}_i(x,t)$ are computed by integrating the flamelet solutions $Y_i(Z,t)$ with the β-PDF. Finally, the physical temperature field is obtained combining iteratively the enthalpy field and the species mass fraction fields:

$$\widetilde{h} = \sum_{i=1}^{N_s} \widetilde{Y}_i h_i(\widetilde{T}) \tag{2.33}$$

where $h_i(\widetilde{T})$ are the species enthalpy estimated with NASA polynomials.

According to [49], flamelet equations are interactively solved with the CFD solver and avoid the use of flamelet libraries to account for flamelet hystory concerning

flamelet parameters. Indeed, flamelets are no function of state relative to flamelet parameters because their response to parameter variations is not infinitely fast; therefore, a unique flamelet solution for a specified set of flamelet parameters does not exist.

The Eulerian Particle Flamelet Model (EPFM)

As it was mentioned beforehand, the solution of the flamelet equations depends on values of the flamelet parameters. Thus, if high spatial variations of these parameters occur, different flamelet histories must be calculated in order to enhance accuracy. As Pitsch reports in [49], the required number of flamelets can be estimated by a presumed criterion for the uniformity of the monitoring flamelet parameter selected within the current flamelet domain. Usually, the scalar dissipation rate is chosen as the reference parameter, since it is the main significant flamelet parameter: if the variance of the scalar dissipation rate in a flamelet exceeds a certain limit, this flamelet is subdivided into two flamelets and all the regions where the limit is overcome are attributed to the new flamelet. Markers particles, $I_l(\mathbf{x}, t)$, are introduced, each of them accounting for the flamelet path through the turbulent flow field and standing for the probability of finding the associated flamelet l at location $\mathbf{x}$ and time t. Thus, an Eulerian convection-diffusion equation is solved for every marker and the model is called Eulerain Particle Flamelet Model (EPFM):

$$\frac{\bar{\rho}\widetilde{I_l}}{\partial t} + \nabla \cdot (\bar{\rho}\mathbf{u}\widetilde{I_t}) = \nabla \cdot \left(\frac{\mu_t}{Sc_t} \nabla \widetilde{I_t} \right) \tag{2.34}$$

where Sc_t is the turbulent Schmidt number.

The presence of these markers modifies the surface average scalar dissipation rate and the integration of the flamelet solution with the β-PDF, weighting them with the probability of finding a certain flamelet in the physical domain [46].

As suggested by D'Errico in [50], in this work each flamelet is representative of a certain portion of the injected fuel mass:

$$\int_V \bar{\rho}\widetilde{Z_l} dV' = \frac{m_{inj}}{n_{f,max}} \tag{2.35}$$

where Z_l is the portion of mixture fraction field related to flamelet l, m_{inj} is the total injected fuel mass and $n_{f,max}$ is the maximum number of flamelets used for the computation. For each flamelet, the following Z_l equation is solved:

$$\frac{\bar{\rho}\widetilde{Z_l}}{\partial t} + \frac{\partial \bar{\rho}\widetilde{u_i}\widetilde{Z_l}}{\partial x_i} = \frac{\partial}{\partial x_i}\left(\frac{\mu_t}{Sc_{t,Z}} \frac{\partial \widetilde{Z_l}}{\partial x_i} \right) + \nu_l \bar{\rho}\widetilde{\dot{S}} \tag{2.36}$$

where ν_l is equal to 1 only if l corresponds to the last flamelet and equal to 0 for other flamelets. In this way, evaporation of the liquid is accounted only in the youngest flamelet. With this method, Z_l equations are unnecessary because the probability associated to flamelet l becomes

$$\widetilde{I_l}(\mathbf{x}, t) = \frac{\widetilde{Z_l}}{\widetilde{Z}} \tag{2.37}$$

This approach is simpler than the original one and it is still able to account for variation of the scalar dissipation rate in the physical domain since this flamelet parameter evolves with injection [46].

Chapter 3

Soot modeling

In this chapter, the semi-empirical soot models proposed by Moss [1], Lindstedt and Leung [2] and Wen [5], which have been implemented in the CFD code, are described.

A brief literature review is first given to provide the picture of the state of art of soot modeling.

3.1 Review of soot models

Many efforts have been made by researchers in last decades to better understand the phenomenology of soot formation and burnout in combustion systems with great progresses, but not all soot processes are still completely clear. Nevertheless, for the increasingly stringent limits on pollutant emissions and the problems that soot may cause to combustion devices, engineers are facing with a pressing need to design systems in which the amount of soot is controlled. For these reasons, over the years, along with a big amount of experimental and theoretical works, several different approaches have been developed in modelling soot formation and oxidation (an extended review can be found in [21]).

Models can be grouped into three categories [21]: purely empirical correlations, semi-empirical models (or semi-global mechanism) and detailed chemistry models.

Empirical correlations are simple expressions in which some parameters are tuned so that predictions are in agreement with measurements. It is obvious that, in this way, these correlations can be applied only in condition close to those for which the original data were first obtained and only for a certain types of engines and specific fuels [29].

Semi-empirical correlations are also defined semi-global mechanism because these soot models describe the formation and oxidation of soot particles by two or more global reaction steps solving related rate equations. This approach attempts to take into account the global physics and chemistry of the phenomenon, but, given its simplicity, it must hold some constant parameters that are set in order to have a good agreement with experimental data. Thus, semi-empirical models have greater generality than empirical models but attention is needed when applying the models for conditions different from those of models set-up. Due to the need for simple and well defined test cases, these semi-empirical soot models are usually developed

and tested for laminar flames and, then, they are incorporated in existing codes for turbulent combustion. During the last two decades, attention has been focused on rather simple semi-empirical soot models used in conjunction with PDF and flamelet-based combustion models. This is the approach that has been employed in the present work, where essentially three semi-empirical soot models, developed by Moss [1], Brookes [4] and Lindstedt-Leung [2, 3] respectively and detailed in the following paragraphs, have been implemented in a flamelet combustion model. Other models widely used are, for example, those of Tesner [51], Hiroyasu [52], Kennedy [53], Young [54], Fairweather [55], Kronenburg [56], Fusco [57].

All models solve a small number of differential equations for the conservation of quantities such as soot particle number density and soot volume fraction, introducing rates for global phases of soot formation and oxidation.

The linking of soot kinetics to turbulence and gas-phase chemistry is crucial for the success of the simulations. Since the objective is the use of a soot model in turbulent combustion, the introduction of a few additional variables is an essential aspect of these class of models.

Finally it is important to emphasize that, once empirical parameters have been set properly, a semi-empirical soot model performance is typically such that the qualitative effects of various engine parameters on the soot emissions can be estimated properly [14].

Detailed models solve the rate equations for elementary processes that lead to soot, related to both gas-phase kinetics, in order to describe the chemical reactions on a molecular scale, as well as particle dynamics, to describe processes such as particle inception, surface growth, coagulation and oxidation on the particle scale. In this way they manifest a greater generality and they can be applied to conditions far from those for which the rates were measured. Frencklach et al. [58] have developed the most popular detailed soot model, but many other works have been elaborated (for example, Balthasar [59], Kazakov [60] or Mauss [61]). The problem of these types of models is that are extremely computationally expensive even for simple laminar flames. For predictions of soot in practical turbulent engineering equipment it is often necessary to use simplified, semi-empirical models to keep CPU-cost at an acceptable level [29].

Soot influences thermochemistry of the flame also by radiation. When a flame is characterized by high soot loads, soot model cannot overlook the presence of a radiation sub-model.

3.2 Semi-empirical soot models

In this work, three soot models, developed respectively by Moss [1], Lindstedt [2] and Brookes [4] in the version slightly modified by Wen [5], have been implemented in the CFD code (see chapt. 4) and tested. The implemented models have similar structures, presenting two transport equations, one for soot molar density, cNp [$\mathrm{kmol_{soot}/m^3}$], which is the ratio between particle number density, n_{soot} [number of particles/$\mathrm{m^3}$], and Avogadro's number, N_a, equal to $6 \cdot 10^{26}$ [$\mathrm{kmol^{-1}}$], and one for soot mass density $\rho_s f_v$ [$\mathrm{kg_{soot}/m^3}$], where ρ_s is soot density and f_v is the soot volume fraction [$\mathrm{m^3{}_{soot}/m^3}$]. The equations are coupled through the assumption of

spherical particles which conforms with a mono-disperse size distribution.

The models described physics and chemistry of soot with global steps of nucleation, soot mass growth, agglomeration, and soot oxidation.

In the present work, soot equations are solved in the flamelet domain, i.e. soot particles are treated as chemical species, following works of Pitsch et al. [47, 49]. The subsequent soot distribution in the physical domain is then obtained by weighting the solution in mixture fraction space with the β-PDF. Unlike what happens for the chemical species, however, source terms related to soot formation and oxidation are semi-global reaction step and they are not incorporated in the kinetic gas-phase scheme. Performing the calculation for pollutant formation as a sort of post processing means a significant gain in terms of CPU-time. In fact, source terms are calculated from temperature and species concentrations already computed in the specific time step. On the other hand, this introduces the further approximation of the non-consumption of chemical species involved in sooting processes. In literature not all authors agree with the validity of this approach. Some argue that the slower kinetics of soot and the greater Lewis number (in particular for the larger particles) do not fit well with the flamelet theory, but Pitsch et al. in [47, 49] and other works have demonstrated that it is possible to make predictions of soot formation using such a post processing concept.

The general form of the two additional flamelet equations for soot is reported below:

$$\frac{\partial cNp}{\partial t} - \frac{\chi}{2}\frac{\partial^2 cNp}{\partial Z^2} + \frac{1}{2}\frac{\partial \chi}{\partial Z}\frac{\partial cNp}{\partial Z} = R^{cNp}_{nucleation} - R^{cNp}_{coagulation} \tag{3.1}$$

$$\frac{\partial \rho_s f_v}{\partial t} - \frac{\chi}{2}\frac{\partial^2 \rho_s f_v}{\partial Z^2} + \frac{1}{2}\frac{\partial \chi}{\partial Z}\frac{\partial \rho_s f_v}{\partial Z} = R^{\rho_s f_v}_{nucleation} - R^{\rho_s f_v}_{growth} - R^{\rho_s f_v}_{oxidation} \tag{3.2}$$

The source terms will be detailed on the basis of the different models. It is worth to note that, because oxidation of soot is a surface phenomenon, the assumption that it has not a great effect on particles number but only on the soot mass has been made.

3.2.1 Moss model

In the soot model of Moss, the source terms related to global processes mentioned above, that appear in transport equations for soot molar density and soot volume fraction, take the forms:

$$R^{cNp}_{nucleation} = \alpha = C_\alpha \rho^2 T^{0.5} x_{C_2H_2} exp\left(\frac{-T_\alpha}{T}\right) \tag{3.3}$$

$$R^{cNp}_{coagulation} = \beta \cdot cNp^2 = C_\beta T^{0.5} \cdot cNp^2 \tag{3.4}$$

$$R^{\rho_s f_v}_{nucleation} = \delta = C_\delta \cdot \alpha \tag{3.5}$$

$$R^{\rho_s f_v}_{growth} = \gamma \cdot cNp \cdot N_a = C_\gamma \rho T^{0.5} x_{C_2H_2} exp\left(\frac{-T_\gamma}{T}\right) \cdot cNp \cdot N_a \tag{3.6}$$

ρ and T are the local mixture density and temperature respectively, $x_{C_2H_2}$ is molar fraction of C_2H_2, S_p is the surface of the mean particle, ω_{ox} is the oxidation rate, T_α and T_γ are activation temperatures related to steps of nucleation and surface growth and C_α, C_β, C_γ and C_δ are prescribed numerical constant. Moss has adjusted the

values of this constant from comparison between predictions and measurements in a laminar diffusion flame of ethylene [1] and the activation temperature are taken from [62], reported in tab. 3.1.

Moss assumes a value for ρ_s of 1800 kg/m^3.

Table 3.1. Constants for the soot model by Moss.

C_α $[\mathrm{m^3\,kg^{-2}\,K^{-0.5}\,s^{-1}}]$	C_β $[\mathrm{m^3\,K^{-0.5}\,s^{-1}}]$	C_γ $[\mathrm{m^3\,K^{-0.5}\,s^{-1}}]$	C_δ	T_α [K]	T_γ [K]
6×10^{26}	2.25×10^{15}	6.3×10^{-14}	144	46000	12600

Moss underlines that the values of the constants vary quite widely with fuel and operating conditions, that can be seen from other his works [63, 64].

Calculations of the scalar field were performed with full chemistry and a flamelet approach, defining temperature and gaseous species as functions of mixture fraction. Then, species and temperature distributions are computed in the CFD domain with a two-dimensional code, whereas the balance equations of n_{soot} and f_v are solved directly in the CFD domain, incorporating the chemical source terms of equations (3.1) and (3.2). Moss neglected contribution of radiation by soot because the flame is weakly sooting.

The term of surface growth in eq. (3.1) is proportional to the concentration of C_2H_2: indeed, acetylene is considered the major species involved in surface growth of soot. This term is also proportional to the number density and not to the surface area, as might be expected. It is possible to estimate the mean particle size and, hence, the soot particle diameter, by combining f_v and n_{soot} with the following relation:

$$f_v = \frac{\pi}{6} n_{soot} d^3 \tag{3.7}$$

In [64], Moss et al. show that a surface growth term proportional to surface area of soot, for the referred conditions, determines an over-prediction of soot and a time dependence of f_v that is not generally observed throughout the flame [1]. The nucleation term is also proportional to the molar fraction of C_2H_2. As it was outlined in chapt. 1, C_2H_2 is the main product of the pyrolysis of hydrocarbons and the principal species involved in the reaction leading to first aromatic ring and in the growth to PAHs. The chemistry of PAHs growth and nucleation is very complex and still not fully understood, but the need to have a simple model, coupling with a gas-phase kinetics, leads to make this assumption.

The coagulation rate term in eq. (3.1) is proportional to the square root of temperature and to the square of particle number density, coherently with the dynamics of coagulation presented earlier.

Unlike the surface growth, term of oxidation is proportional to the surface of soot considering particle size effects: given the mean diameter of particles calculated from (3.7), S_p is expressed as

$$S_p = \left(\frac{36\pi}{\rho_s^2}\right)^{\frac{1}{3}} n_{soot}^{\frac{1}{3}} \left(\rho_s f_v\right)^{\frac{2}{3}} \tag{3.8}$$

In his work, Moss has compared the three more consolidated models for soot oxidation: Nagle and Strickland-Constable [65], Lee et al. [66], Fenimore and Jones [30].

Nagle and Strickland-Constable consider oxidation only by O_2 and assume that there are two types of active sites on soot surface: more reactive (A) and less reactive (B). Three types of reactions are assumed (with their respective reaction rates), namely the oxidation of both A and B sites as well as their thermal rearrangement:

$$\mathrm{A} + \mathrm{O_2} \longrightarrow \mathrm{A} + 2\,\mathrm{CO} \qquad \dot{\omega} = \frac{k_A P_{\mathrm{O_2}}}{1 + k_Z P_{\mathrm{O_2}}} \chi \tag{3.9}$$

$$\mathrm{B} + \mathrm{O_2} \longrightarrow \mathrm{A} + 2\,\mathrm{CO} \qquad \dot{\omega} = k_b P_{\mathrm{O_2}} (1 - \chi) \tag{3.10}$$

$$\mathrm{A} \longrightarrow \mathrm{B} \qquad \dot{\omega} = k_T \chi \tag{3.11}$$

where $P_{\mathrm{O_2}}$ is the partial pressure of O_2 and the kinetic constants assume the value reported below:

$$k_A = 20 exp\left(\frac{15098}{T}\right) \tag{3.12}$$

$$k_B = 4.46 \times 10^{-3} exp\left(\frac{-7650}{T}\right) \tag{3.13}$$

$$k_T = 1.51 \times 10^{5} exp\left(\frac{-48817}{T}\right) \tag{3.14}$$

$$k_Z = 21.3 exp\left(\frac{2063}{T}\right) \tag{3.15}$$

χ is the fraction of A sites on the surface and, assuming quasi-steadiness by matching eqn. (3.10) with eqn. (3.11), it takes the form

$$\chi = \left[1 + \left(\frac{k_T}{k_B P_{\mathrm{O_2}}}\right)\right]^{-1} \tag{3.16}$$

Thus, the overall reaction rate is given by

$$\omega_{NSC} = 1.2 \times 10^2 \cdot \left(\frac{k_A P_{\mathrm{O_2}} \chi}{1 + k_z P_{\mathrm{O_2}}} + k_B P_{\mathrm{O_2}} (1 - \chi)\right) \tag{3.17}$$

Lee et al. derived a simpler model by measurements carried out on a laminar diffusion flame, assuming that particles were small enough that diffusion did not limit the rate of oxidation and that the kinetics of surface reactions were assumed to be the limiting mechanism. They have formulated this expression:

$$\omega_{LBT} = 1.085 \times 10^5 P_{\mathrm{O_2}} T^{-0.5} exp\left(\frac{-19778}{T}\right) \tag{3.18}$$

where values of the constant and activation temperature can be modified with the variations of operating conditions.

Fenimore and Jones [18] demonstrated that even in slightly fuel-rich gas where $P_{\mathrm{O_2}}$ is very small, oxidation rates remains considerable and about five times faster than those reported by Lee at the same temperature and O_2 partial pressure. On

the other hand, OH is considered to be the main oxidant under stoichiometric and fuel-rich conditions. Therefore, Fenimore and Jones proposed the following oxidation model:

$$\omega_{FJ} = 1.27 \times 10^3 \Gamma P_{OH} T^{-0.5} \tag{3.19}$$

where Γ is the collisional efficiency, that is the fraction of collisions that results in a single carbon atom being removed from the soot molecule, and it is taken equal to 0.1, according to the measurements of Neoh et al. [32], while P_{OH} is the partial pressure of OH radicals.

Results of Moss demonstrate that OH mechanism gives the best results reflecting the fact that on the fuel side of a diffusion flame, OH radicals play a dominant role in the oxidation of soot. Therefore, in the simulation performed in this work, the mechanism of Fenimore and Jones is used.

3.2.2 Lindstedt and Wen models

The soot model of Lindstedt-Leung and Wen are jointly presented because they have the same structure but different model parameters and constant [29].

$R^{\rho_s f_v}_{nucleation}$, $R^{\rho_s f_v}_{growth}$, $R^{\rho_s f_v}_{oxidation}$ include a modified Arrhenius rate constant of the form

$$k_i = A_i T^{B_i} exp\left(\frac{-E_i}{RT}\right) \tag{3.20}$$

The values of parameters for the two different models are reported in tab. 3.2.

As for Moss, it is assumed that acetylene is the indicative species for nucleation and surface growth of soot, making the simplifying hypothesis that these steps are first-order functions of acetylene concentration.

The nucleation step is based on the following reaction step:

$$\mathrm{C_2H_2} \longrightarrow 2\,\mathrm{C(s)} + \mathrm{H_2} \tag{3.21}$$

Thus the nucleation rate takes the form:

$$R^{\rho_s f_v}_{nucleation} = 2k_1(T)[\mathrm{C_2H_2}]M_s \tag{3.22}$$

The surface growth step reflects the assumption that growth occurs by $\mathrm{C_2H_2}$ absorption on the soot surface:

$$\mathrm{C_2H_2} + \mathrm{nC(s)} \longrightarrow (\mathrm{n} + 2)\,\mathrm{C(s)} + \mathrm{H_2} \tag{3.23}$$

where the associate reaction rate is

$$R^{\rho_s f_v}_{growth} = k_2(T) f(S)[\mathrm{C_2H_2}]M_s \tag{3.24}$$

$[\mathrm{C_2H_2}]$ is the molar concentration of acetylene and $f(S)$ is a function of the soot surface area.

The surface ageing of soot particles would imply a temporal dependence of the rate constant of the soot surface growth step with further equations describing the loss of reactivity of active sites with time. This would add complexity and uncertainty to the model and therefore Lindstedt has made the assumption that the

Table 3.2. Constants of Lindstedt and Wen models

		Lindstedt	Wen
General	ρ_s	2000	2000
	M_s	12.011	12.011
Nucleation	A_{nucl}	10000	5400
	b_{nucl}	0	0
	$\frac{E_{nucl}}{R}$	21100	21100
	C_{min}	100	100
Mass growth	A_{growth}	6000	750
	b_{growth}	0	0
	$\frac{E_{growth}}{R}$	12100	12100
	$f(S)$	$\sqrt{S}$	S
Oxidation	A_{O_2}	10000	741.3
	b_{O_2}	0.5	0.5
	$\frac{E_{O_2}}{R}$	19680	19778
	A_{OH}	9	8.8
	b_{OH}	0.5	0.5
	$\frac{E_{OH}}{R}$	0	0
	Γ_{OH}	0.04	0.13
Agglomeration	C_a	9	1

initial formation of soot particles is dominated by the nucleation of incipient particles and initial elevated surface growth. This allows to introduce a simple approximated way to take in account the reduced reactivity of surface: unlike the model of Wen, in which there is a linear dependence from surface (see tab. 3.2), Lindstedt assumes that the number of active sites is proportional to the square root of the soot surface. Also the activations temperatures and pre-exponential factors were chosen according to this hypothesis. The model of Wen shares with that of Lindstedt the activation temperatures.

Lindstedt in [3] and Wen [5] propose inception models based, respectively, on benzene as indicative species and on the formation rates of two and three ringed aromatics from acetylene, benzene and the phenyl radical (C_6H_5). These inception models show a better behaviour in the prediction of soot nucleation, especially when they are used with complex fuels including a not negligible amount of aromatic species, and they allow to obtain greater generality in the context of semi-empirical models. These versions have not been implemented because the fuels employed in the simulations performed are aliphatic hydrocarbons, namely n-dodecane and n-heptane. Moreover, the need to limit the computational time, yet costly in turbulent combustion simulations, avoids the use of detailed gas-phase kinetics mechanisms.

For what concerns the soot oxidation step, the original model of Lindstedt does not consider the oxidation by OH radicals, but only by O_2. Because of the recognised importance of soot burnout by OH, its contribution has been added following the works of Kronenburg [56] and Bolla [67, 68].

Wen, which employs both species in oxidation model, shows that O_2 practically plays a negligible role in soot oxidation in his turbulent jet diffusion flame of kerosene.

The chemical model equations for soot oxidation are

$$\mathrm{C(s)} + \frac{1}{2}\,\mathrm{O_2} \longrightarrow \mathrm{CO} \tag{3.25}$$

$$\mathrm{C(S)} + \mathrm{OH} \longrightarrow \mathrm{CO} + \mathrm{H} \tag{3.26}$$

and the soot oxidation term takes the following form:

$$R^{\rho_s f_v}_{oxidation} = k_3(T) S[\mathrm{O_2}] M_s + k_6(T) \Gamma_{\mathrm{OH}} S[OH] M_s \tag{3.27}$$

where Γ_{OH} is the collisional efficiency.

Particle nucleation step in the equation of soot molar density takes the form:

$$R^{cNp}_{nucleation} = \frac{2}{C_{min}} \frac{R^{\rho_s f_v}_{nucleation}}{M_s} \tag{3.28}$$

where C_{min} is the number of carbon atoms in the incipient soot particle.

Both models assumed that nuclei has formed by 100 carbon atoms, giving a particle size of around 1.24 nm. As Lindtstedt emphasizes in his work, however, it can be shown that the final results are not strongly dependent on the presumed size of the incipient particle provided that this remains in the range 1-10 nm. The decrease in the number of particle is simply assumed to occur according to particle coagulation for which it is assumed a normal square dependence coherently with the expression presented above in the brief explanation of coagulation and agglomeration:

$$\mathrm{nC(s)} \longrightarrow \mathrm{C_n(S)} \tag{3.29}$$

$$R^{cNp}_{agglomeration} = -2C_a d_p^{1/2} \left(\frac{6\kappa T}{\rho_s} \right) \left(cNp \cdot N_a \right)^2 \tag{3.30}$$

where C_a is the agglomeration rate constant, which assumes different values depending on the model: 9 in the model of Lindstedt and 1 in that of Wen. C_a takes in account that the measured values of the agglomeration rate is several times higher that the theoretical one derived by the free-molecule kinetic theory.

Chapter 4

Soot modeling in CFD simulation

The soot models of Moss, Lindstedt and Wen have been implemented in the library flameletCombustionModels of Lib-ICE library for internal combustion engine which is based on the OpenFOAM technology. Therefore, before describing the flamelet soot library developed in this work, OpenFOAM and Lib-ICE are briefly presented.

4.1 OpenFOAM and the Lib-ICE library

OpenFOAM (Open source Field Operation and Manipulation) is an open source C++ library working on Unix based operating systems that has been developed for solving continuum mechanics problems, including computational fluid dynamics. OpenFOAM is distributed with pre-compiled executables, known as applications, and libraries. Applications are split into two main categories: solvers, designed to solve a specific problem, and utilities, for manipulating data. Libraries are code transposition of physical models and are dynamically linked runtime. Both applications and libraries are supplied as source codes and thanks to the object-oriented programming language modifications of existing models and applications and implementation of new ones are possible, enabling the solution of complex and user specific problems.

Lib-ICE is a set of applications and libraries for internal combustion engine simulations, developed by ICE group of Politecnico di Milano. Lib-ICE uses OpenFOAM pre-compiled operators and classes, e.g. regionModel class that performs exchanges of information between CFD mesh and region mesh and is used to derive the flameletCombustionModels class. Figure 4.1 shows Lib-ICE structure, very similar to the one of OpenFOAM. The applications directory contains solvers, grouped in five categories: cold flow solvers, compressible solvers, Diesel combustion solvers, multiphase solver and spark-ignition combustion solvers. The utility directory hosts tools for case set-up, mesh generation, parallel processing and post-processing. The src directories holds codes for modeling in-cylinder flow and processes such as spray, combustion, pollutant formations and liquid film.

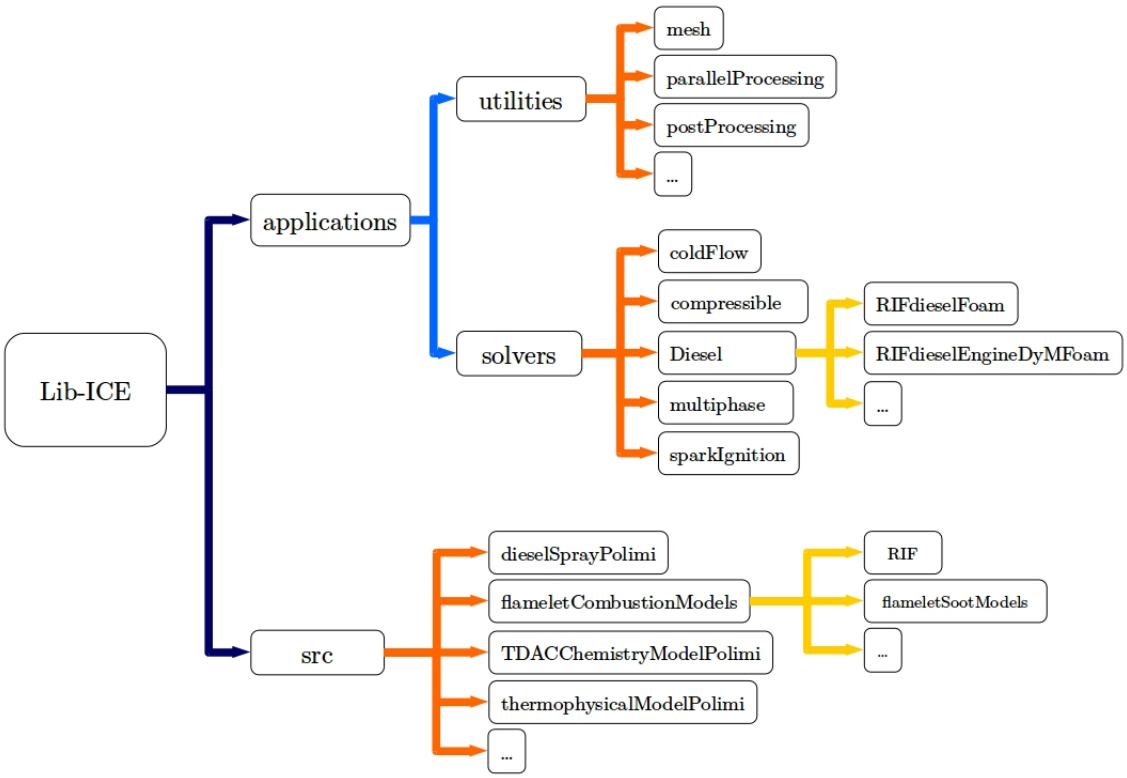

Figure 4.1. Lib-ICE code structure.

4.2 Soot models in the Lib-ICE library

flameletMoss, flameletWen and flameletLindstedt are derived OpenFOAM classes of flameletSootModel (fig.1) that solve the flamelet equations for soot with source terms respectively proposed by Moss, Wen and Lindstedt. As described in (chapter 3), the soot models are integrated in the RIF model for spray combustion which is available in Lib-ICE with two different solvers: RIFdieselFoam, for constant volume simulations, and RIFdieselEngineDyMFoam, for internal combustion engine simulations. The most representative steps of the two solvers and the employed Lib-ICE libraries are depicted in figure 4.2.

The time loop starts with the Lagrangian spray solver, owned by dieselSprayPolimi, that provides the source terms of transport equations for Z and its variance. At the end of the spray evolution, the routine solveFlamelets.H begins and points the RIF library, called for the first time. RIF solves the flamelet equations (2.19) and (2.20), closed with $\widehat{\chi}_{st}$ and the mass reaction rate of each chemical species, respectively provided by the scalarDissipationRate library, included in thermophysicalModelsPolimi, and by one of the chemistry solver defined in TDACChemistryModelPolimi.

Next, the continuity equation (2.9) is solved in rhoEqn.H, followed by the so called "PIMPLE loop". The PIMPLE loop is an algorithm for the solution of pressure-velocity coupling which results from the combination of the SIMPLE algorithm and the PISO algorithm. Briefly, the PIMPLE loop starts with the solution of the momentum equations with the available pressure field and then the PISO algorithm

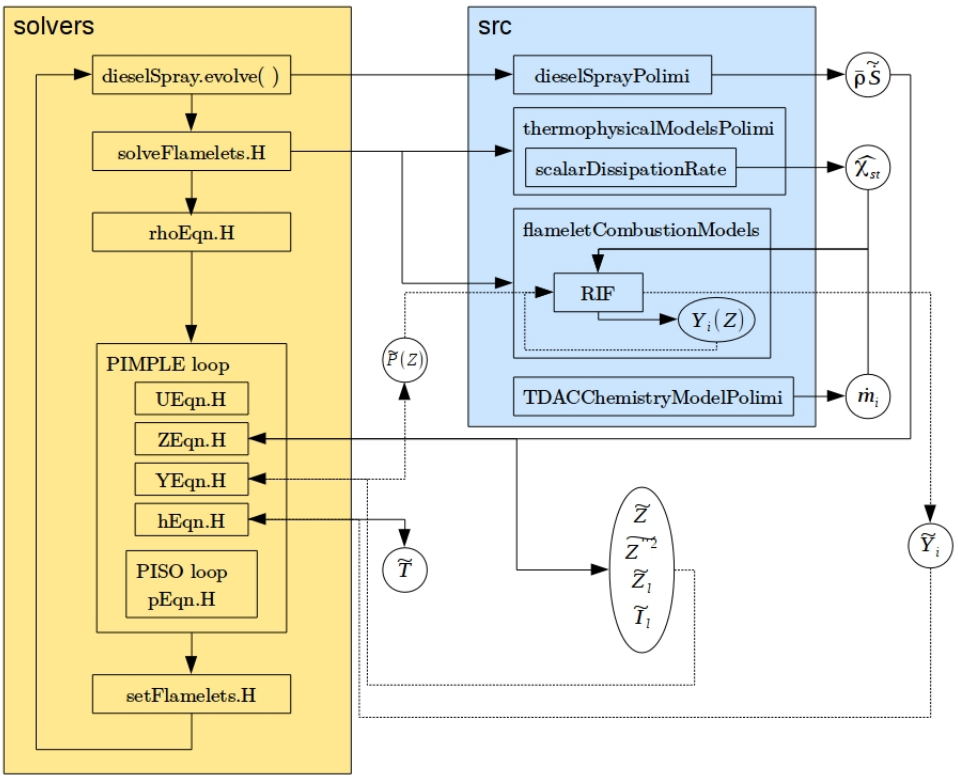

Figure 4.2. Code structure of RIFdieselFOAM. The second passage through the RIF library is marked with dashed lines.

is used to rectify the second pressure correction and to adjust both velocities and pressure explicitly. The sequence is concluded with an additional integration using the final values obtained at the end of the previous iteration as initial values, eventually involving under-relaxation factor for pressure.

During the PIMPLE loop other transport equations are solved. Firstly, in ZEqns.H equations for Z, Z_2'', I_l and Z_l are solved. Later, the routine YEqns.H calls back the RIF library and the β-PDF integration of species mass fraction is performed through equation (2.31). The total entalphy field is computed in hEqn.H and the temperature field is estimated with equation (2.33). The current time step is concluded with eventually setting a new flamelet in setFlamelets.H, if all the necessary constrains to subdivide the domain are satisfied.

The flameletSootModel library and its derived classes are invoked when the RIF library is called for the first time. The flameletSootModel solved the flamelet equations for soot, according to the chosen model, and provides the mass fraction (Y_{soot}), the volume fraction (f_v) and the particles number density (n_{soot}) of soot to the RIF library (figure 4.3). During its second call, the RIF library performs the integration with β-PDF of all soot parameters mentioned above.

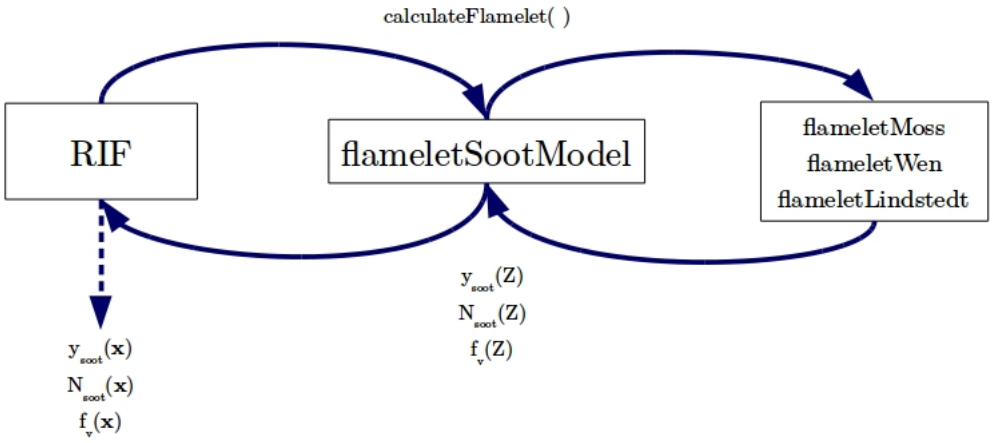

Figure 4.3. flameletSootModel and RIF library interaction. The first passage in the RIF library is marked with full lines, the second one with dashed lines.

Chapter 5

Case set-up

The aim of this work is to test the soot models incorporated in the framework of the RIF combustion model in a constant volume chamber for different operating conditions, taking advantage of the data supplied by the SANDIA National Laboratories (SNL). The choice of the experimental reference is due to the wide range of ambient conditions which can be reliably reproduced and the large amount of experimental data publicly available [69].

In this chapter, the SNL vessel and the test cases are firstly presented. The following sections are dealt with description of the CFD simulation set-up.

5.1 Experimental set-up

The SNL vessel is a constant volume vessel with a cubical-shaped combustion chamber of 108 mm side. Figure 5.1 provides the schematic cross-section of the vessel. Further information about the geometry of the chamber and its features can be found in [69].

The ambient conditions at the time of fuel injection space among gas temperature from 450 K to 1300 K, gas density from 3 kg/m^3 to 60 kg/m^3 and oxygen molar concentration from 0% to 21%. Multiple fuels can be injected in the vessel, like D2, single-component fuels and oxygenated fuels. The injection system is a common-rail injector with injection pressure variable from 40 MPa to 200 MPa and nozzle diameters ranging from 0.05 mm to 0.5 mm.

Several experimental diagnostics are available for combustion tests. In the following part, only the techniques able to obtain data useful for the validation presented in this study are briefly explained. A complete and accurate description of the whole diagnostic is discussed in [69].

The lift-off length can be estimated through chemiluminescence coming from excited-state OH (OH*), which is the main source of light emission at 310 nm and results from chemical reactions in near-stoichiometric, high-heat release region. Time-averaged, line-of-sight images of light emitted from a burning fuel jet at 310 nm were acquired with an intensified CCD camera using a 310 nm band-pass filter. Two lobes of intense chemiluminescence are usually present around the spray centreline; thus, the lift-off length is determined by finding the distances between the injector and the first axial locations above and below the spray centreline with an intensity

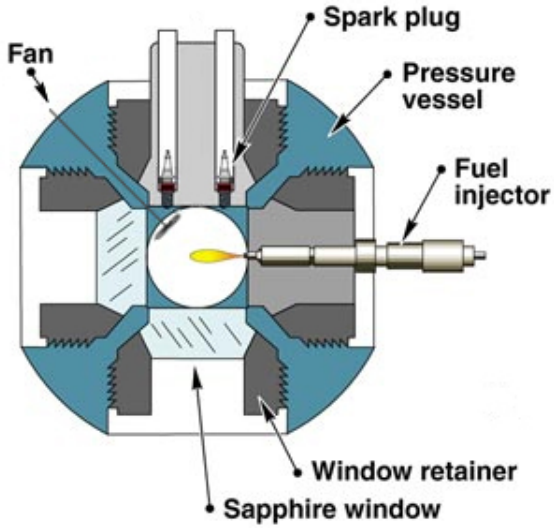

Figure 5.1. Schematic cross-section of the SNL vessel reproduced from [69].

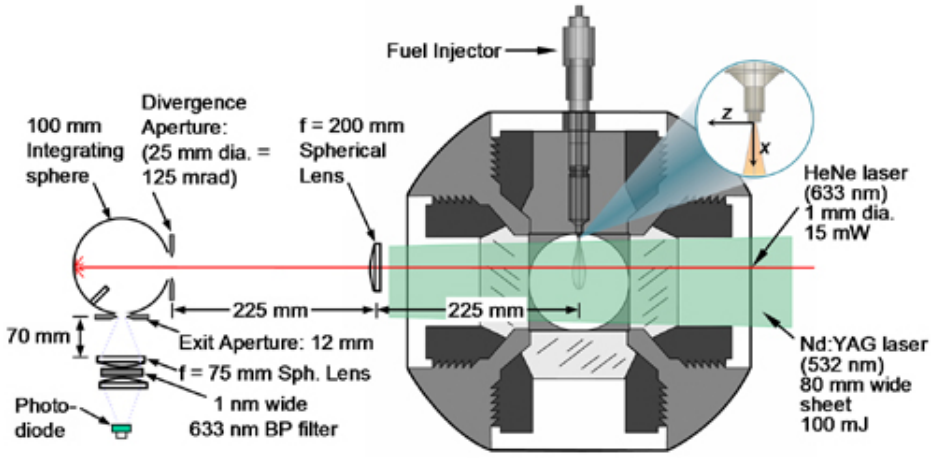

Figure 5.2. Schematic of the combustion vessel and optical set-up for soot measurements reproduced from [69].

greater than approximately 50% of the levelling-off value.

The ignition delay is evaluated with two different techniques: chemiluminescence images, that allow to record the high-temperature combustion, and pressure history, acquired using a piezoelectric transducer.

Quantitative soot measurements are provided by laser extinction and planar laser-induced incandescence (PLII), as illustrated in fig. 5.2.

For laser extinction, a modulated (50 kHz), 15 mW, 1 mm diameter HeNe laser beam (632.8 nm) was passed through sooting regions of a fuel jet and collected by an integrating sphere, narrow bandpass filter, and photo-diode. The transmitted laser intensities are related to soot optical thickness, KL, as follow:

$$\frac{I}{I_0} = exp(-KL) \tag{5.1}$$

where K is the extinction coefficient, L is the path length through soot, I and I_0 are transmitted laser intensities with and without soot present, respectively. The optical

Table 5.1. Case set-up for constant volume vessel simulations for Spray-A

fuel		n-dodecane				
Amb. temp.	[K]	850	900	1000	900	900
O_2 molar fract	[%]	15	15	15	13	21
Amb. density	[kg/m^3]	22.8	22.8	22.8	22.8	22.8
Amb. pressure	[MPa]	5.63	5.98	6.62	6.04	5.91
Injection duration	[ms]	6	6	6	6	6

Table 5.2. Case set-up for constant volume vessel simulations for Spray-H

fuel		n-epthane	
Amb. temp.	[K]	1000	1000
O_2 molar fract	[%]	15	15
Amb. density	[kg/m^3]	14.8	30
Amb. pressure	[MPa]	4.25	8.7
Injection duration	[ms]	6.8	6.8

thickness can be quantitatively related to the soot volume fraction, f_v, along the path of the laser using small particle Mie theory [69].

PLII images were obtained by passing a thin (0.3 mm) Nd:YAG laser sheet (532 nm) through the fuel jet centreline. The PLII signal was imaged with an intensified CCD camera (50 ns gate) with Nikkor 105 mm, f/2.8 lens, a 450 nm short-pass filter, and a zero-incidence 532 nm laser mirror.

An example of chemiluminescence, PLII and laser extinction images is reproduced in fig. 1.7.

The soot models and their responses to variations of ambient conditions are validated against the set of environment conditions summarized in tab. 5.1 for Spray-A and in tab. 5.2 for Spray-H, which reproduce the operating conditions typical of a Diesel engine.

5.2 Spray set-up

The spray evolution in the combustion vessel is described by the Lagrangian solver presented and validated by Lucchini et al. in [70] and implemented in the Lib-ICE library. This solver is based on the Eulerian-Lagrangian approach, widely used because it represents an acceptable compromise in terms of computational time and accuracy. The gas-phase is described using the RANS equations (Eulerian approach). The liquid spray is assumed to be made up by a discrete number of parcels, each one formed by an ensemble of droplets with the same physical properties; the properties of each parcel are determined for each time step by solving conservation equations in the Lagrangian way. The two phases are coupled because momentum, energy and mass are exchanged. Namely, the effect of the gas-phase on the dispersed liquid is accounted for by evaluating gas quantities at parcel location with interpolation techniques presented in [69] whereas the source terms of the RANS equations of each

grid cell are obtained by summing the rate of change of mass, momentum and energy of all drops inside the cell at a defined time step.

In this work, Blob-injection model [71] is employed to define the starting conditions of the first drops at the nozzle exit. It assumes that fuel is introduced in the combustion chamber as big spherical droplets with uniform size, equal to the nozzle diameter, and the number of drops injected per unit time is determined from the mass flow rate. Primary and secondary break-up (for more details about spray regimes see [13, 14, 72] are described by the KH-RT model, a combination of the Kelvin-Helmholtz model [71] and the Rayleigh-Taylor model [73], which are here briefly presented.

5.2.1 The Kelvin-Helmholtz break-up model

Reitz [71] applied his wave-breakup model, based on a first order linear analysis of a Kelvin–Helmholtz instability growing on the surface of a cylindrical liquid jet, to describe break-up of droplets. Such instabilities start to grow on the surface of blobs and also of droplets subsequently generated. The fastest growing wave with growth rate Ω_{KH} and wavelength Λ_{KH} are responsible for the detachment of the new child drops, with radius r_{new}, from the surface of the parent drop of size r. Ω_{KH} and Λ_{KH} depend on the parent drop radius, relative velocities, densities of liquid and gas phases, surface tension and kinematic viscosity of liquid, grouped in several non-dimensional numbers. Their expressions can be found in [71]. The size of the new droplets is proportional to the wavelength Λ_{KH}:

$$r_{new} = B_0 \cdot \Lambda_{KH} \tag{5.2}$$

where $B_0 = 0.61$ is a constant. A new parcel containing product drops of size r_{new} is created and added to the computation. The parent drop continues to loss mass and rate with which it reduces its size is given by

$$\frac{dr}{dt} = \frac{r - r_{new}}{\tau_{KH}} \qquad \tau_{KH} = 3.788 \cdot B_1 \frac{r}{\Lambda_{KH} \cdot \Omega_{KH}} \tag{5.3}$$

where τ_{KH} is the characteristic break-up time. If the KH model is used in combination with the blob method, the influence of the nozzle hole flow on primary break-up is not modelled satisfactorily. B_1 is a constant that should be adjusted to match experimental data of spray penetration and including the influence of the nozzle flow like turbulence level and nozzle design on spray break-up. A wide range of values is proposed in the literature: B_1 varies from 1.73 to 60. A higher value of B_1 should lead to reduced break-up and increased penetration, while a smaller value results in increased spray disintegration, faster fuel-air mixing, and reduced penetration [72].

5.2.2 The Rayleigh-Taylor break-up model

It is known that liquid droplets in Diesel sprays have very high initial velocities, and decelerate rapidly due to drag forces. In this case, Rayleigh–Taylor instability may also play an important role on droplet breakup mechanisms in addition to the Kelvin-Helmholtz instability [74]. Since the disintegration of drop is induced by the

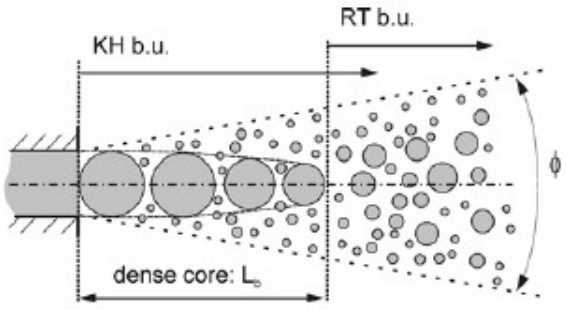

Figure 5.3. Schematics of KH-RT break-up model. [72]

inertia of the liquid and by the action of aerodynamic drag forces, unstable waves grow on the back side of the drop. The expressions of growth rate Ω_{RT} and the corresponding wave number K_{RT} of the fastest growing wave can be found in [75]: they are derived from the expressions of drag force and acceleration of gas-liquid interface. The wavelength Λ_{RT} is obtained by

$$\Lambda_{RT} = \frac{2\pi C_{RT}}{K_{RT}} \tag{5.4}$$

The wavelength Λ_{RT} is compared to drop radius and, if $\Lambda_{RT} < r$, it is assumed that RT waves have started to grow on its surface. The life time of RT waves is then tracked from then on, and when it exceeds the characteristic RT time τ_{RT} catastrophic break-up occurs and small droplets with radius r_{new} are created where

$$r_{new} = \frac{\pi C_{RT}}{K_{RT}} \qquad \tau_{RT} = \frac{C_\tau}{\Omega_{RT}} \tag{5.5}$$

C_{RT} and C_τ are adjustable model constants that vary in order to match experimental characteristics of the spray. Similar to the constant B_1 in the KH model, C_{RT} includes the unknown effects of initial conditions like turbulence and cavitation inside the nozzle hole on the secondary break-up. By increasing its value, break-up is reduced and the size of the new droplets is increased.

5.2.3 The Blob-KH/RT model

If the blob-method is utilized in order to inject initial drops into the numerical grid, usually two secondary break-up models are used. In the case of the KH-RT model, both KH and RT models are allowed to grow unstable waves simultaneously, and if the RT-model predicts a break-up within the actual time step, the disintegration of the whole drop according to the RT mechanism occurs. Otherwise the KH model will produce small child droplets and reduce the diameter of the parent drop [72]. Since the rate of reduction of droplet size by the RT model is too high, if it is applied to drops just leaving the nozzle hole, the model is switched off within the so-called break-up length L_b and only KH stripping break-up is allowed to occur near the nozzle, as shown in fig. 5.3.

The expression of the break-up length is given by

$$L_{bu} = C_{bu} \cdot \sqrt{\frac{\rho_l}{\rho_s}} \cdot d_{noz} \tag{5.6}$$

By varying the constant C_{bu}, the distance at which the break-up RT is activated can be established. Compared to the single use of the KH model, a faster disintegration of big drops is achieved, and an increased evaporation as well as a reduced penetration are calculated allowing a better matching of experimental data.

In this work, values of constant presented above, for constant vessel simulations, are reported in tab. 5.3.

Table 5.3. Spray constant values

B_1	C_τ	C_{RT}	C_{bu}
23.5	1	0.5	5

5.3 Discretization method

In order to be solved, the set of partial differential equations (PDE) that describe the continuum mechanics problem has to be discretized, i.e. it has to be approximate by a system of algebraic equations. This transformed set is then solved at discrete locations in space and time.

In OpenFOAM, discretization is performed according to the "Finite Volume" method whose starting point is the integral form of the conservation equations. The computational domain is then subdivided into a finite, but not always fixed, number of control volumes, called cells. These cells are contiguous, which means that they do not overlap one another, and the ensemble of spatial locations of their vertices is named *mesh*. The computational grids used in this work are described in details in the next section. The conservation equations are applied to each cell centroid and most volumes integrals are converted to surface integrals through the Gauss theorem. Finally, all terms are linearised with appropriate schemes. The result is a set of algebraic equations for each cell, ready to be integrated over the chosen time step by a suitable method.

In this work, time step duration is kept constant at run-time and equal to 2.5e-7 s.

OpenFOAM offers a wide selection of discretization schemes for every terms that appear in the equations and those used in this work are summarized in tab. 5.4. Detailed information about the discretization techniques can be found in [76].

Table 5.4. Discretization methods for constant volume vessel simulations.

$\frac{\partial \varphi}{\partial t}$	Euler
$\nabla \varphi$	Gauss linear
$\nabla \cdot \varphi$	Gauss limited linear 1
$\nabla^2 \varphi$	Gauss linear corrected

The discretized algebraic equations are still non-linear; therefore iterative solvers, based on the "Conjugate Gradient" algorithm, are chosen among those available in OpenFOAM. Besides, in order to achieve fast convergence, the solving process is preceded by pre-conditioning.

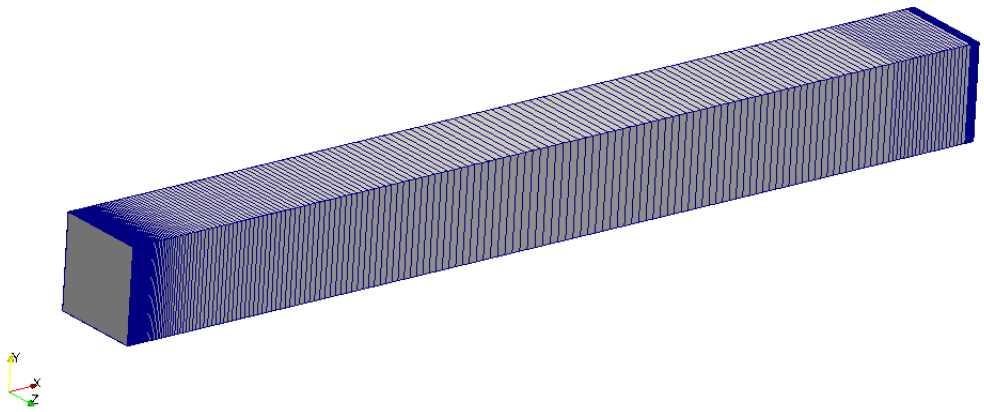

Figure 5.4. Flamelet domain finite-volume mesh.

The Pre-conditioned Conjugate Gradient (PCG) solver, developed for symmetric matrices, is used for the continuity equation (2.9), the flamelet equations (2.19) and (2.20) and the pressure equation in the PISO loop. The associate pre-conditioner is based on Diagonal Incomplete Cholesky (DIC) algorithm. For equations with convective terms which cause matrices to be asymmetric, an evolution of the PCG algorithm, the Pre-conditioned bi-Conjugate Gradient (PBiCG) algorithm, is used along with a Diagonal Incomplete Lower-Upper (DILU) pre-conditioner. Further explanations of the solvers and pre-conditioners employed in this work are provided by [77].

5.4 Mesh set-up

For each simulations performed in this work, two different meshes are used: the one discretizing the physical space and the ones representing the flamelet domains, which are strictly coupled with the combustion model.

Although their one-dimensional nature, flamelet domains (fig. 5.4) are treated as particular finite volume domains, in order to use the same tools implemented in OpenFOAM for solving both the flow and the flamelet equations. Flamelet domains, one per each flamelet present in the computational domain, are made up of 270 cells and remain unchanged run-time. The x axis corresponds to the Z coordinate in the flamelet domain and its boundaries represent the oxidizer side (x = 0) and the fuel side (x = 1). A refinement of the cells near the boundaries in the x direction is required for the β-PDF integration. Indeed, as discussed in section 2.3.1, the β-PDF for young flamelets has strong decreases at the oxidizer size and comparable increases at the fuel side, thus enhanced local refinement is unavoidable to accurately discretize the probability density function of the mixture fraction and overcome numerical drawbacks as referred in [78].

For constant volume vessel simulations, as a symmetric spray arrangement is

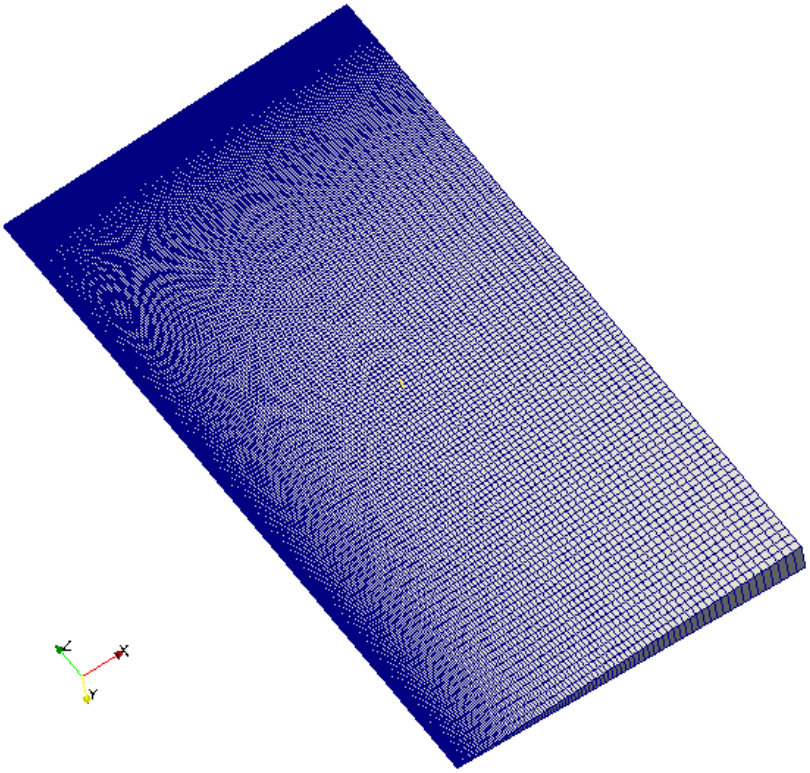

Figure 5.5. Constant volume vessel finite-volume mesh.

considered, a wedge grid with five degree angle of size 4.7108 mm × 53.95 mm × 108 mm is employed. The mesh is composed by 23328 hexahedral cells and does not change during the simulation. A constant grading is used which leads a refined mesh close to the nozzle to perform a better coupling of the Lagrangian and Eulerian fields in the spray solver. The constant volume mesh is depicted in fig. 5.5.

5.5 Chemistry set-up

In the performed simulations, skeletal mechanisms are used to describe chemistry of n-dodecane and n-heptane. The chemical mechanism for n-dodecane is based on the skeletal mechanism developed by Luo et al. in [79], which consists of 106 species and 420 reactions, with an addiction, proposed by Hawkes, of a 5 species reaction mechanism for OH* made up of 13 reactions and 34 reactions for CH, CH_2, C_2H and CH_2(s) extracted from [80]. The skeletal mechanism for n-heptane is derived by Lu in [81] and is composed of 68 species and 283 reactions.

The reaction mechanisms are provided to chemistry solver in CHEMKIN format, where stored data are used to evaluate the molar reaction rate $\dot{w}_i$ for the generic species i with the standard Arrhenius expression:

$$\dot{\omega}_i = A_i T^{\beta_i} exp\left(\frac{E_i^{act}}{RT}\right) \tag{5.7}$$

The mass reaction rate is then calculated as

$$\dot{m}_i = \frac{y_i^*(t+\Delta t) - y_i(t)}{\Delta t} = \frac{\int_t^{t+\Delta t} \dot{\omega}_i \frac{W_i}{\rho} dt'}{\Delta t} \tag{5.8}$$

where y_i^* and y_i are respectively the updated and the current species mass fractions, W_i is the molecular weight of species i, ρ is the density and Δt is the selected chemical time step. The solution of eqn. (5.8) is carried out by a multi-step, Semi-Implicit Bulirsch-Stoer (SIBS) method, a stiff ODE solver described in [82], and it is performed for every species and in each cell of the flamelet domain. The resulting reaction rates m_i are then included in the flamelet equations as source terms.

5.6 Reduction of computational time

Incorporating detailed chemical mechanisms into ICE simulations is a fundamental prerequisite for predictive combustion models, particularly for reliable forecasts of flames and emissions. However, the use of comprehensive chemical kinetics gives rise to a large system of non-linear stiff ordinary equations for each computational cell, which is solved by a proper ODE stiff solver with demanding CPU times.

The RIF approach solves the reaction-diffusion in the one-dimensional mixture fraction space, therefore reducing the number of cells on which chemistry integration is performed and limiting the time required for calculations. Anyhow, as reported in [83], complex kinetics mechanisms cause high computational overheads, especially when chemistry has to be solved for a high number of flamelets and because of the PDF integration of the chemical species. Thus, to properly account for full chemistry, tabulation and reduction mechanisms have been employed in this work, along with a virtual species approach to shorten the time spent with PDF integration.

5.6.1 Tabulation and reduction algorithm

The In-situ Adaptive Tabulation (ISAT), firstly developed by Pope [84], is an algorithm that stores results of integration of the chemical stiff ODE system and all the required data to retrieve them. Differently from all traditional tabulation techniques, the table is not built-up in a pre-processing stage but rather during the reactive flow calculations.

It is now necessary to introduce a few definition which will be useful in the subsequent explanation of the ISAT algorithm.

The thermochemical state of a fluid flow is completely defined by the composition φ, which groups species mass fraction, pressure and temperature: $\varphi = [y_i, p, T]$. The composition is therefore a vector in the multidimensional composition space. The solution of the reaction equations for a fixed time step Δt and a given initial composition φ_0 is called reaction mapping $\mathbf{R}(\varphi_0) = \varphi(t_0 + \Delta t)$ and is a unique function of φ_0.

The accessed region is defined as the set of compositions that occurs in the flow and it is the one tabulated in the ISAT algorithm. Clearly, the accessed region is not known prior calculations and thus the table is constructed runtime. Given a query

point φ_q, with a $\delta\varphi$ displacement from the initial condition such that $\varphi_q = \varphi_0 + \delta\varphi$, the corresponding reaction mapping $\mathbf{R}(\varphi_q)$ can be computed as a linear approximation

$$\mathbf{R}(\varphi_q) = \mathbf{R}(\varphi_0) + \delta\mathbf{R} \simeq \mathbf{R}_l(\varphi_q) = \mathbf{R}(\varphi_0) + \delta\mathbf{R}_l \tag{5.9}$$

where $\delta\mathbf{R}_l = A(\varphi)\delta\varphi$, being A the mapping gradient matrix related to sensitivity coefficients.

The linear approximation is valid within the region of accuracy (ROA), defined as a connected region containing φ_0 and all the φ_q for which the local error, ε_{local}, does not exceed the user-specified tolerance, ε_{ISAT}:

$$\varepsilon_{local} = |\mathbf{R}(\varphi_q) - \mathbf{R}_l(\varphi_q)| = |\delta\mathbf{R} - \delta\mathbf{R}_l| \leq \varepsilon_{ISAT} \tag{5.10}$$

The ROA is not computed according to its definition in eqn. (5.10) but rather approximated by a conservative hyper-ellipsoid called ellipsoid of accuracy (EOA).

The table generated by the ISAT algorithm during calculation consists of a binary tree, with "leaf" that stores φ, $\mathbf{R}(\varphi)$, A(φ) and EOA and "nodes" where cutting hyperplanes with all informations required to scan the tree are gathered.

For each query φ_q, the binary tree is traversed until a leaf with a composition φ_0 close to φ_q is reached. Then, one of the following operation is performed:

1. *retrive*: if φ_q is within the EOA of φ_0, the linear approximation is returned;

2. *growth*: if φ_q is not within the EOA but the corresponding $\mathbf{R}(\varphi_q)$ determined by direct integration of the ODE system belongs to the region of accuracy according to eqn. (5.10), $\mathbf{R}(\varphi_q)$ is returned and the EOA is grown;

3. *adding*: if φ_q is not within the EOA and the corresponding $\mathbf{R}(\varphi_q)$ determined by direct integration do not belongs to the region of accuracy, $\mathbf{R}(\varphi_q)$ is returned and a new leaf is added.

The mechanisms of reduction have been developed on the observation that for most practical reaction problems, much less than all the species held by the chemical mechanism act a pivotal role in the combustion process. Therefore, such approach eliminates unimportant species and reactions from the detailed mechanism.

The Direct Relation Graph (DRG) method was originally proposed by Lu and Law in 2005 [85] as a pre-processing tools. The DRG algorithm constructs a graph where each vertex represents a species present in the full mechanism and each direct edge stands for the immediate dependence of one species to another. The direct connection between two species is quantified by the normalized contribution that measures the error on the production and consumption of a species when another is removed from the mechanism: a direct path is obtained only if the normalized contribution is greater than or equal to a user specified threshold value ε_{DRG}.

The Dynamic Adaptive Chemistry (DAC) is based on the DRG method but was developed by Liang et al. in [86] to perform a runtime reduction, rigorously valid for local and instantaneous conditions. In order to overcome the drawback of the binary truncation performed by DRG, which causes a loss of considerable information about contribution strength, an error propagation control has been implemented in the DAC algorithm: the connection path strength, defined as the maximum chain product

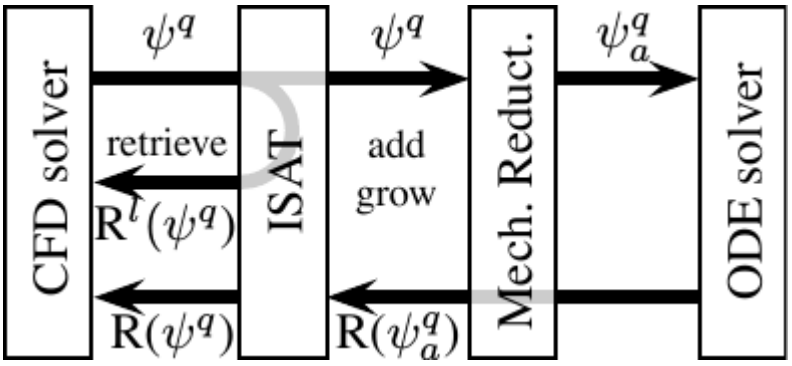

Figure 5.6. Structure of the TDAC algorithm, reproduced from [70].

among all possible paths of the normalized contributions of the edges along the given path, is evaluated and a species is preserved if the connection path strength is larger than a user-defined threshold value ε_{DAC}. A set of active species is then determined starting with selected major species and a reaction is included in the mechanism only if all the reactants and products are active species. The ordinary differential equations are formulated with respect to only active species, therefore leading to a more compact ODE system. However, when reaction rates for active species are evaluated, all species are considered so that third body effects are accounted [86].

In the context of ICE simulations, the mixture inhomogeneities and the sever changes in thermodynamic conditions reduce the effectiveness of the tabulation and reduction methods. Therefore, to achieve a satisfactory speed-up factor, the two approaches have been combined by Contino et al. [87]. With the aim to better applying to the large range of thermochemical conditions encountered in internal combustion engines, the ISAT algorithm has been adapted. The table is periodically cleaned up according to user specified parameters: a stored point is removed after N_{ms} time steps, i.e. when is deemed too old, and the stored composition centre in φ_0 is replaced by the one centre in φ_q after N_{mg} growths, refocusing the EOA. In addition, the maximum size is limited to avoid memory issues and too slow retrieves, clearing and repopulated the table with the most recently used list. Furthermore, the DRG algorithm has been modified such that it can be performed runtime to more efficiently match with ISAT algorithm.

The coupling of ISAT and reduction methods is performed by TDACChemistryModel solver, implemented into the Lib-ICE code by the ICE group of Politecnico di Milano. Figure 5.6 shows schematically how this algorithm works.

When ISAT algorithm receives a query point φ_q, it first attempts to retrieve the corresponding linear mapping $\mathbf{R}_l(\varphi_q)$. If it fails, the ISAT provides φ_q to the reduction mechanism which finds the reduced mechanism at runtime and supplies the set of active species φ_q^a to the stiff ODE solver. This solver computes the reaction mapping $\mathbf{R}(\varphi_q^a)$ which is used by ISAT to add or grow the binary tree and to build the reaction mapping $\mathbf{R}(\varphi_q)$ in the full composition space.

5.6.2 The virtual species approach

The virtual species approach has been specifically developed for the RIF combustion model, with the aim to properly employ detailed chemistry but, at the same time, avoid accounting for all the species in the geometry domain. A reduced set of chemical species is considered in the mixture fraction space and the corresponding composition is computed to consistently preserve both mass and thermodynamic properties of the entire set of chemical species used in each flamelet. The PDF integration is performed only for the virtual composition in a limited amount of CPU time. Details can be found in [83].

Chapter 6

Results and discussion: constant volume vessel validation

In this chapter, results of soot models validation in the constant volume vessel are presented. First, a preliminary analysis was carried out in order to determine the optimum set of tolerances for the chemistry solver and, thus, to speed-up the following simulations.

The validation has been performed with the RIF combustion model using a single flamelet and then with multiple flamelets approach. Indeed, as the soot formation and oxidation are strictly related to the kind of combustion and to its characteristics, an accurate combustion model, which is able to well reproduce all the combustion phenomena, represents the basis for reliable soot prediction. Based on this observation, multiple RIF approach compared to single RIF model provides significant improvements in the computation of the flame structure, particularly in the prediction of the lift-off length, as carefully discussed in [88].

6.1 Optimization of chemistry solver tolerances

A preliminary investigation was performed to determine the optimum set of tolerances of the odeTDAC solver, i.e. the best compromise between reduced computational time and accuracy of results. As described in section 5.6.1, the odeTDAC solver manages the coupling of the ISAT algorithm with the chosen reduction mechanism and the ODE stiff solver. Therefore, the aim of this analysis is to define an optimal combination of tolerances for the ISAT algorithm, the DAC or DRG mechanism and the SIBS solver, which respectively fix the region of accuracy, the minimum connection path strength or the minimum normalised contribution and the maximum error between the actual and approximate solution. The investigation was carried out in the constant volume vessel introduced in section 5.4 at ambient conditions summarized in table 6.1.

The RIF model with one flamelet and the Moss model have been used to simulate the combustion and the soot processes, respectively. The end time was set to 1.3 ms, when diffusive combustion regime has stabilized, as it was seen in a test simulation with the same ambient conditions.

Simulations were performed on a 2 processors Pentium (R) Dual-Core CPU T4300

Table 6.1. Ambient conditions for chemisitry solver tolerance optimization

fuel	Amb. temperature [K]	O_2 molar fraction [%]	Amb. pressure [MPa]
n-dodecane	900	15	5.94

@ 2.10 GHz.

In order to account for possible interferences between the different reduction mechanisms, the tabulation and the ODE solution, two different sets of simulations have been performed: one with DAC algorithm, called TDAC, and the other with DRG method, called TDRG. The sets are constructed by defining default values of each tolerance and by changing one-by-one; therefore, a sub-set is defined by keeping two tolerances at their default values as the third is varied. For each set, the execution time has been evaluated and the accuracy of the results in terms of average pressure and species trends in the mixture fraction domain has been determined by comparison with a reference simulation without tabulation and reduction mechanisms. Particularly, temperature, species connected to sooting processes according to the Moss model, namely C_2H_2 and OH, and the main oxidation products, CO_2 and CO, have been taken into account.

6.1.1 TDAC analysis

In the TDAC analysis, the values of the tolerances are chosen in agreement with [83]. In tab. 6.2 default values are displayed in the first column whereas their variations are shown in the remaining columns.

Table 6.2. Tolerance values for TDAC analysis. The default values are displayed in the first column.

ε_{ISAT}	1e-06	1e-04	1e-02
ε_{DAC}	1e-03	3e-02	1e-01
ε_{ODE}	1e-06	5e-04	1e-03

Table 6.3 shows the computational time for the simulations of each sub-set.

As it was expected, the computational time is reduced by incrementing the values of the tolerances. Further investigations on average pressure reveal no significant difference with changing the tolerance for the ISAT algorithm and the SIBS solver. Conversely, by increasing the tolerance at the value of 3e-2 for the DAC method there is a notable reduction of the ignition delay and for value equal to 1e-1 no ignition is detectable, as can be inferred by fig. 6.1. Indeed, as suggested by Liang et al. in [86], the ignition stage is a complex chemical phenomenon and it requires a high number of species and reactions to be correctly predicted.

During the analysis, an interference between the soot model and the chemistry solvers has been pointed out. Deeper investigations were conducted and by switching off the oxidation in the soot model, different species trends, both involved in the sooting and in the combustion processes, have been found out. This outcome is

Table 6.3. Execution times of TDAC analysis. "Default" refers to the simulation with all tolerances at their default values as reported in tab. 6.2.

		Default	
Exec. time	[min]	1253	
ε_{ISAT}		1e-04	1e-02
Exec. time	[min]	1056	594
ε_{DAC}		3e-02	1e-01
Exec. time	[min]	965	528
ε_{ODE}		5e-04	1e-03
Exec. time	[min]	662	652

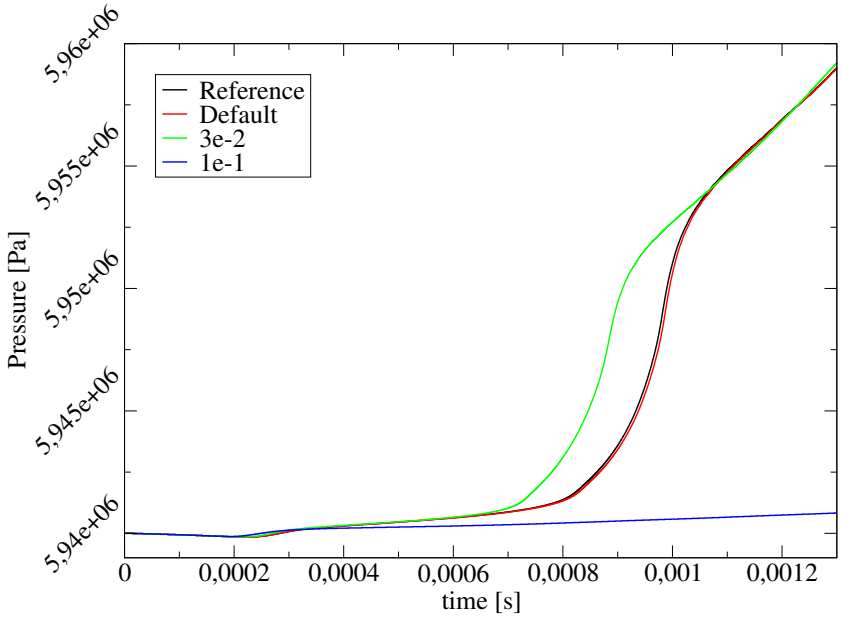

Figure 6.1. Pressure trends for TDAC analysis.

unexpected because each soot model developed in this study works unidirectionally by taking results of the flamelet equations for acetylene and hydroxide; no reverse effect is accounted, i.e. consumption of C_2H_2 and OH is not considered.

6.1.2 TDRG analysis

In the TDRG analysis, the selected values of the tolerances are shown in tab. 6.4, where default values are grouped in the first column. Values for the DRG tolerance are chosen according to [86].

Results in terms of executional time are compared in tab. 6.5. Significant reduction of computational time is provided by raising the tolerance of the ODE solver from 1e-6 to 5e-5 with a decrease of almost 7 hours.

In fig. 6.2, a good overlap of pressure trends is noticeable between the default simulation and the reference simulation but no important deviations are detectable in the other cases, for which there is a slight increase of the ignition delay.

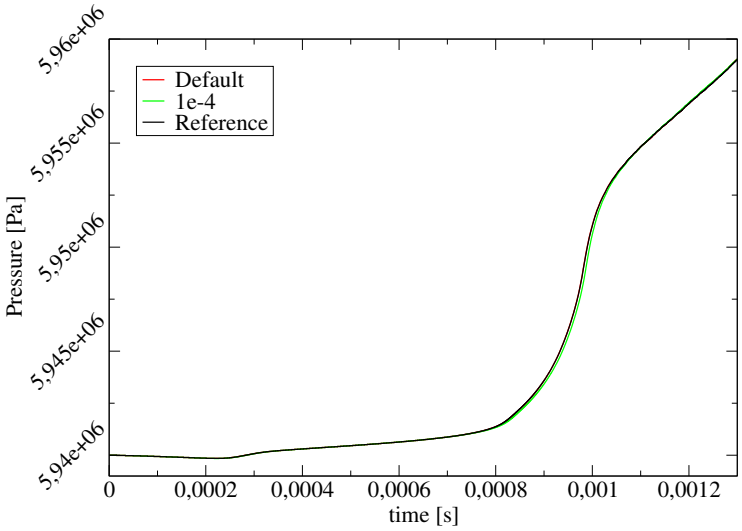

(a) ISAT tolerance analysis.

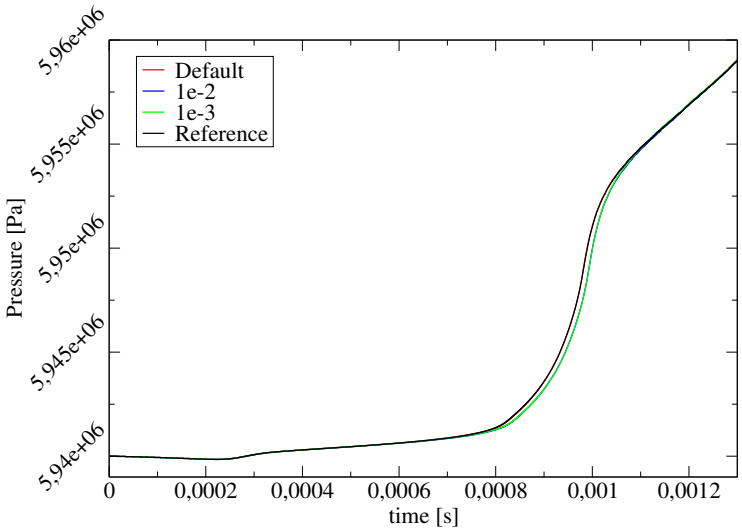

(b) DRG tolerance analysis.

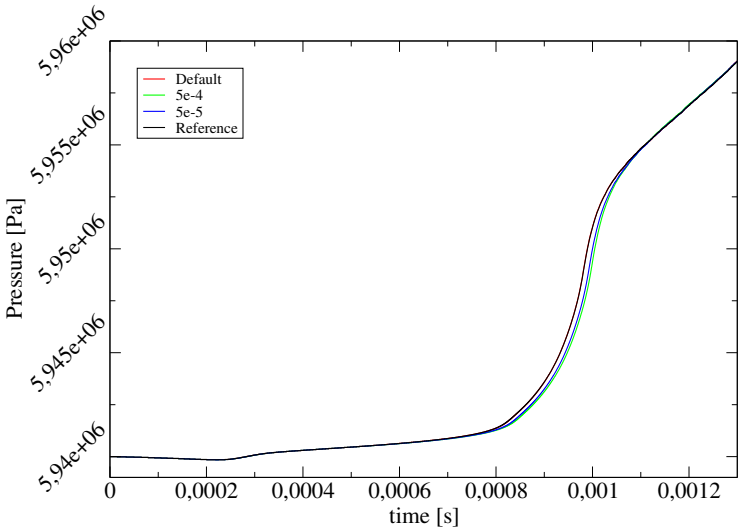

(c) ODE tolerance analysis

Figure 6.2. Pressure trends for TDRG analysis

Table 6.4. Tolerance values for TDRG analysis. The default values are displayed in the first column.

ε_{ISAT}	1e-06	1e-04	
ε_{DRG}	1e-04	1e-03	1e-02
ε_{ODE}	1e-06	5e-05	5e-04

Table 6.5. Execution times of TDRG analysis. "Default" refers to the simulation with all tolerances at their default values as reported in tab. 6.4.

		Default	
Exec. time	[min]	1062	
ε_{ISAT}		1e-04	
Exec. time	[min]	931	
ε_{DRG}		1e-03	1e-02
Exec. time	[min]	999	966
ε_{ODE}		5e-05	5e-04
Exec. time	[min]	640	600

This behaviour can also be observed in the species profiles in the mixture fraction domain. Indeed, no differences are evidenced between the reference and the default simulations whereas small offsets are detected at ignition stage for the other simulations, which vanish when diffusive regime establishes. By way of example, fig. 6.3 collects species and temperature trends for different subsets at 0.9 ms and 1.3 ms, respectively close to ignition and almost at the beginning of the diffusive stage.

No interference has been seen between the soot model and the chemistry solvers.

Based on the above analysis, ISAT algorithm combined with DRG and the set of tolerances listed in tab. 6.6 will be used in all the following calculations. It is believed that the selected set represents the best compromise between accuracy and limited computational time.

Table 6.6. Set of tolerances selected.

ε_{ISAT}	ε_{DRG}	ε_{ODE}
1e-6	1e-04	5e-05

6.2 Validation of the soot models with single RIF model

In the first part of this work, validation of the three soot models described in chapter 3 is performed by combustion simulation with single RIF model, due to its simplicity and its limited computational cost.

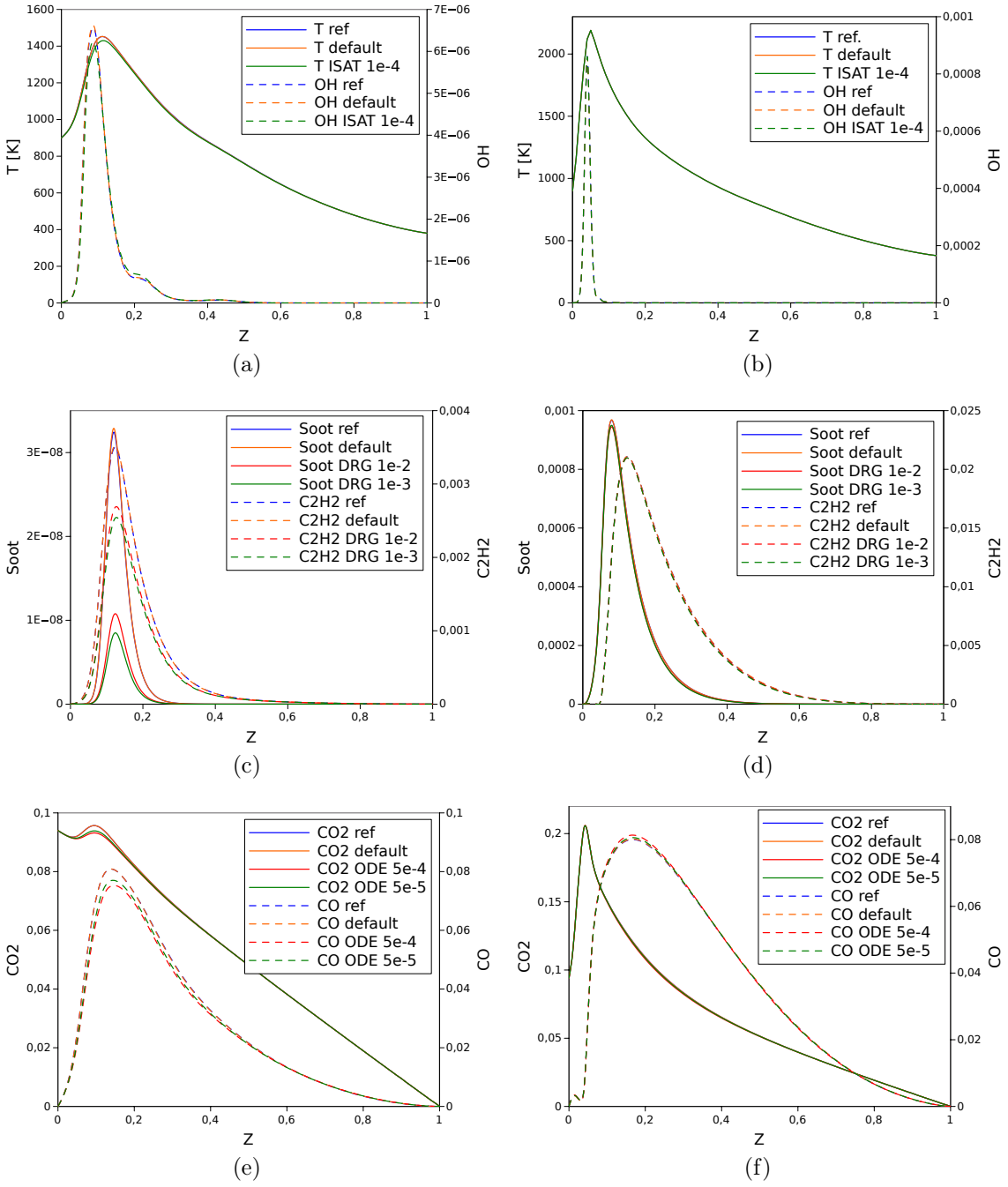

Figure 6.3. Temperature (left axis) and OH mass fractions (right axis) in the mixture fraction domain for ε_{ISAT} are reported in (a) and (b). C_2H_2 (left axis) and soot (right axis) mass fractions in the mixture fraction domain for different ε_{DRG} are shown in (c) and (d). CO_2 (left axis) and CO (right axis) mass fractions in the mixture fraction domain for ε_{ODE} are depicted in (e) and (f). Trends at 0.9 ms and 1.3 ms are respectively reported on the left (a) and on the right (b).

First, simulations at a reference set of ambient conditions have been carried out in order to assess the ability to predict soot of the aforementioned models in an acceptable time. Then, validation of the models that has shown good results in the initial analysis is presented for the conditions reported in tables 5.1 and 5.2. Simulations were performed on a 2 processors Pentium (R) Dual-Core CPU T4300 @ 2.10 GHz.

6.2.1 Validation of soot models at reference conditions

The set of ambient conditions selected for this early analysis are summarized in tab. 6.7 with the measured values of the lift-off length and ignition delay provided by Sandia National Laboratories [69].

Table 6.7. Reference ambient conditions for the comparison of the soot models.

Fuel	Ambient temp. [K]	O_2 mole fraction [%]	Ambient density [kg/m^3]	Injected mass [mg]	Lift-off length [mm]	Ignition delay [ms]
$nC_{12}H_{26}$	900	15	22.8	14	16.1	0.4

Flame structure

The natural emission image for quasi-steady combustion at reference ambient conditions reproduced from [69] is shown in fig. 6.4.

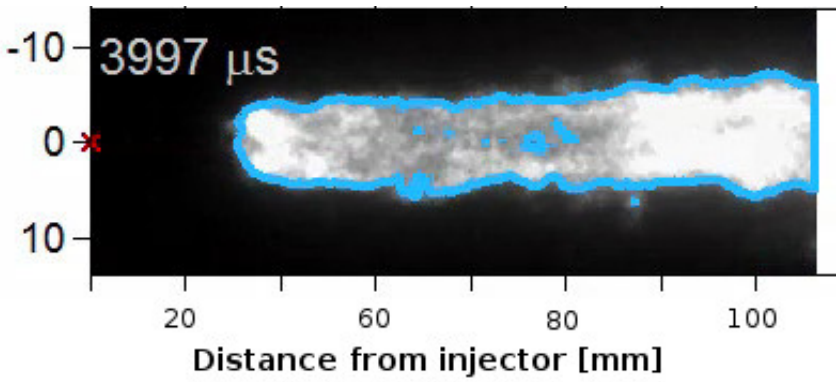

Figure 6.4. Natural luminosity image for the quasi-steady combustion at reference ambient conditions.

The flame is surrounded by a blue line which corresponds to the stoichiometric diffusion flame defined by the 50% of OH* chemiluminescence threshold. The luminosity is dominated by OH* chemiluminescence near the lift-off length, which represents the cold rich premixed flame, but includes some soot incandescence contribution downstream where the diffusive flame enclosed the entire head vortex.

The volume of the Sandia combustion vessel and that of the simulated combustion chamber are different (see chapt. 5). Therefore, comparison between experimental

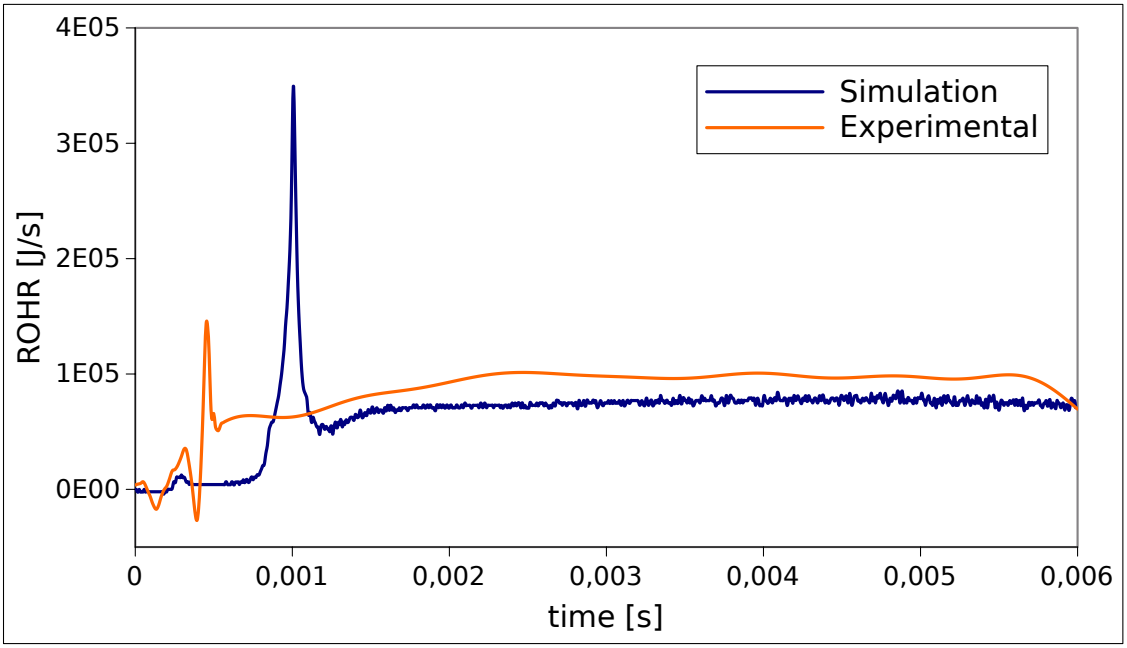

Figure 6.5. Rate of heat release comparison between experimental and computed values with single RIF combustion model for reference conditions.

and simulated pressure traces is not strictly correct. The measured and the calculated rates of heat release (ROHR), shown in fig. 6.5, are, instead, independent from volume and are compared in place of pressures.

Although the same fuel quantity injected, the calculated ROHR is slightly smaller than the measured one. The main reason for this difference is that the first one accounts for heat losses because it was obtain from pressure derivative. The single RIF model overestimates the ignition delay which is close to 0.9 ms. In general, the overestimation of ignition delay provided by RIF model is due to the excessive computed values of scalar dissipation rate during the early stages of injection: for longer than expected, the scalar dissipation rate remains higher than the extinction threshold value, delaying the fuel auto-ignition.

Figure 6.6a displays the computed temperature and OH fields at 4 ms. The maximum values of temperature and OH are distributed around the profile of stoichiometric mixture fraction and especially towards the top of the flame. The stoichiometric mixture fraction and the OH distribution determine the position of the diffusive flame, which extends up to the nozzle. This means that RIF model with only one flamelet is not able to reproduce lifted flames. This is basically due to the single one-dimensional flame structure which describes the entire physical domain. The mixture fraction is the unique transported variable related to the flame, implying that, once the first injected fuel is auto-ignited, the last injected fuel already vaporized near the nozzle ignites immediately. This constitutes a relevant drawback in the simulation of diesel combustion and in particular for soot formation processes, in which the presence of the lift-off represents the fundamental aspect in the formation of air-fuel mixture that undergoes first premixed combustion and then diffusive one.

In fig. 6.6b the mixture fraction and the acetylene fields in the physical domain

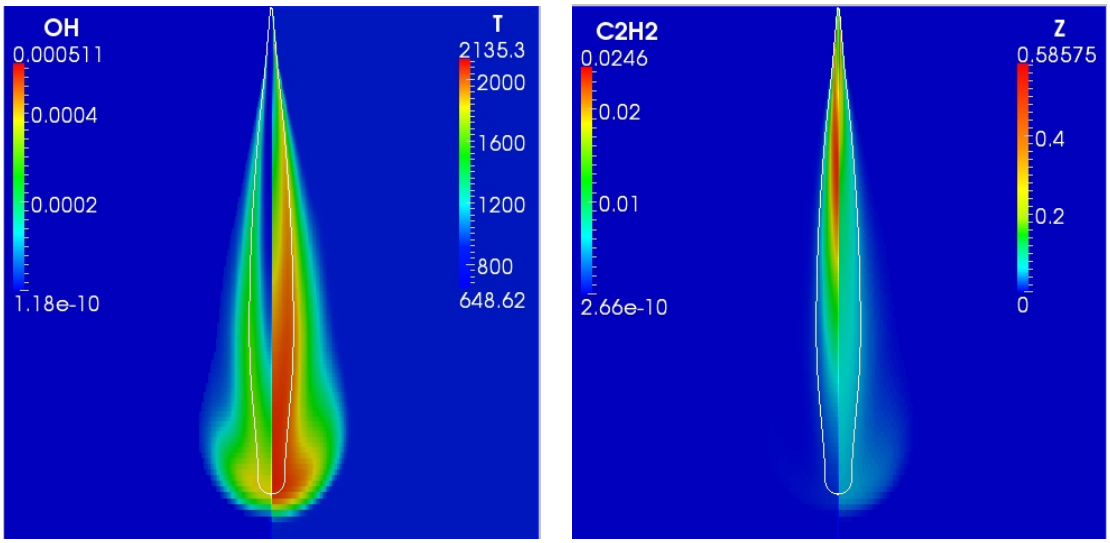

(a) Computed OH mass fraction (left) and temperature fields (right).

(b) Computed C_2H_2 mass fraction (left) and mixture fraction fields (right).

Figure 6.6. Computed species mass fraction and temperature fields for the reference case at 4 ms. The white line points the stoichiometric mixture fraction contour.

are reported. Due to the absence of lift-off, the pyrolysis and rich-combustion zones, pointed by the high values of Z and C_2H_2 concentration, extend up to the nozzle. This implies that, in the same operating conditions, higher amounts of C2H2 and larger area of soot nucleation are present compared to a lifted flame.

At this point, it is worth to underline that the aim of this analysis is not to obtain an excellent quantitative agreement of soot yield with experimental measurements, but to evaluate the qualitative response of the soot models with a flamelet approach to variations in ambient conditions because this is what is expected by a semi-empirical model. Therefore, conducting this parametric analysis initially with one flamelet allows to realize a first simpler validation of the flamelet soot models, despite the shortcomings listed in the flame modeling the flame.

Soot model comparison

Because soot models are practically unidirectional and a sub-model for soot radiation is not present in this work, they do not influence the structure of the flame described early. This approximation is much less acceptable as increases the soot load of the flame. In the spray-A conditions the amount of soot is relatively low and it allows, at least for the aim of our analysis, the use of this kind of approach.

Figure 6.7 shows the distribution in physical domain of soot particle number density, n_{soot} [particles/m^3] at 4 ms for the three soot models considered. All models are characterized by a rapid saturation in the maximum values as indicated by the Moss in his [1] because a local balance is established between nucleation and coagulation. Regions with higher particle density are located further downstream than the area in which the maximum values of C_2H_2 concentration are present. This is consistent with what is described by the conceptual model of Dec and it

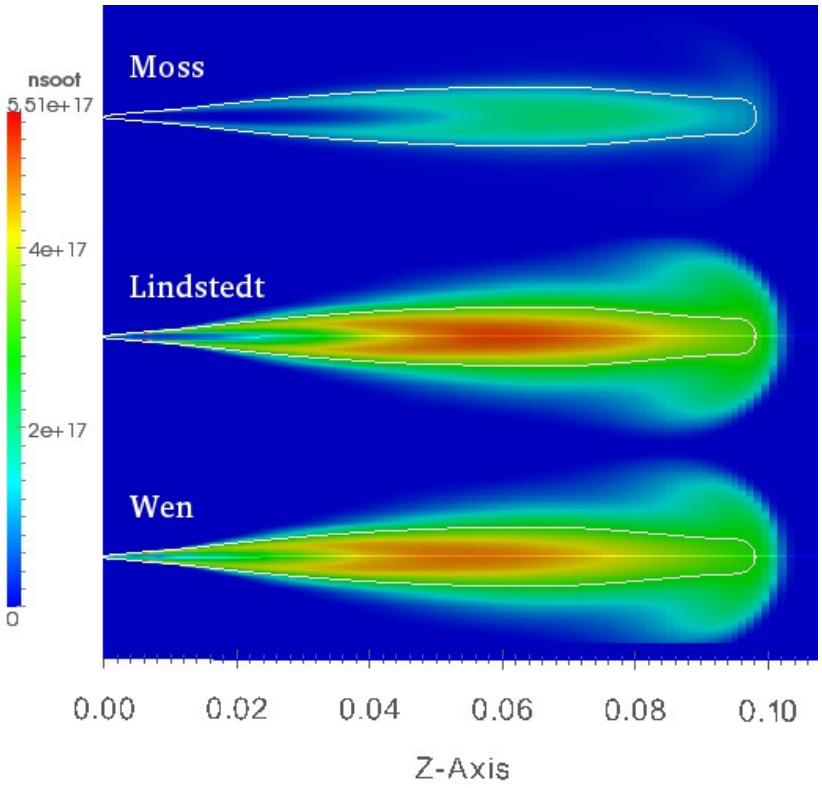

Figure 6.7. Soot particle density fields for the models of Moss, Lindstedt and Wen for the reference case at 4 ms. The white line points the stoichiometric mixture fraction contour.

is due to the convective transport by the jet and to the strong dependency of the nucleation process from temperature. With the model of Moss, lower values and less extensive region of high soot particle number density are detected due to the different modelling of nucleation and coagulation processes characterized by a higher activation temperature.

Distributions of soot volume fraction f_v for the three soot models are reported in fig. 6.8 for 1.5 ms and 4 ms respectively, compared with the experimental ensemble-averaged optical thickness KL or time-averaged over quasi-steady period f_v distributions. As it can be seen from images, the visible region of interest (ROI) in the experimental detections extends from 15.2 mm to 67.2 mm. In [69], it is pointed out that model comparisons should be made only within this ROI. The quasi-steady period is assumed between 2.5 ms and 6 ms (EOI), but this time interval refers to the given experimental ROI and this does not mean that the flame reaches its stable length already at 2.5 ms. This is the time at which the transient head vortex of the jet is completely out of sight. If computed vapour penetration is compared with the experimental one, a very good match is observed. In these reference conditions, stoichiometric mixture fraction contour reaches a stable axial position at about 4-4.5 ms and it can be assumed that the experimental flame stabilizes not much earlier.

The time evolution of f_v for the three models is in agreement with the time sequences of KL acquired in different works [47, 49, 69]: during the initial transient period, the higher values of f_v are concentrated in the head vortex where there is still a rather rich mixture. Then, as the jet extends and tends to the quasi-

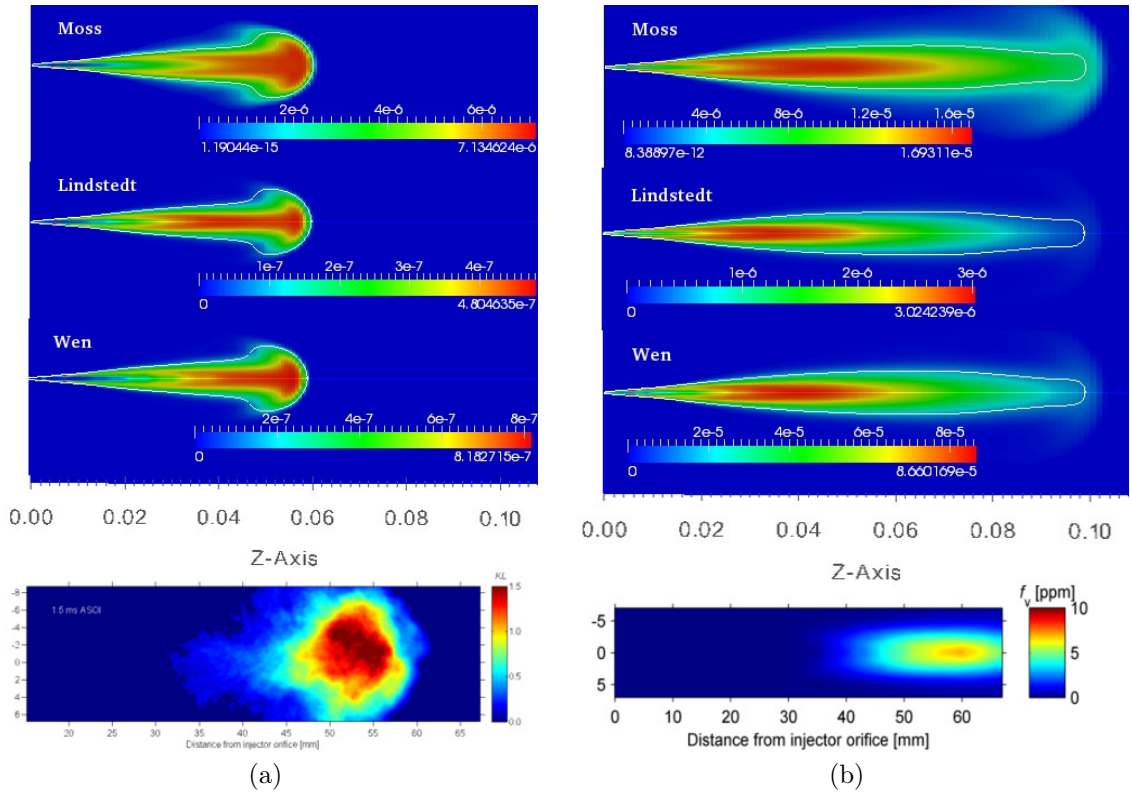

(a) (b)

Figure 6.8. Computed f_v for the reference case at 1.5 ms (a) and 4 ms (b) with model of Moss (top), Lindstedt (middle) and Wen (bottom). The white line points the stoichiometric mixture fraction contour. The frames at the bottom respectively show the KL profiles at 1.5 ms (a) and the measured f_v at 4 ms (b) reproduced from [69].

steady condition, more air is incorporated and the axial gradient of mixture fraction diminishes. In this way, the rich zone with abundance of C_2H_2, where soot can grow in mass, tends to be located in the middle of the jet. The axial position in which there is the maximum of KL and f_v is the point where soot mass growth and oxidation are balanced. In terms of this position, there is a fairly good agreement with the experimental measurements, especially for Moss which tends to have a distribution less overlapped to that of C_2H_2 unlike Lindstedt and Wen. There can be two reasons for this behaviour. The first one is that the source term of surface growth for the model of Moss is directly proportional to the number of particles, which has a peak further downstream than that of the acetylene (fig.6.7). The second is the higher activation temperature for soot mass growth in Moss model. Upstream of the peak location, the f_v rise and thus that of total soot mass across the fuel jet cross section indicate the dominance of soot formation over soot oxidation. The overall rate of soot formation, however, must decrease with increasing axial distance as the fuel and soot are consumed by combustion. Downstream of the peak, the amount of soot decreases as soot oxidation begins to dominate over soot formation as the flame length is approached [37]. In general, the largest discrepancy between computed and experimental soot distributions is related to the lack of lift-off for the computed flame. This determines a soot on-set axial location practically attached to the nozzle, while the mean experimental one is equal to 33.1 mm, with a larger zone in which

soot can nucleate and adds mass. The reason for the distinct separation between the location of LOL and that of first soot formation is because it takes a finite amount of time for soot precursors and then soot to form downstream of the region of first heat release [40]. In the performed simulations this aspect is less evident due to a soot kinetic modeling greatly simplified which leads to have a certain overlap with the areas of a high concentration of C_2H_2 and high temperature.

Distributions of f_v for the three models over time are quite similar but Wen model shows a more delayed soot on-set time. Moreover, maximum values for Wen are lower up to about 2.5 ms and then increase fast above the maximum values of both the other models. Lindstedt model leads to values of about an order of magnitude lower than Moss. Compared to the experimental values, Moss and especially Wen overestimate the maximum value of f_v while Lindstedt underestimates it. This behaviour can be due quantitatively to the lack of setting constant values and qualitatively to the difference in modeling soot nucleation but mostly to the difference dependency of soot mass growth, the most important process in determining the total soot mass produced. The dependence on the square root of soot surface for Lindstedt model slows the addition of mass, trying to take into account the surface ageing of particle as explained in chapters 1 and 3.

It is observed that, in general, region with the highest concentration of soot particles does not coincide with the one characterized by the highest values of f_v and it is possible to see a non-zero number of particles in fuel lean region where negligible soot mass is present. This is due to the numerical formulation of soot oxidation in the two-equation models used: oxidation decreases particle mass but not the number.

Finally, results for the total soot mass yield for the entire vessel are reported as a function of time along with the experimental one [69] in fig. 6.9.

It is worth to highlight that the aim of this work at this point is to evaluate the soot time trend. The prediction in terms of amount of soot might be improved by a more accurate flame model and by properly setting semi-empirical constants.

Great attention must be focused on the fact that experimental soot mass reported is obtained processing high-speed KL images such as those above. Therefore they take into account only soot mass present in the ROI specified for experimental detections. The experimental trend of total soot mass shows an initial peak with a subsequent stabilization. Such peak, therefore, seems to be due to the exit from the field of view of the head vortex of the jet, which it is characterized by a higher soot concentration, and only to minor part to the effect of its rapid partial oxidation within the field of experimental detection. Then, the stabilization of soot is due to the quasi-steady conditions which are established in the jet after the passage of the head vortex. Even Pickett, in his work [6], highlights this behaviour of soot. This mass of soot is actually only partial and it is reasonable to think that the real total mass in the flame grows even after the head has overstepped the right boundary of the ROI. The difference between the actual mass and the one experimentally detected is greater the more the environmental conditions lead to a longer flame length. However, it could be correct to expect a peak and a subsequent stabilization delayed in time, related to the achievement of the stationary flame length and to the oxidation of soot present in the head vortex. Since the total soot mass computed in this work are related to the whole flame, their quantitative comparison with the

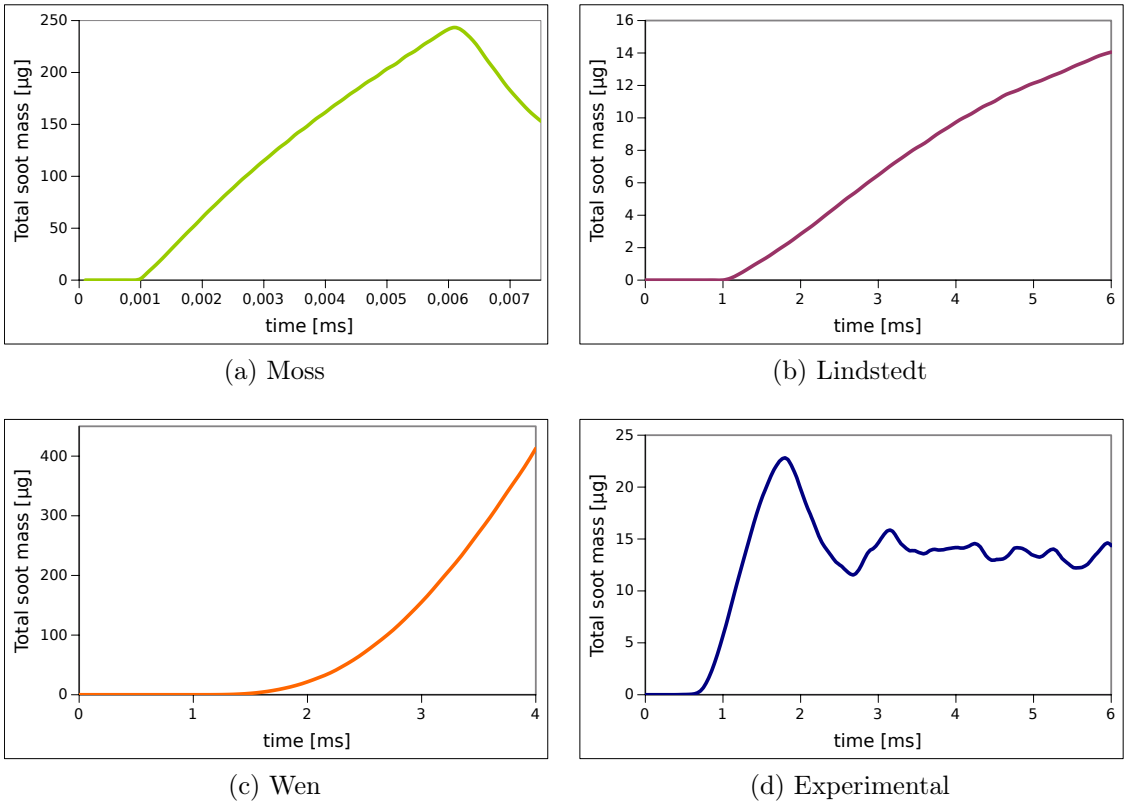

(a) Moss (b) Lindstedt

(c) Wen (d) Experimental

Figure 6.9. Total soot mass computed with the three soot models at reference conditions. Experimental trends is reported in (d) for comparison.

experimental ones is not strictly correct, but, as pointed out several times, here it is mainly interested in assessing their relative variations when ambient conditions are changed.

None of the three models can reproduce the stabilization of soot, even if delayed in time, though Moss and Lindstedt, after a rapid initial growth, show a decrease in the derivative of total soot mass. Wen model, on the other hand, shows a wrong trend, with a continuous increase in the rate of soot formation. The reasons for the failure of expected soot stabilization can be different. The absence of flame lift-off produces a large rich area, in which soot can grow in mass without being oxidized. Certainly the simplified semi-empirical modelling of soot processes greatly contributes: the consumption of chemical species associated to soot formation (C_2H_2) and the slowing down of these processes for the approaching of the thermodynamic equilibrium are not taken into account. Moreover, the soot models do not consider (Moss and Wen), or at least do it in a very simplified way (Lindstedt), the surface ageing of particles. Another possible factor could be the modelling of the spray: it seems to give values for mixture fraction rather high (no experimental data are available but maximum values of about 0.3 – 0.4 are considered reasonable), especially in the upstream part of the jet. This can result in higher values of C_2H_2 and soot reported by the flamelet domain to the physical one.

In [69] soot on-set time is defined as the time ASOI at which the total soot mass exceeds the value of 0.5 µg. In tab. 6.8 the computed values compared with the

experimental one are reported.

Table 6.8. Soot on-set times calculated with the models of Moss, Lindstedt and Wen at reference conditions.

	Experimental	Moss	Lindstedt	Wen
Soot on-set time [ms]	0.73	1	1.3	1.6

At the end of injection, the total mass of soot in the vessel is gradually oxidized. The computed soot is not fully oxidized in the same time because the absolute values are higher and more time is required by oxidation of all soot mass generated. Furthermore, this could also be due to the fact that the oxidation mechanism is related only to OH and, as noted in chapter 1, oxygen plays an important role in the oxidation of soot in the leaner conditions that are created when injection finishes.

Taking into account the fact that the ignition delay is overestimated of about 0.5 ms, it may be considered in an approximate way that Lindstedt model provides the best result. The higher delay in the soot on-set time for Wen model and its different trend compared to the other two soot model, could be explained by the lower values of the constant for nucleation and mass growth source terms and the dependence of latter from soot surface and not from square root of surface as for Lindstedt. This causes a mass of soot produced initially lower but which then grows in a much quicker way. Looking at soot trend completely different from the experimental one and from that of the other two models, the following analysis have been performed with the models of Moss and Lindstedt.

6.2.2 Validation of soot models: Moss

Influence of ambient temperature

Experimental measurement of LOL and ignition delay for the analysed cases, along with the computed ignition delay, are summarized in tab. 6.9.

Table 6.9. Measured LOL and ignition delay and computed ID with single RIF for different ambient temperatures.

	Measured LOL [mm]	Measured ID [ms]	Computed ID [ms]
850 K	20.6	0.59	1.2
900 K	16.1	0.4	0.9
1000 K	11.5	0.32	0.6

As can be observed from heat release trend reproduced in fig. 6.10 ignition delays are still overestimated but error decreases with increasing initial temperature, and this is likely due to the higher chemical reactivity that counterbalances the effect of elevated scalar dissipation rate.

Flame structure is almost similar for the three cases. Increasing ambient temperature causes an increment of maximum flame temperature and C_2H_2 and OH mass

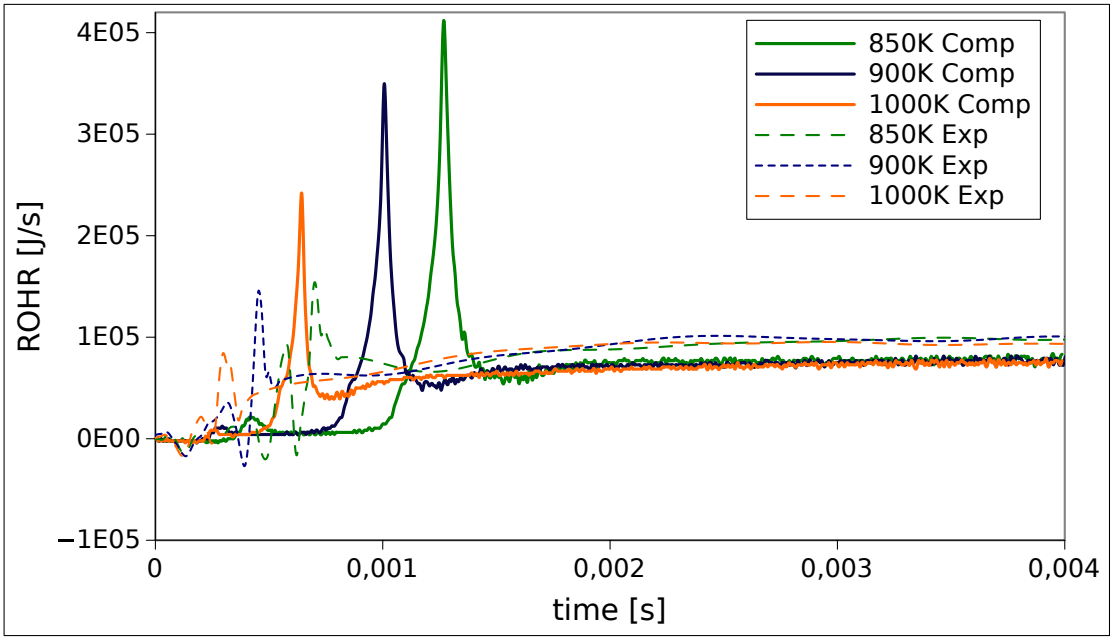

Figure 6.10. ROHR computed with single flamelet combustion model (full line) and measured (dashed line) for 850K, 900K and 1000K

fraction as shown in fig. 6.11. Due to the inability of the single flamelet to predict the lift-off length where premixed combustion occurs, it is impossible to provide the increment of the equivalence ratio but, because of the higher temperatures, accelerated chemical kinetics leads to higher values of C_2H_2.

As it can be seen in fig. 6.12, with increasing ambient temperature, soot volume fraction and particle number density increase, in agreement with experimental results. This is due both to the direct effect of temperature on the soot nucleation, mass growth and oxidation kinetics but also to indirect effect of increment of species involved in soot processes. With a no-lifted flame, the variation in the position of sooting region cannot be easily caught, with the peak of f_v located approximately in the same region for all three cases.

With regard to total soot mass, in fig. 6.13 computed normalised trends versus time are compared to experimental ones and several results are summarize in tab. 6.10.

Table 6.10. Soot data for different ambient temperatures computed with Moss and single RIF models. Normalized quasi-steady soot values are reported in brackets.

	Exp. soot on-set time [ms]	Comp. soot on-set time [ms]	Exp. quasi-steady soot value [µg]	Comp. quasi-steady soot value [µg]
850 K	1.14	1.3	2(0.143)	142 (0.86)
900 K	0.73	1	14 (1)	165 (1)
1000 K	0.47	0.65	42 (3)	197 (1.20)

Trend of variation with ambient temperature is correct: total soot mass increases when ambient temperature is higher. As can be observed by normalised values

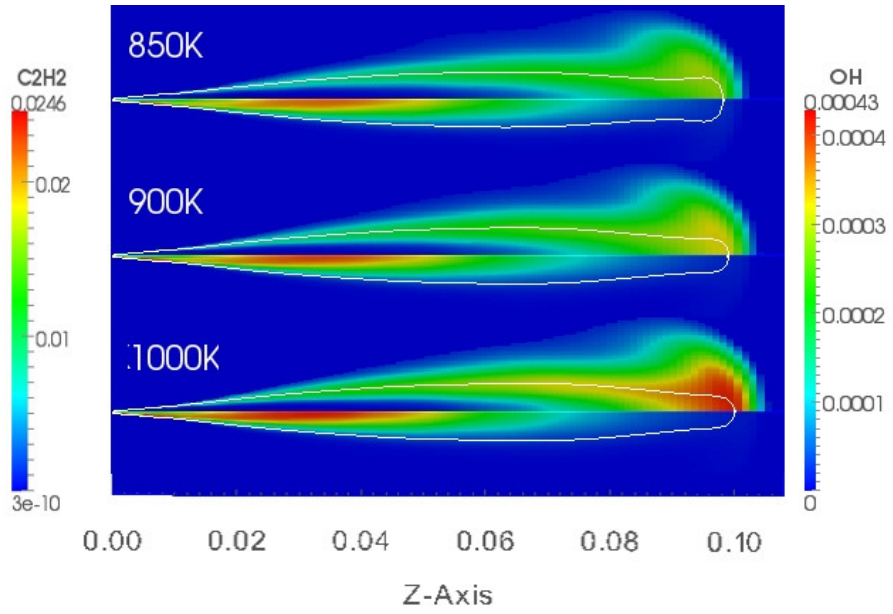

Figure 6.11. Comparison of C_2H_2 and OH fields for different ambient temperatures. The C_2H_2 and OH fields are respectively shown in the bottom and in the top half of each frame.

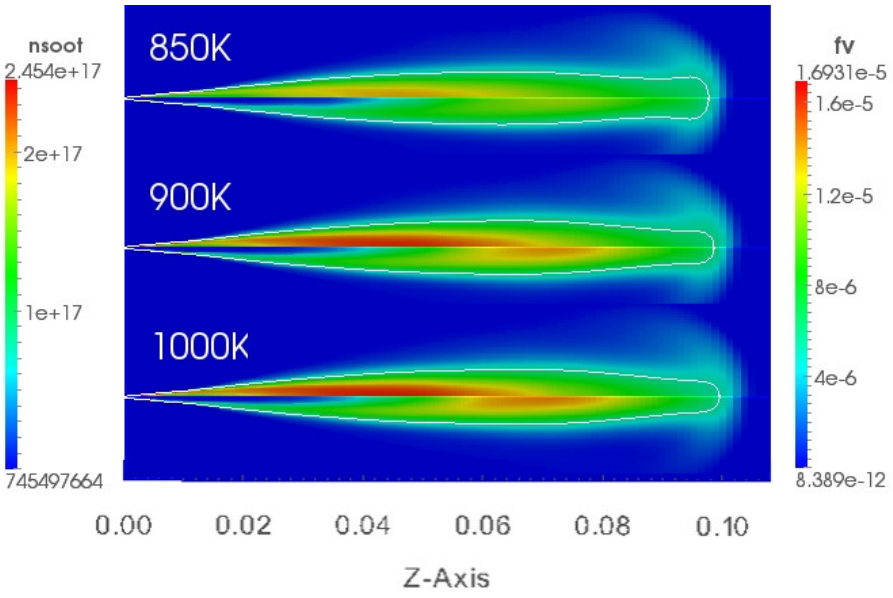

Figure 6.12. Comparison of soot volume fraction and particle number density fields for different ambient temperatures. The f_v and n_{soot} fields are respectively shown in the top and in the bottom half of each frame.

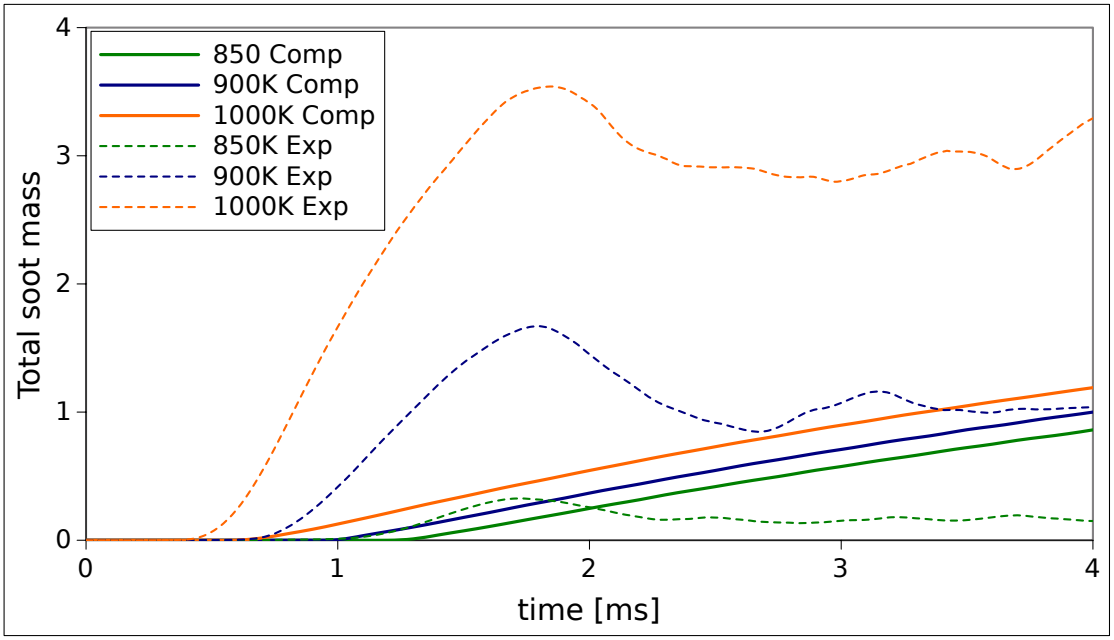

Figure 6.13. Comparison of normalised total soot mass computed (full lines) with the model of Moss with the experimental values (dashed lines) taken from [69] for different ambient temperatures.

to that at 4 ms in reference conditions, the normalised changes are less than the experimental case and this is primarily due to the lack of lift-off and also to the simplicity of the model of soot. Indeed, the lower magnitude of changes of computed values indicates that the simplified modelling of the influence of temperature on the different soot processes can not fully reproduce the strong effect that it has on the actual soot kinetics.

Influence of oxygen concentration

Influence of three different initial oxygen concentrations are investigated. In tab. 6.11 the main features of three cases are indicated.

Table 6.11. Measured LOL and ID and computed with single RIF ignition delay for different oxygen concentrations.

	Measured LOL [mm]	Measured ID [ms]	Computed ID [ms]	Z_{stoich}	Computed T_{max} [K]
13%	20.4	0.47	1.3	0.0393	1990
15%	16.1	0.4	0.9	0.045	2110
21%	9.9	0.28	0.5	0.0614	2500

Trend for ignition delay is correct and analogous consideration made for cases with variation of ambient temperature can be done here: increasing initial O_2 concentration, the difference between experimental ignition delay and computed one, reduces. In this case, the higher reactivity is caused by the higher oxygen concentration.

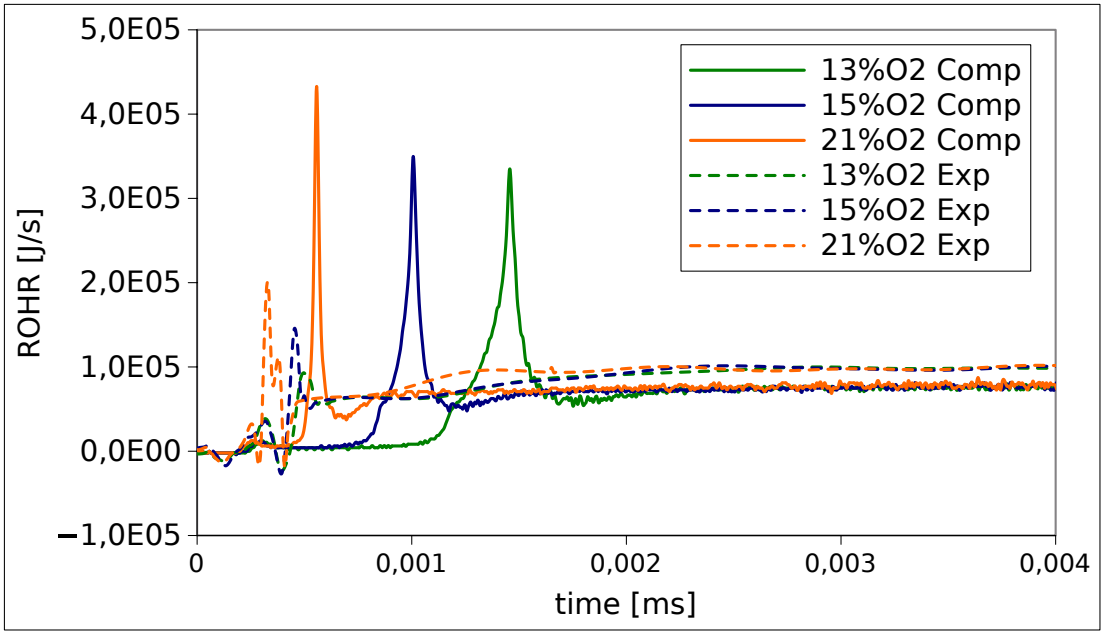

Figure 6.14. ROHR computed with single flamelet combustion model (full line) and measured (dashed line) for 13%, 15% and 21% oxygen molar fractions.

As it is possible to see from fig. 6.14, indeed, with less oxygen, peak of heat release rate diminishes but the duration of premixed burn increases.

Unlike before, structure of the flame varies significantly. In agreement with experimental results, flame length reduces when the amount of oxygen increases, because for a given mass of oxidizer, a greater mass of air should be entrained into the jet. In the same way, the increase of the oxygen concentration makes the stoichiometric mixture fraction Z_{stoich} larger and, hence, the stoichiometric region is smaller. Thus, Z_{stoich} iso-contour for the case with 21% O_2 reaches a stable position at about 2.8 ms, while the other two flame at 4 ms are not yet stabilized, even if Z_{stoich} profile for 15% O_2 has a more elongated shape, compared to that with 13% O_2, indicating that the stabilization of the flame is closer in time. As reported in tab. 6.11, maximum temperature increases with oxygen concentration.

Fig. 6.15 shows distributions of C_2H_2 and OH at 4 ms. Thanks to the different conditions in terms of reactivity and temperature, mass fractions of acetylene and especially OH increase raising oxygen concentration. On the other hand, it progressively reduces the extension of the region in which acetylene is present, that is the richer zone where soot is assumed to be formed according to the conceptual model.

Soot volume fraction and particle number density fields are displayed in fig. 6.16. In agreement with experimental detections, peak for both quantities reduces with decreasing oxygen concentration due to the slower kinetics of soot nucleation and mass growth, related to lower temperatures and amount of C_2H_2. At the same time, however, soot is distributed over increasingly large areas, with more residence time for soot to nucleate and then to grow in mass, because, as described in chapt. 1, thanks to lower temperature and lower rate of oxygen entrainment into the jet, soot formation rate exceeds oxidation rate for greater distances from injector.

This compromise allows to explain the non-linear trend observed for the total

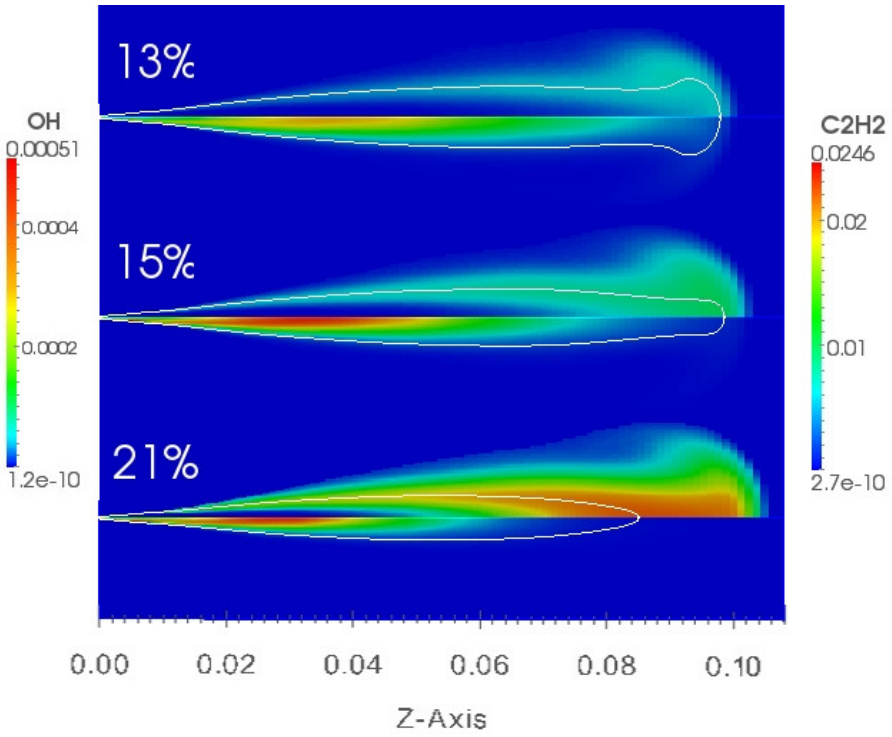

Figure 6.15. Comparison of C_2H_2 and OH fields for different oxygen concentrations. The C_2H_2 and OH fields are respectively shown in the bottom and in the top half of each frame.

soot mass produced varying the initial concentration of oxygen as shown in fig. 6.17, in which computed normalised results are plotted along with the experimental ones, and in tab. 6.12.

Table 6.12. Soot data for different oxygen concentrations computed with Moss and single RIF models. Normalized quasi-steady soot values are reported in brackets.

	Exp. soot on-set time [ms]	Comp. soot on-set time [ms]	Exp. quasi-steady soot value [µg]	Comp. quasi-steady soot value [µg]
13%	0.97	1.45	10 (0.71)	107 (0.65)
15%	0.73	1	14 (1)	165 (1)
21%	0.36	0.55	11 (0.786)	117 (0.71)

It is very interesting to observe that normalised values are closer to the experimental ones compared to case with variation of temperature. This is likely due to the fact that, as described in chap. 1 and proved by several works [17, 38–40], varying ambient oxygen concentration, LOL changes but the equivalence ratio in this position remains approximately the same. Variation in LOL does not affect considerably the variation of amount of soot yield but only its axial position. Therefore, the inability of single RIF to reproduce the lift-off with only one flamelet is less important in these cases.

An other important observation is that trend of total soot mass for case with 21% O2 shows, after the first instants of soot formation, a strong reduction in the

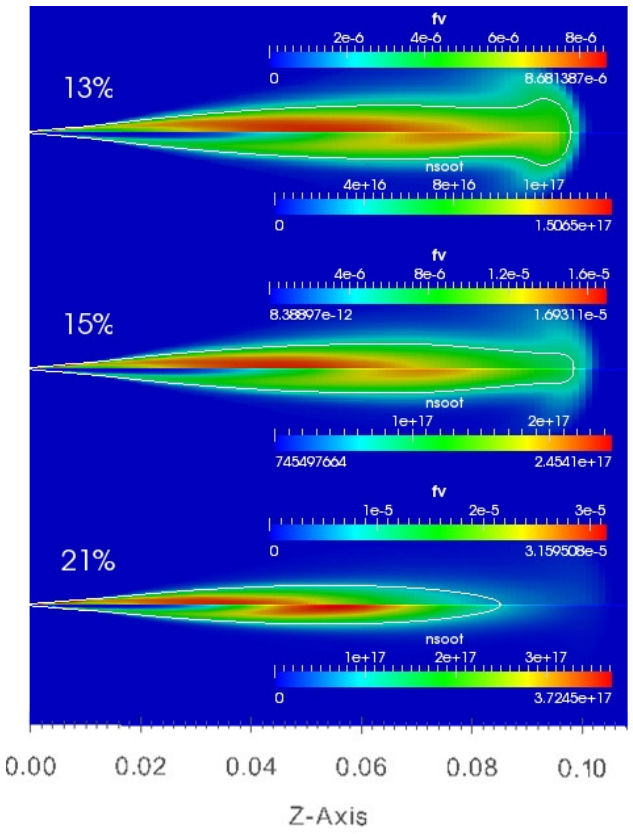

Figure 6.16. Comparison of soot volume fraction and particle number density fields for different oxygen concentrations. The f_v and n_{soot} fields are respectively shown in the top and in the bottom half of each frame.

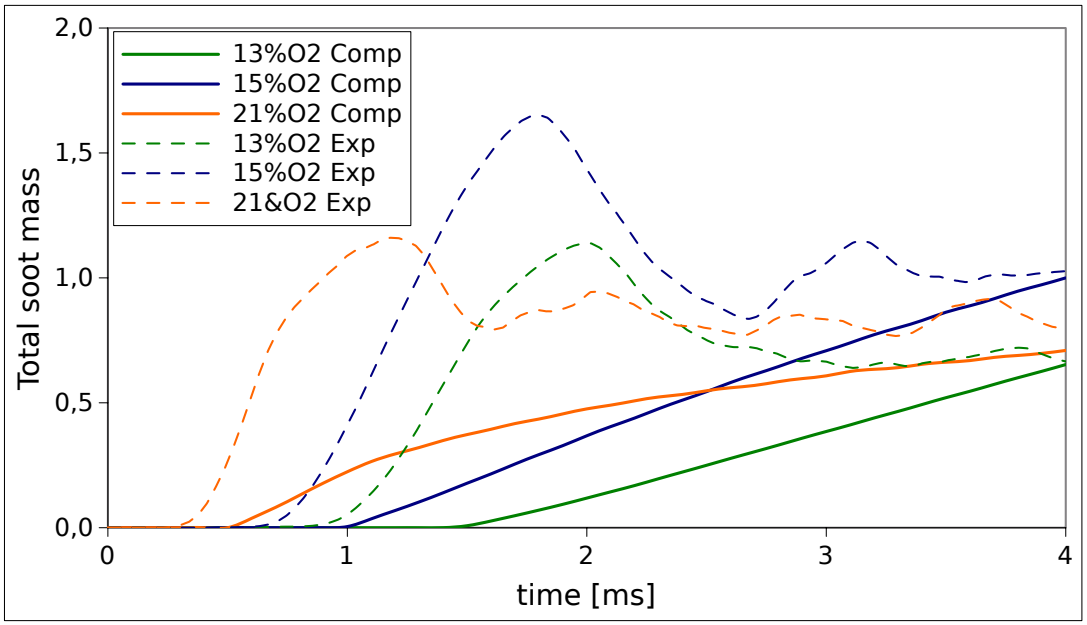

Figure 6.17. Comparison of normalised total soot mass computed (full lines) with the model of Moss with the experimental values (dashed lines) taken from [69] for different oxygen concentrations.

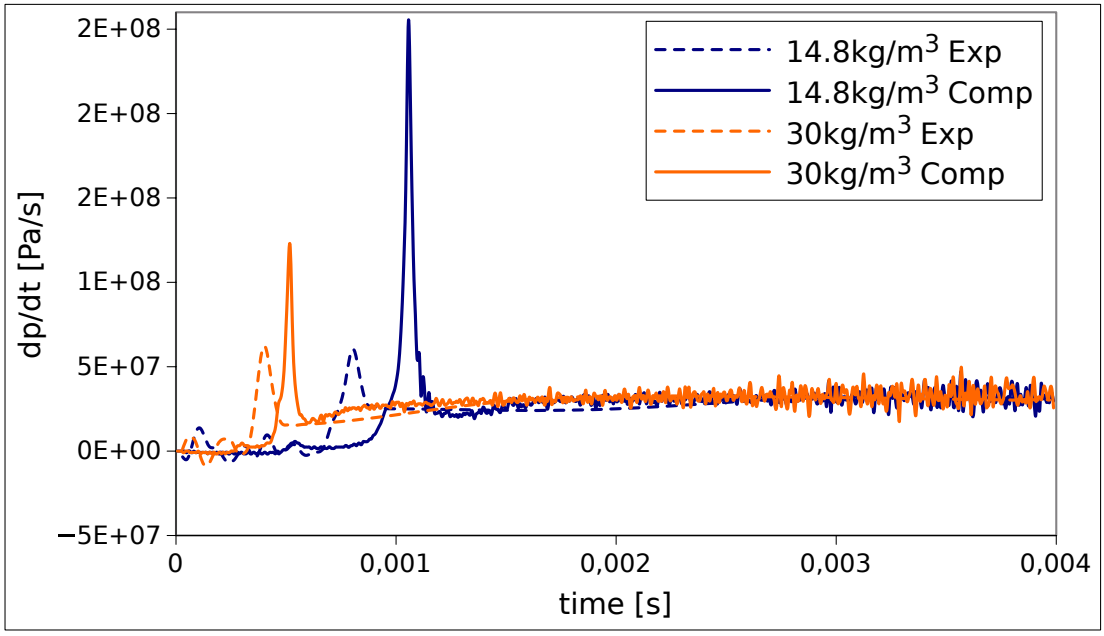

Figure 6.18. Pressure derivative computed with single flamelet combustion model (full line) and measured (dashed line) for 14.8 kg/m^3 and 30 kg/m^3.

derivative versus time, approaching almost to a stabilization of soot. It is believed that this is due to the attainment of the quasi-steady condition of the flame in less time with a confinement of rich zones of soot growth into smaller regions.

Influence of ambient density

To assess ambient gas density effects on soot, conditions of spray-H are simulated. Only two different conditions are considered and their main features are summed up in tab. 6.13.

Table 6.13. Measured LOL and ID and computed with single RIF ignition delay for different ambient densities.

	Measured LOL [mm]	Measured ID [ms]	Computed ID [ms]
14.8 kg/m^3	23.4	0.73	1.0
30 kg/m^3	11.9	0.38	0.5

Looking at the pressure derivative profiles in fig. 6.18 (no ROHR data are available for spray-H), the increase of the ignition delay for lower density can be observed, in agreement with theory and experimental results, but also of the overestimation of it, as for cases with temperature and oxygen variations. With the increase of ambient density, LOL decreases but at the same time the air entrainment builds up. This produces an intense reduction of flame length, as can be seen in fig. 6.19 from the profile of stoichiometric mixture fraction at 4 ms and also of its radial extension.

In this case, the inability to provide the lift-off with one flamelet causes the presence of less rich zones upstream in the jet, in contrast to experimental observations,

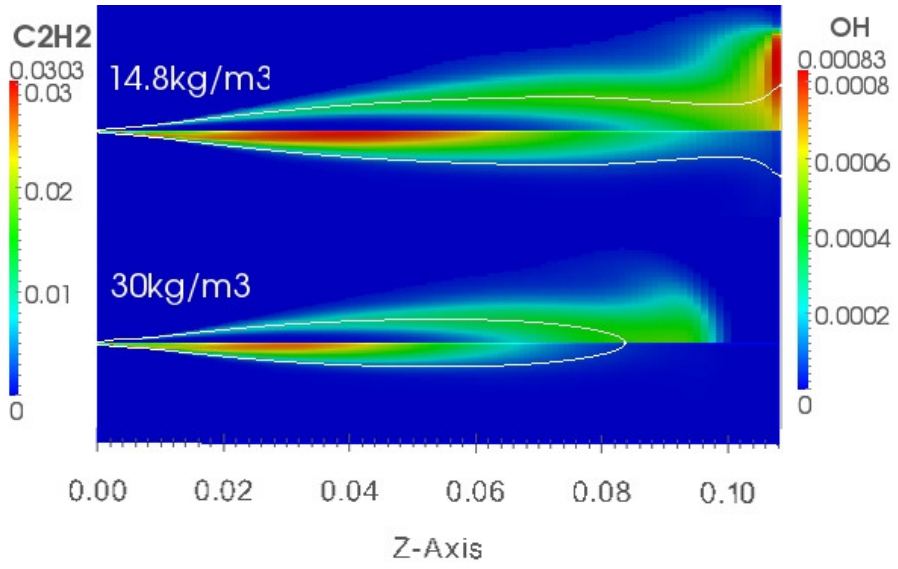

Figure 6.19. Comparison of C_2H_2 and OH fields for different ambient densities. The C_2H_2 and OH fields are respectively shown in the bottom and in the top half of each frame.

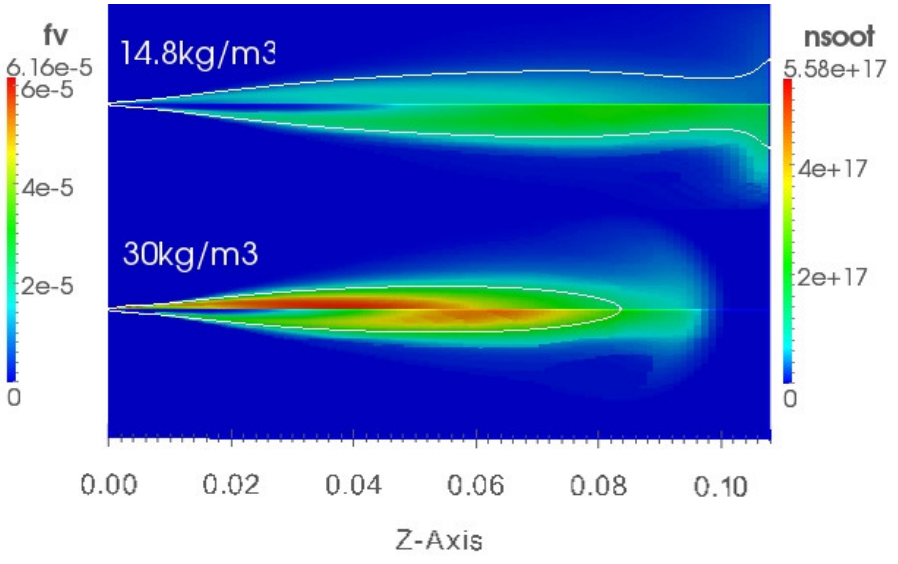

Figure 6.20. Comparison of soot volume fraction and particle number density fields for different ambient densities. The f_v and n_{soot} fields are respectively shown in the top and in the bottom half of each frame.

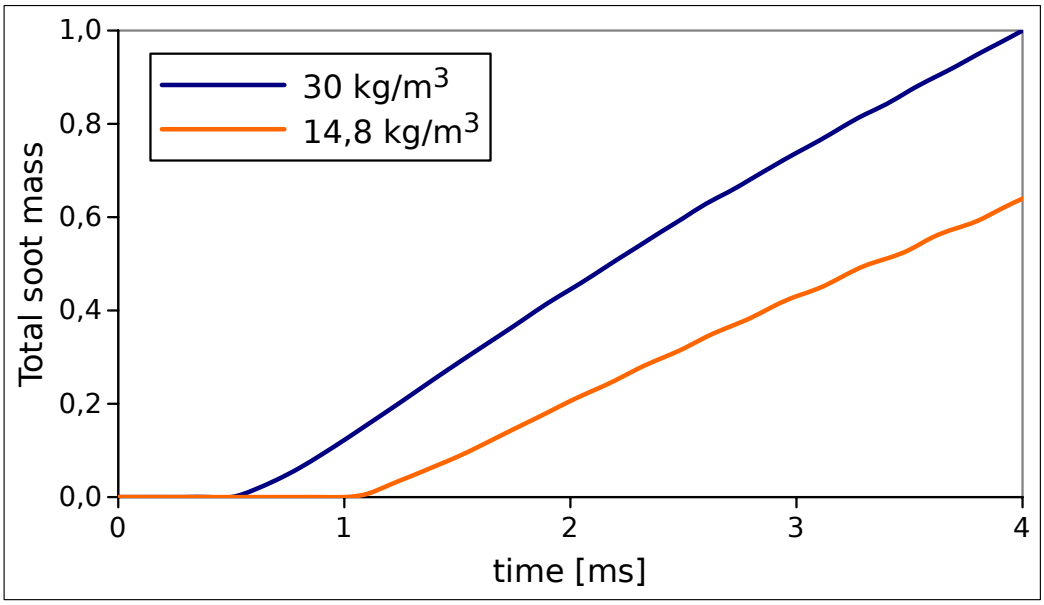

Figure 6.21. Normalised total soot mass computed with the model of Moss and single RIF model for different ambient densities.

with a minor peak of C_2H_2 mass fraction. Despite this, the results related to the soot match with the experimental data, at least the trend. Fig. 6.20, indeed, shows distributions of f_v and particle number density at 4 ms.

Peaks of the two variables considered are greater for the case with higher density and this can be explained by the fact that the molar concentration of acetylene and not the mass fraction appears in source terms of soot nucleation and surface growth. However, as already pointed out in chapt. 1, an increase of any chemical species concentrations, and not only for soot, is expected because of the higher density. Pickett, on the other hand, in [6] has shown that there is an increase in soot produced much greater to that expected from the simple increase in density and due to richer premixed combustion associated with lower LOL, respect to the conceptual model of Dec [7]. Computed values of f_v for the two different densities are less distant than in the experimental case, in which peaks differ by an order of magnitude, showing that model tends to capture only partially this further increase in soot concentration due to the richer conditions and not simply to the increment of reactants quantity per unit volume. As for the experimental data, even computed distributions show a shift of sooting regions downstream in the jet with decreasing density, due to the lower reactivity associated to the lower molecular collision frequency and to greater distances from the injector nozzle required to entrain the same amount of air into the jet.

Finally, the total soot mass is reported in fig 6.21. However, no experimental data are available in terms of total soot mass and comparisons cannot be made. The absolute values are certainly largely overestimated, but the trend is correct. The values are the highest reported so far and this is likely due the higher ambient temperature and to the different conditions of the spray-H.

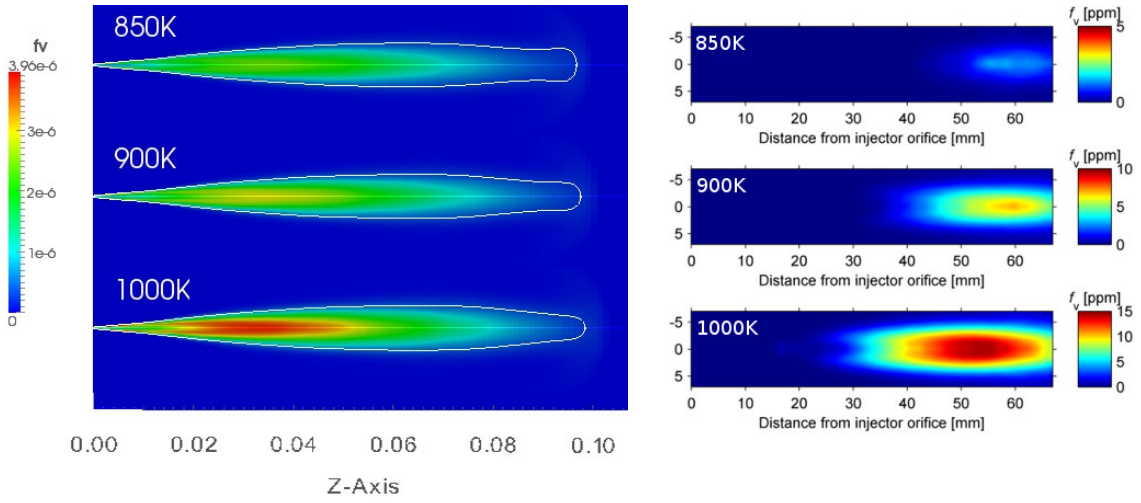

Figure 6.22. Soot volume fraction computed (a) with the model of Lindstedt and measured (b) by [69] for different ambient temperatures.

6.2.3 Validation of soot models: Lindstedt

Influence of ambient temperature

As it was observed in section 6.2.1, Lindstedt tends to predict an amount of soot closer to the experimental values in reference conditions.

Distributions of computed f_v in physical domain at different ambient temperatures compared with the experimental ones are reported in fig. 6.22.

Moreover, in fig. 6.23 f_v axial profiles for the models of Moss and of Lindstedt and the experimental values are shown. Also varying ambient temperature the best agreement with the quantitative data remains true. Lindstedt model seems to be less able to vary the amount of soot produced in terms of absolute values but this could be due to the fact that these absolute values are smaller than Moss. Looking at f_v normalised profiles, which are referred to the peak value at reference conditions, it is possible to observe that variations are rather similar. Both models provide a small shift of the peak f_v upstream as the temperature increases. Lindstedt, as discussed in section 6.2.1, determines the peak closer to the injector, because sooting region are more overlapped to those with the greatest concentration of C_2H_2.

Absolute and normalised total soot mass are reported in fig. 6.24. Normalized trends show that Lindstedt model captures slightly better the variation of the total soot mass than Moss as the temperature changes.

Influence of oxygen concentration

The f_v axial profile computed with the models of Lindstedt and Moss are reported in fig. 6.25. With Lindstedt model the quantitative agreement with experimental values is better and soot is distributed over smaller region. Both models provide a correct shift of f_v peak downstream from the injector with decreasing oxygen concentration and above all its reduction in value. It is interesting observe that at a

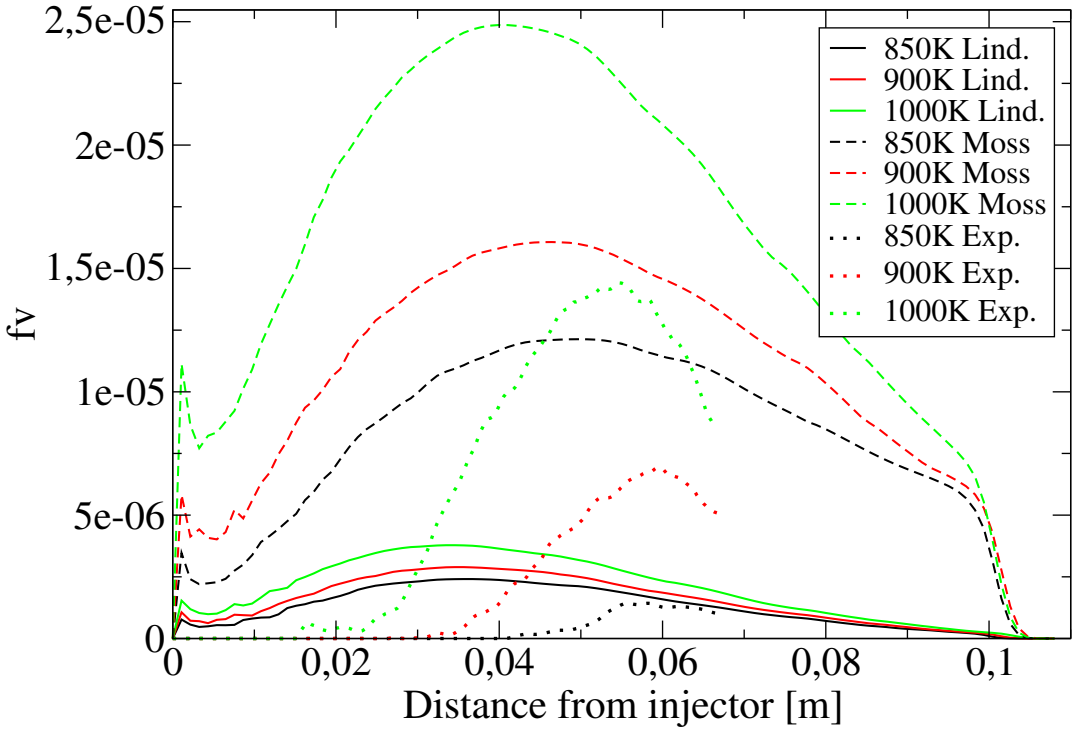

(a) Absolute

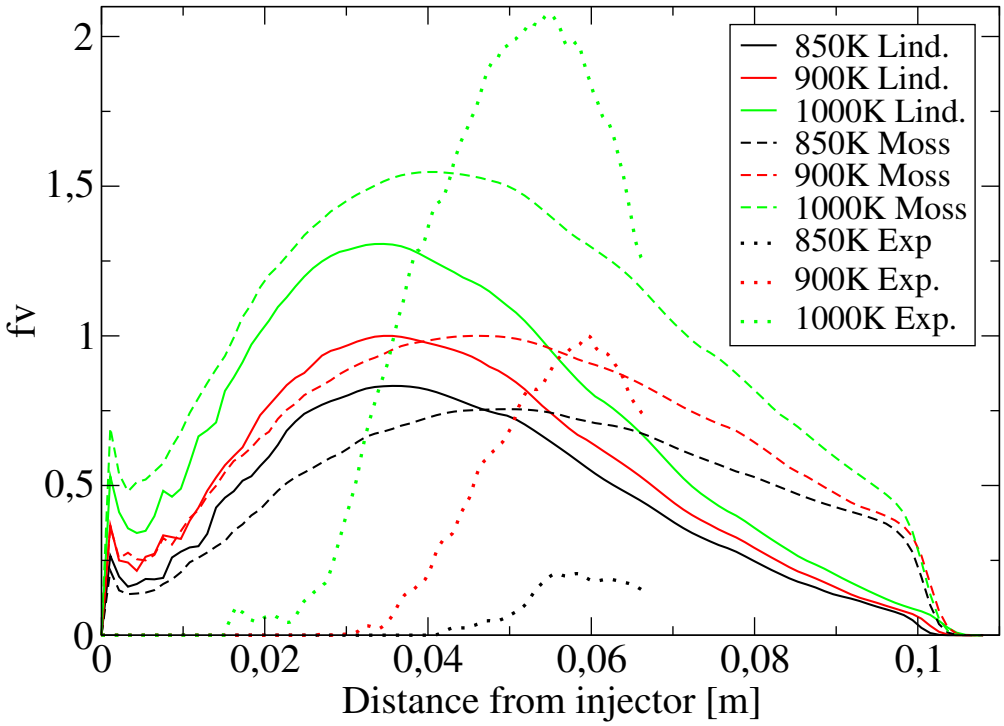

(b) Normalized

Figure 6.23. f_v axial profiles computed with the models of Moss (dashed lines) and Lindstedt (full line) and single RIF model for different ambient temperatures. Measured profiles are reported in dot lines.

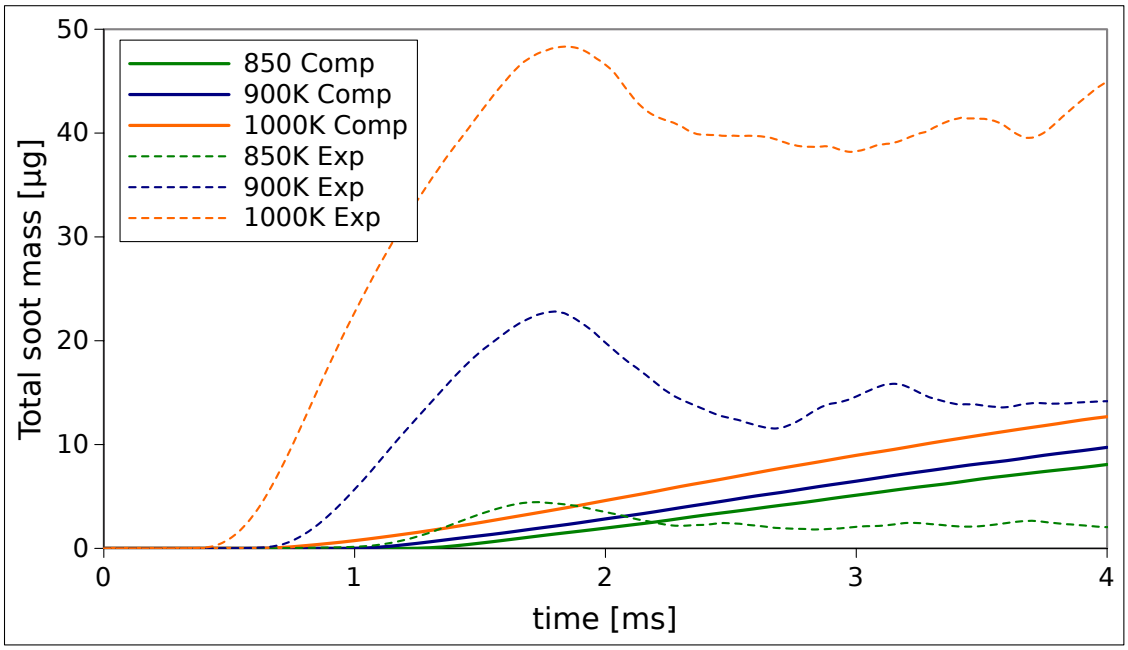

(a) Absolute

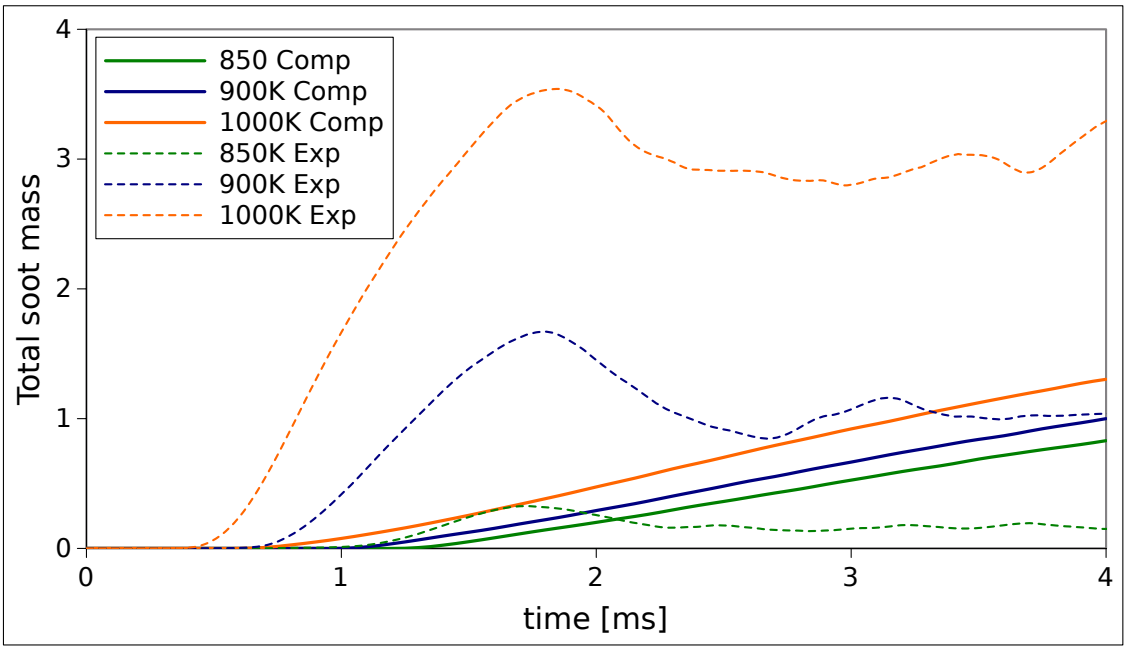

(b) Normalized

Figure 6.24. Comparison of total soot mass computed (full lines) with the model of Lindstedt with the experimental values (dashed lines) taken from [69] for different ambient temperatures.

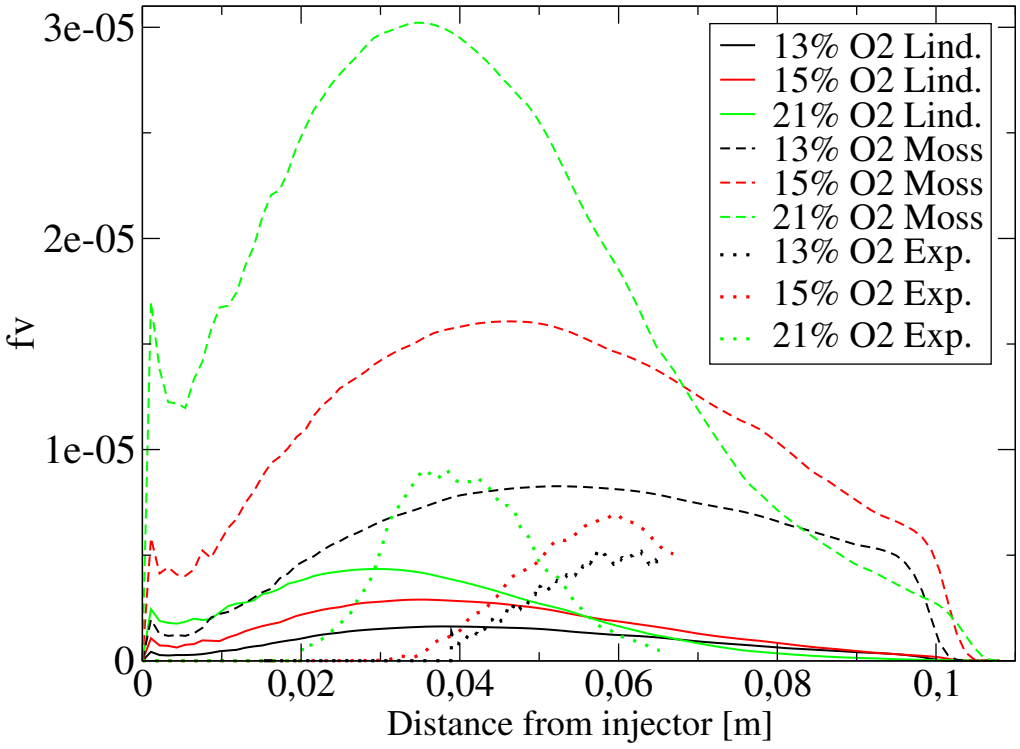

(a) Absolute

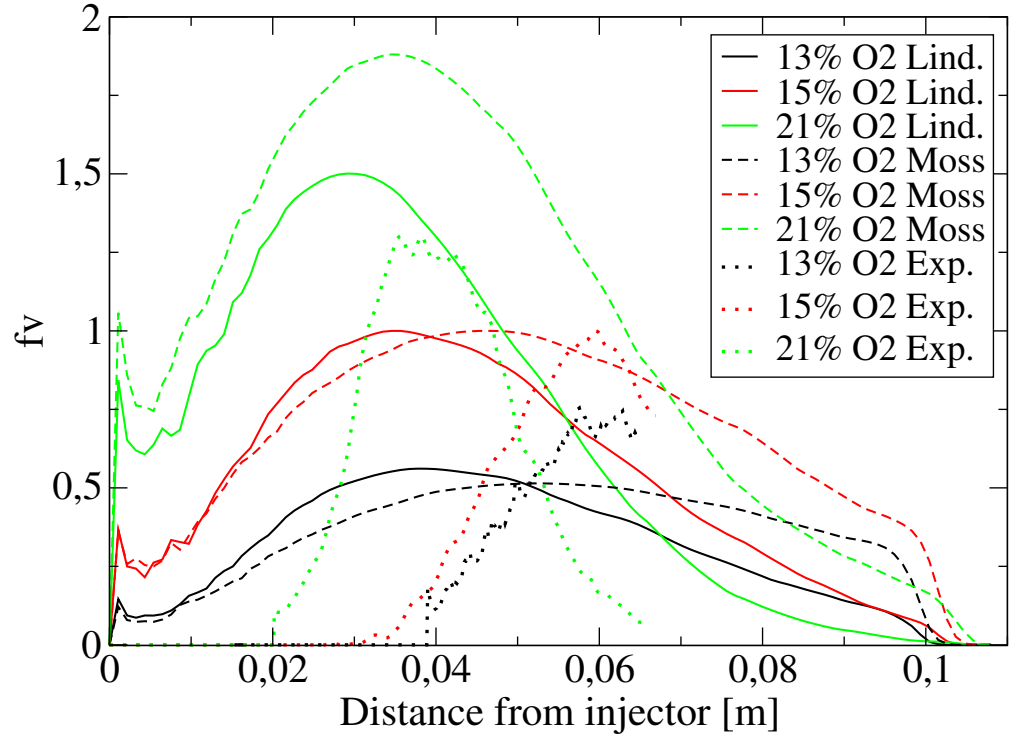

(b) Normalized

Figure 6.25. f_v axial profiles computed with the models of Moss (dashed lines) and Lindstedt (full line) for different oxygen concentrations. Measured profiles are reported in dot lines.

certain axial location, f_v profile for the case with 21% O_2 drops to lower values than to those of the other two cases because flame length is shorter and soot oxidation begins further upstream. However, for Moss model at a certain point, this profile returns above whereas this does not happen with Lindstedt. This is believed to be due to the oxygen oxidation mechanism which becomes increasingly important approaching the stoichiometric contour of the flame and especially just outside of it. Looking at normalised quantities, variations are similar with two models, even if Moss tends to provide slightly major variations.

In terms of total soot mass reproduced in fig. 6.26, Lindstedt provides a correct trend with varying ambient oxygen concentration as was observed for Moss. The normalised values are in discrete agreement with the experimental counterparts, even if there is an overestimation of the reduction for the condition with 21% O_2. It is very interesting to note that the latter case is the only one analysed so far that actually reaches a stabilization of the soot. Probably, in addition to the considerations provided for the model of Moss, this further improvement is due to the addition of oxygen as oxidizing species of soot and to the different modelling of soot mass growth. The abundance of oxygen in this case permits to achieve a balance between formation and oxidation that in the other cases is only approached.

Influence of ambient density

In terms of f_v, Lindstedt model tends to give better results than Moss both in quantitative terms and as regards the distribution in physical domain.

In fact, as it can possible to see from fig. 6.27, especially for the case with ambient density of 30 kg/m^3, computed distributions match quite well with the experimental ones. For case with density of 14.8 kg/m^3, however, the reduction of f_v peak value is less accentuated than the experimental comparison. Properly, also the Lindstedt model predicts a decrease of the extension of the region of soot and a shift of the peak towards the injector with the increase of density.

Fig. 6.28 shows the f_v axial distributions for the two models normalised with the respective peak value at 30 kg/m^3. Trends are similar, but Lindstedt model predicts a minor normalised reduction with decreasing density and a position of peak closer to the injector, probably due in part also to oxidation by oxygen. More interesting is to observe the trends of the total soot mass reported in fig. 6.29.

Comparing the total soot mass trends obtained with the model of Lindstedt reported in fig. 6.29 and with the model of Moss (fig. 6.21) the following observations can be done. The model of Moss shows a quantity of soot, for the case with higher density, constantly greater than that at lower density and the trends are increasingly spaced apart as time passes. The two trends for the Lindstedt model, instead, at about 4 ms intersect and the total soot mass becomes, incorrectly, larger for the case with lower density. This is believed to be probably due to the different modelling of the growth surface that might be less sensitive to variations in the concentration of acetylene and to the oxidation by oxygen, which, given the structure of the flame with higher densities, has a greater influence in this case. This negative result, however, must not be completely attributed to the soot model, but must also be viewed in relation to the shortcomings in the modelling of the flame highlighted several times.

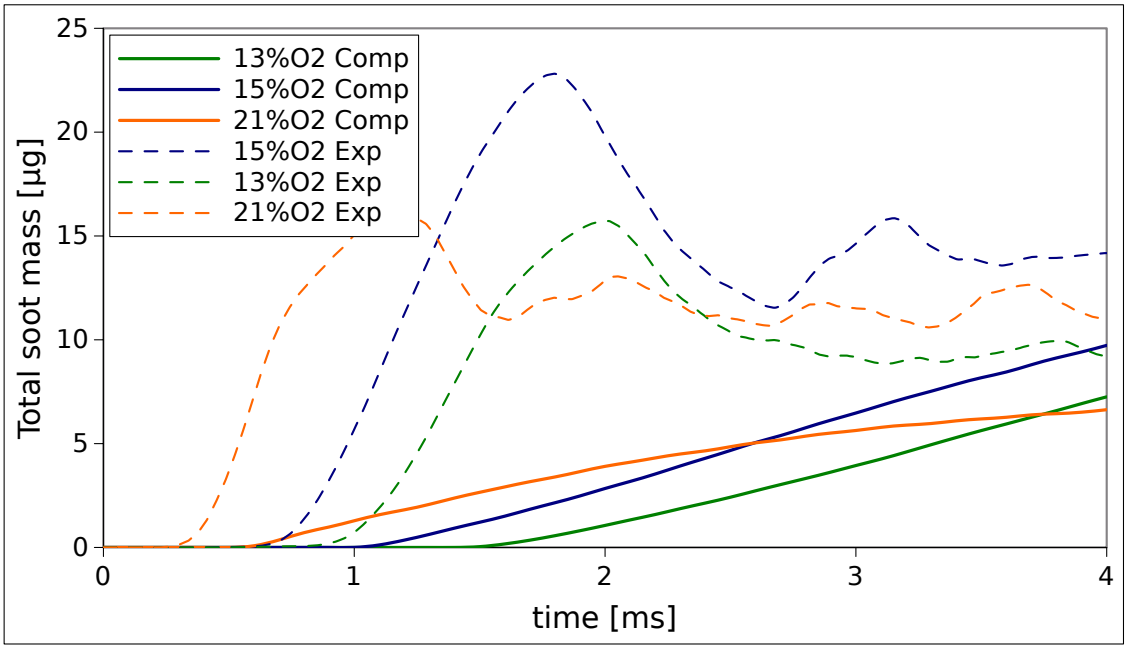

(a) Absolute

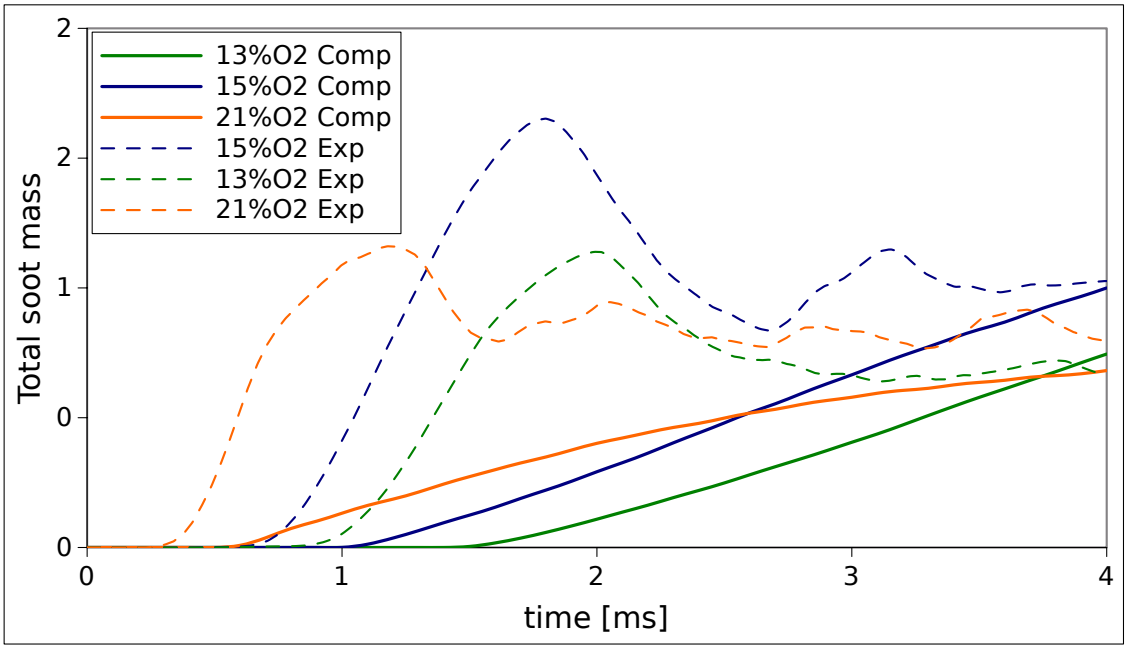

(b) Normalized

Figure 6.26. Comparison of total soot mass computed (full lines) with the model of Lindstedt with the experimental values (dashed lines) taken from [69] for different oxygen concentrations.

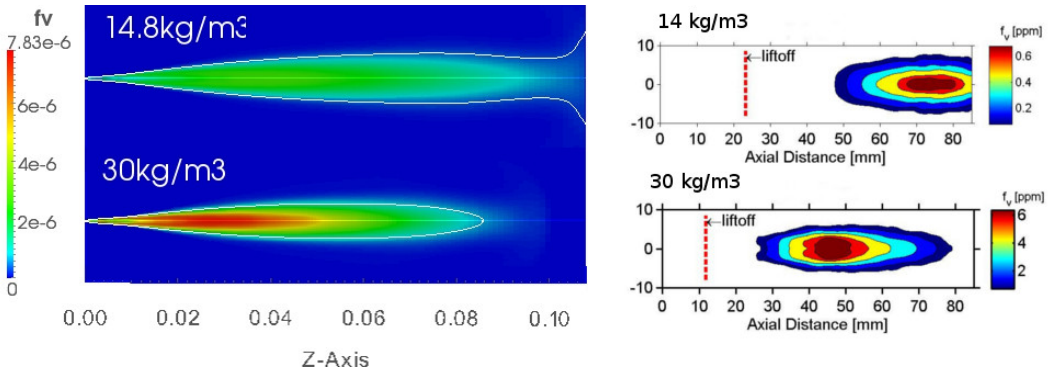

(a) (b)

Figure 6.27. Soot volume fraction computed (a) with the model of Lindstedt and measured (b) by [69] for different ambient densities.

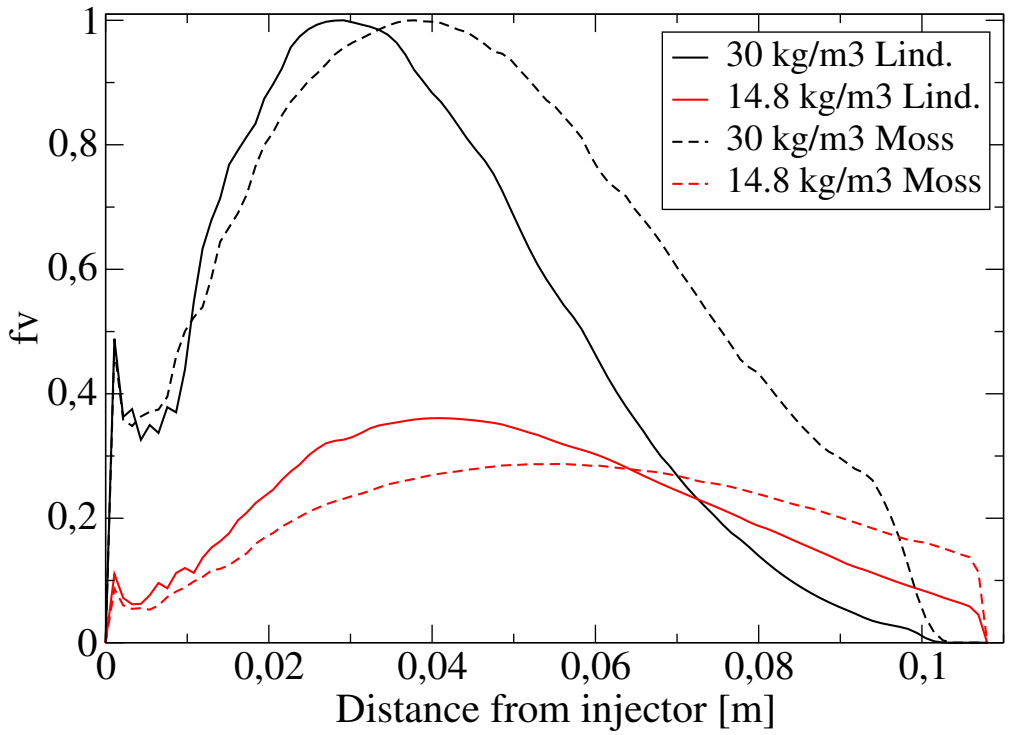

Figure 6.28. Normalized f_v axial profiles computed with the models of Moss (dashed lines) and Lindstedt (full line) and single RIF model for different ambient densities.

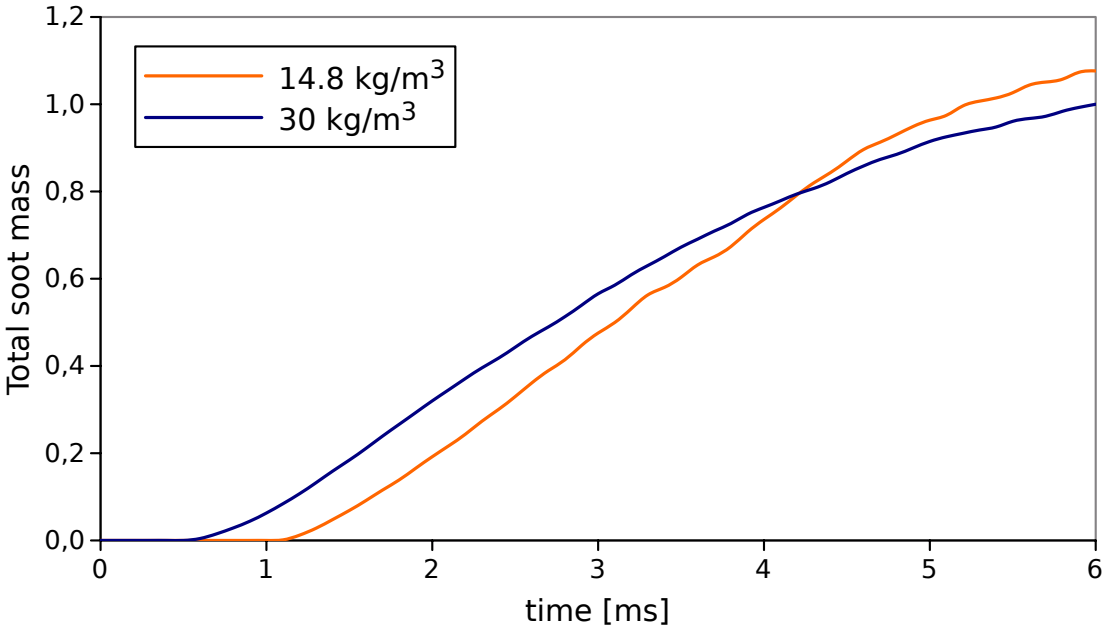

Figure 6.29. Total soot mass computed with the model of Lindstedt and single RIF model for different ambient densities.

6.3 Validation of soot models with multiple RIF model

In this section the same analysis performed previously with one flamelet will be carried out with multiple flamelets approach. The validations will be performed for the models of Moss and Lindstedt and not for the model of Wen because the first two have shown a better behaviour in the single flamelet analysis.

Simulations were performed on a 12 processors Intel(R) Xeon(R) CPU X5670 @ 2.93GHz.

6.3.1 Preliminary analysis at reference conditions

Before presenting the results of simulations with multiple RIF combustion models, a preliminary analysis is carried out in order to evaluate the minimum number of flamelets to be used in the following validation and which guarantee accuracy in soot prediction along with a limited computational time. Then, a comparison on flame structures obtained with single flamelet and multiple flamelets approaches is presented to provide a basis for the following validations of soot models. This study will be conducted at reference conditions reported in tab. 6.7.

Number of flamelets

Normally, a good assumption is to introduce a new flamelet each 0.1 ms. In order to limit the computational cost which increase with raising the number of flamelets, an end time of 0.4 ms has been chosen, hence 40 flamelets should be used. However, Colombi, in his work on RIF validation [88], showed that no significant

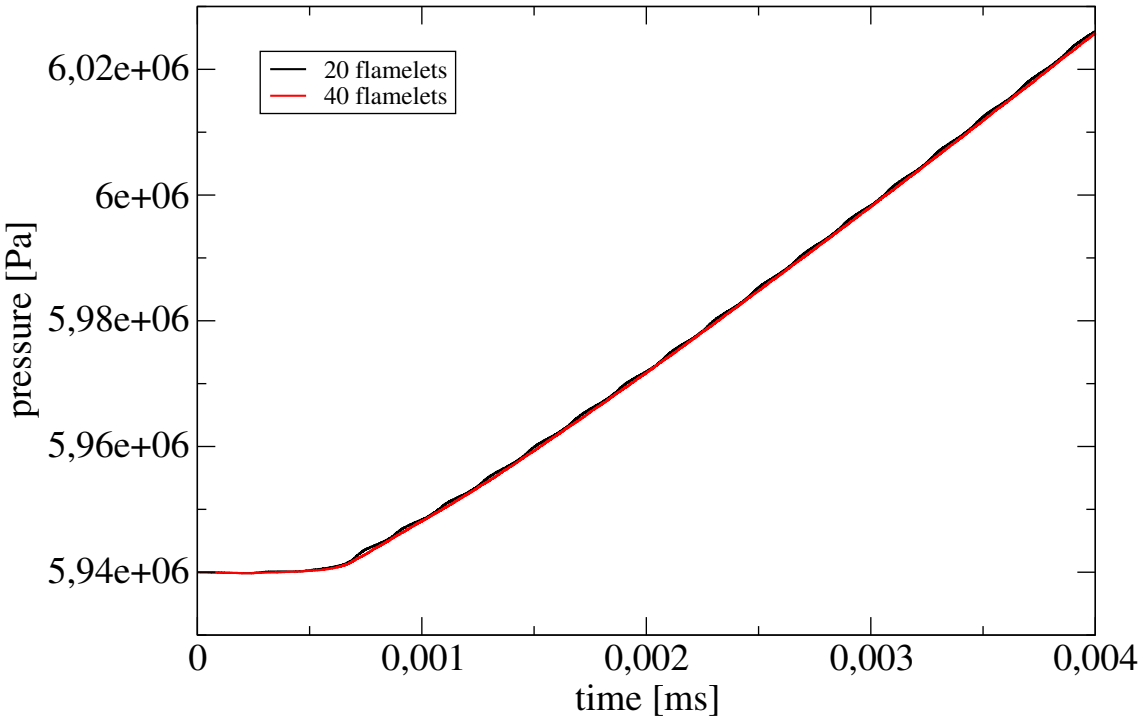

Figure 6.30. Pressure computed with 20 flamelets and 40 flamelets approaches at reference conditions.

differences are detected with increasing the number of flamelets over a certain value. Therefore, a concise analysis is conducted comparing simulations with 20 flamelets and 40 flamelets at reference conditions.

In fig. 6.30 the pressure trends for the two case are reported. The ignition delay is the same (about 0,6 ms) and curves are close to each other. With a higher number of flamelets, local oscillations associated to the ignition of flamelets are less visible because the mass of fuel related to the single flamelet is smaller. No significant differences in LOL values are observed, as reported in tab. 6.14.

Table 6.14. Measured and computed with m-RIF model LOL for reference conditions.

Measured LOL [mm]	20 flamelets [mm]	40 flamelets [mm]
16.1	17.2	17.8

Distributions of temperature, mixture fraction, chemical species, f_v or n_{soot} in physical domain are very similar, especially during diffusive combustion and in quasi-steady state. Only during the early stages of combustion slight differences are observed: with 40 flamelets there is an area in the centre of the jet a little richer, resulting in a lower temperature and a higher concentration of C_2H_2. This is probably due to the greater number of young flamelets just formed which are at the initial phases of mixing with air and reactions. These differences do not greatly affect soot results, as it can be deduced from total soot mass trends reported in fig. 6.31.

At 4 ms the computation with 40 flamelets predicts a total soot mass lower of

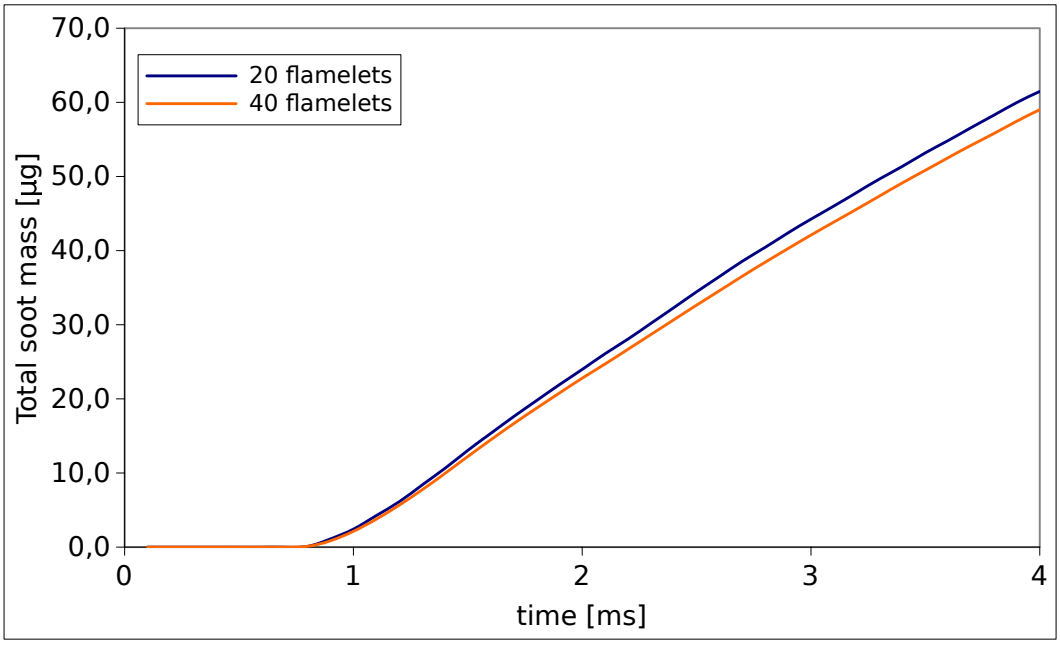

Figure 6.31. Total soot mass trends computed with 20 flamelets and 40 flamelets approaches with soot model of Moss.

3 µg then that of 20 flamelets case. This deviation of the two values is likely due to the difference noted above: increasing the number of flamelets, the injected fuel is virtually divided into smaller portions that react each following its own history, allowing a better simulation of the actual kinetics of combustion. In this way also processes leading to soot formation are slower and they are developed following more properly the real chemical and physical dynamics of soot.

In conclusion, the multiple RIF with 20 flamelets will be used for the following validation of soot models because it does not compromise the accuracy with a considerable reduction of CPU time compared with 40 flamelets computations for simulations that last 4 ms. Moreover, it was considered appropriate for the purposes of the present analysis not to further pursue in decreasing the number of flamelets in order to stress the comparison with single flamelet analysis.

Flame structure comparison

In fig. 6.32 approximate heat release rates computed with single RIF model and 20 flamelets approach compared with the experimental one at reference conditions are reported.

With 20 flamelets, as already noted, ignition delay decreases, although it is still overestimated as reported in tab. 6.15.

This reduction is due to the fact that, for the case with more flamelets, as long as there is only the first flamelet, its scalar dissipation rate is identical to that of the case with only one flamelet. When, however, the second flamelet is created, the SDR of the first decreases faster then the one of the case with one flamelet, leading to a more rapid auto-ignition. This causes a smaller amount of fuel which reacts during the premixed burn, with a lower peak of heat release rate. As seen in fig. 6.32,

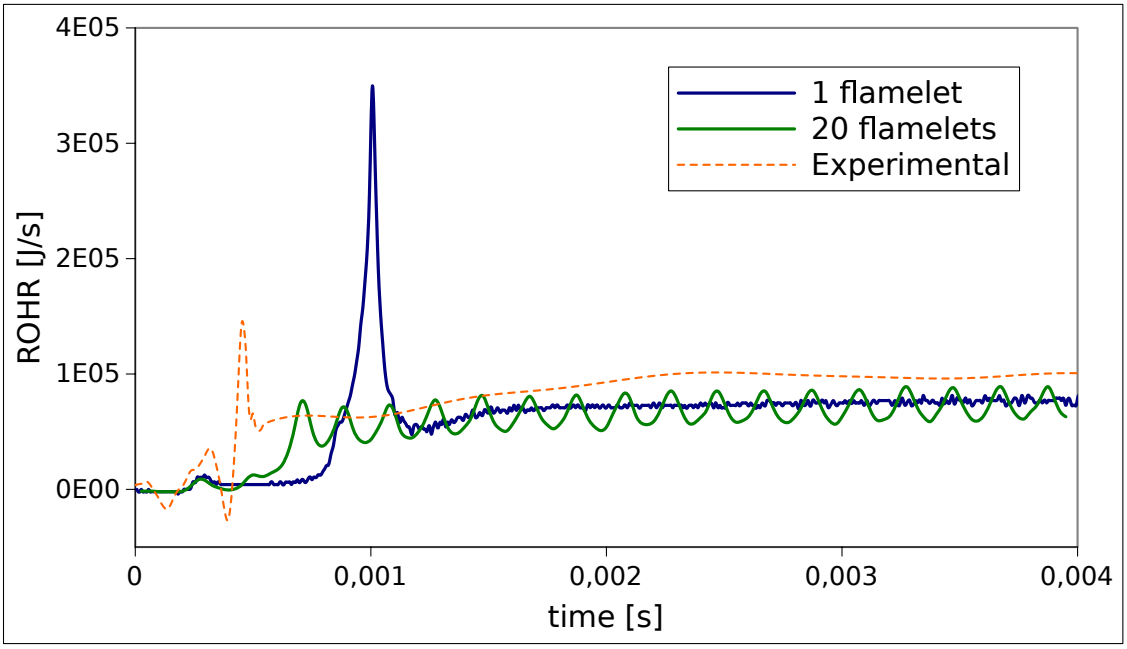

Figure 6.32. Comparison between ROHR computed with single flamelet and multiple flamelets models.

Table 6.15. Computed ID and LOL with single RIF and multiple RIF models

	ID [ms]	LOL [mm]
Measured	0.4	16.1
single flam.	0.9	0
multiple flam.	0.6	17.2

however, the ignition of the subsequent flamelets leads to not physical peaks of heat release during the mixing controlled combustion. As expected, with 20 flamelets the flame lifts from the nozzle and the LOL is predicted with a good accuracy (tab. 6.15).

Indeed, as it is possible to see in fig. 6.33, profiles of maximum of temperature and OH do not extend up to the injector hole: near the nozzle, upstream in the jet, there are the youngest flamelets, only recently created with the latest mass of fuel injected. These flamelets have still a high mean stoichiometric scalar dissipation rate and have not yet ignited, allowing the reactions to take place at a certain distance from the injector. As a consequence, distributions of mixture fraction and C_2H_2 is completely different (fig. 6.34).

Due to to the high scalar dissipation rate of the youngest flamelets, there is an enhancement in the mixing of fuel with air leading to maximum values of Z significantly lower and in general a less rich jet, especially in the zone where premixed combustion occurs. These factors result in a drastic reduction in both the extent of the region in which the acetylene is present and in its concentration, which means that, correctly, the region of potential soot nucleation is more confined and soot can form and grow only at a certain distance from the injector. In terms of soot, comparison between one flamelets and 20 flamelets is performed with Moss model.

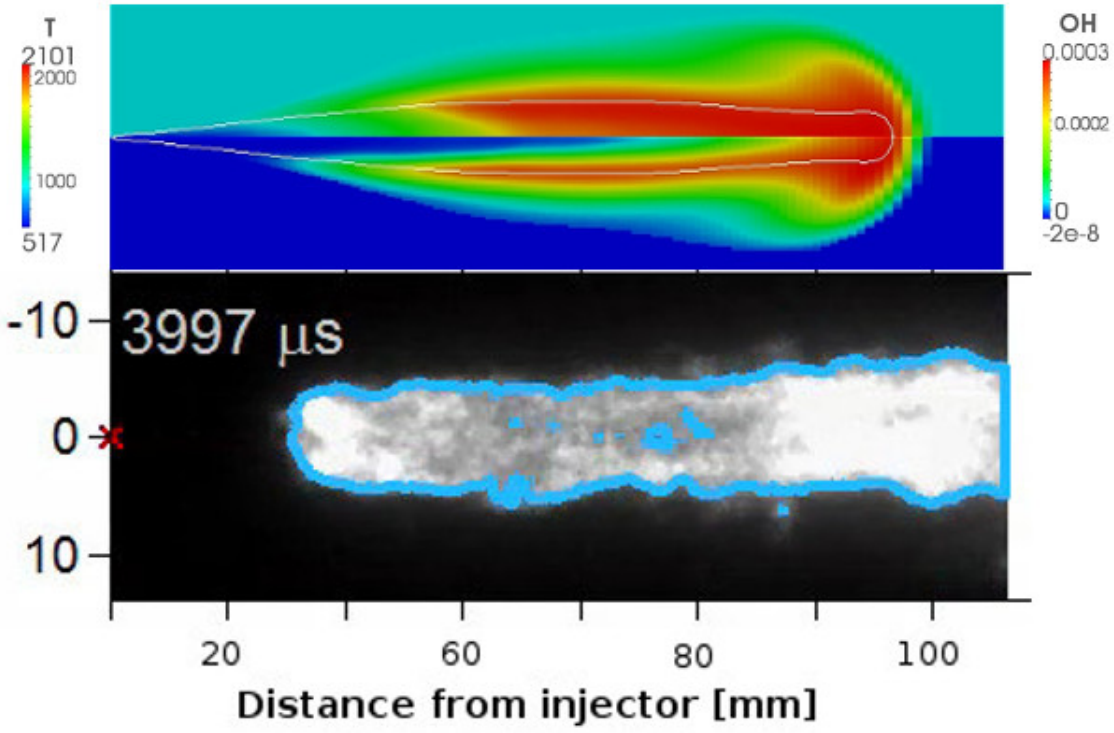

Figure 6.33. Temperature (top) and OH (bottom) fields for multiple RIF simulation. In the bottom half, natural luminosity image at reference conditions is reproduced where the blue line represent the 50% OH* chemiluminescence threshold.

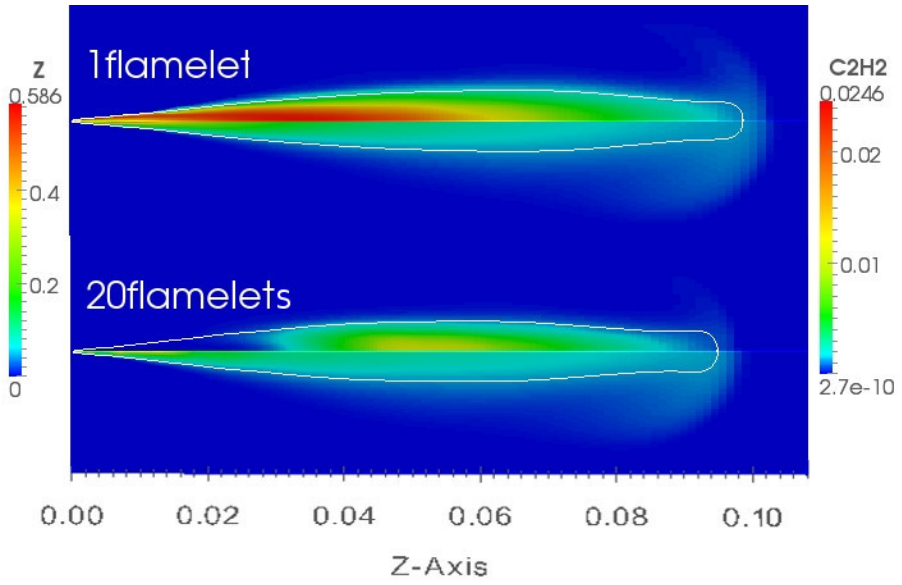

Figure 6.34. C_2H_2 (top half) and Z (bottom half) fields for single flamelet and multiple flamelets simulations.

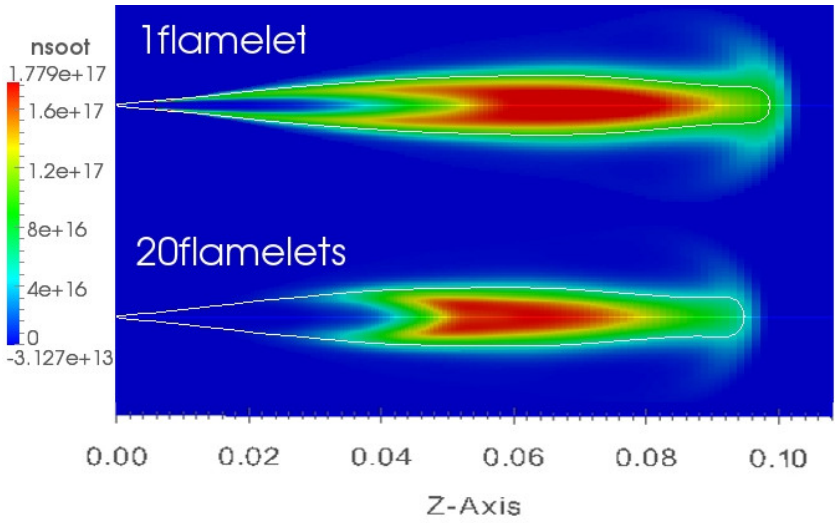

Figure 6.35. Particle number density fields for single flamelet (top frame) and multiple flamelets (bottom frame) simulations.

Fig. 6.35 compares soot particle number density for the two cases. For 20 flamelets case, soot nucleates at a finite distance from the injector, even greater than the LOL, which is consistent with experimental observations, because of time required by the kinetics of nucleation and surface growth processes. It is also noted a decrease in the number of particles associated with the lesser richness of the jet.

In fig. 6.36 computed f_v distributions, at 1.5 ms and 4 ms respectively, are compared with experimental ensemble-averaged optical thickness KL and, for the second case, with the f_v time-averaged over the quasi-steady period. It can be observed an excellent agreement with the experimental measurements both in terms of distribution, both of absolute values. As for the case with a single flamelet, the temporal development of the soot is correct, with an initial peak concentration in the head vortex of jet and, with the attainment of a quasi-steady condition, its elongation across the rich region of the flame.

For a more detailed comparison, axial trends of f_v, computed and experimental, are shown in fig. 6.37. The result is very good: the on-set soot location and the gradient of f_v growth computed match the experimental ones very satisfactorily. Peak location is slightly further downstream and also its absolute value is very little overestimated. These observations confirm that, with an adequate prediction of the structure of the flame, the model of Moss, and, as will be seen in more detail later, also the Lindstedt model, capture correctly the global soot processes.

The total soot mass, fig. 6.38, decreases considerably, as a result of considerations made previously, becoming less than half the amount obtained with one flamelet. Since, as said, the experimental total soot mass seems not to be a complete data, the value obtained at 4 ms, 63 µg, though likely overestimated, are more comparable with the experimental one (14 µg). The soot on-set time, comprised between 0.7 ms and 0.8 ms, is closer to the experimental 0.73 ms and up to 2 ms, almost when the experimental mass reported is actually all that present in the jet, the results are very encouraging with a very good agreement between the calculated and experimental data. Although the time derivative is decreased, the trend still does not stabilize

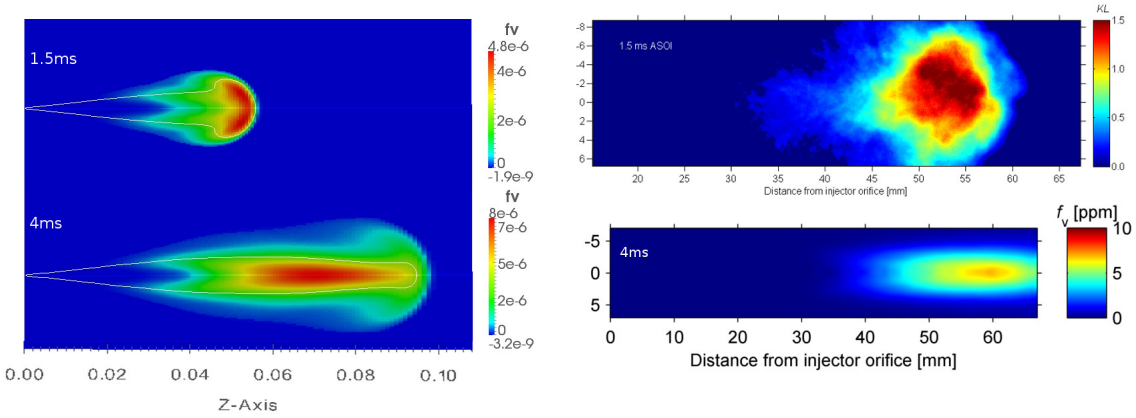

(a) Computed (b) Experimental

Figure 6.36. Comparison of f_v fields computed with multiple RIF (a) and KL and f_v measured (b) by [69], respectively at 1.5 ms and 4 ms

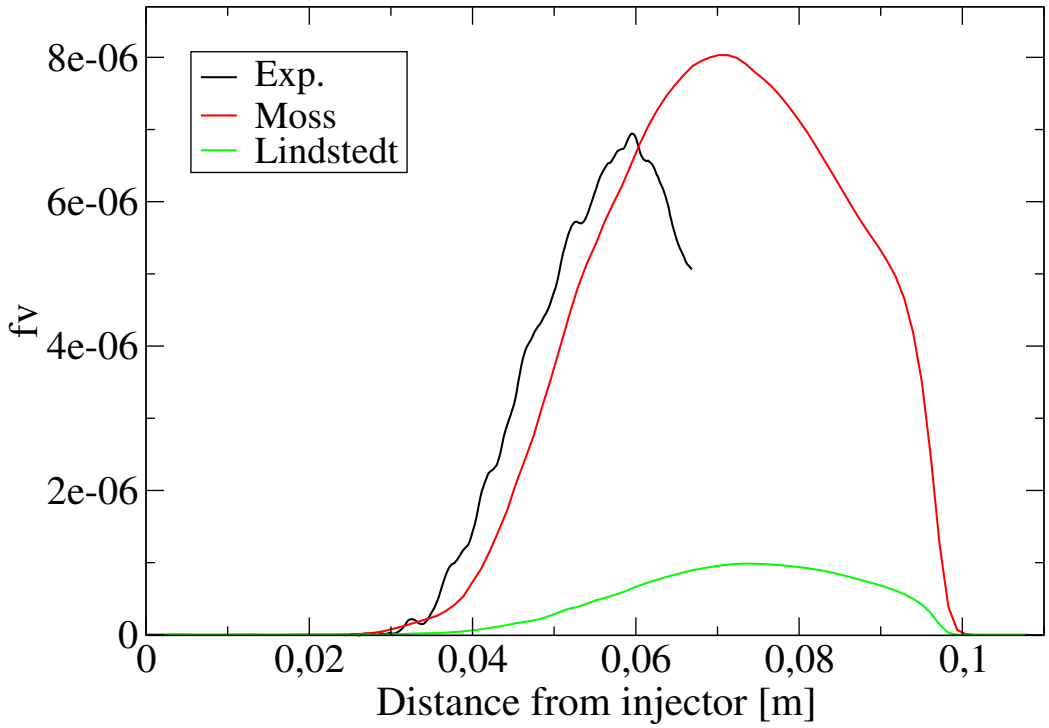

Figure 6.37. Axial f_v computed with multiple RIF and the model of Moss (red line) and Lindstedt (green line) at reference conditions. Experimental trend (black line) is reported for comparison.

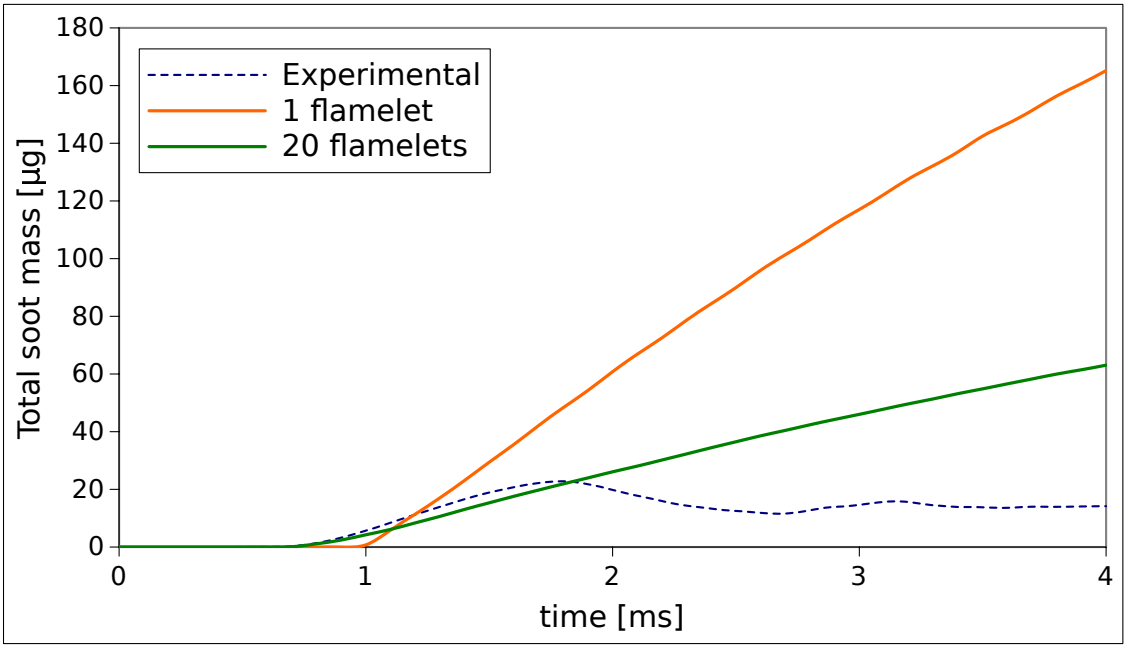

Figure 6.38. Total soot mass computed with 20 (green line) and 40 flamelets (orange line) compared with the experimental one (dashed line) at reference conditions.

within 4 ms.

6.3.2 Validation of soot models: Moss

Influence of ambient temperature

In tab. 6.16 ignition delays and lift-off lengths for the three cases compared with the experimental ones are listed. The heat release rates as a function of time are not reported because considerations made above for the case in reference conditions and for the cases with one flamelet, are still valid. Trend of variations of ignition delays is correct. They are still overestimated but the error decreases compared to using only one flamelet and as the temperature increases, as already noted. Moreover, with increasing temperature, greater oscillations are present in the computed trend of heat release, probably due to the higher rates of reaction when flamelets ignite. The result related to LOL is more significant: trend with temperature is correct and values are close to the experimental ones, except that at 1000 K which is quite overestimated.

Table 6.16. Measured and computed with multiple RIF LOL and ignition delay for different ambient temperatures.

	Measured LOL [mm]	Computed LOL [mm]	Measured ID [ms]	Computed ID [ms]
850 K	20.6	19.0	0.59	0.8
900 K	16.1	17.2	0.4	0.6
1000 K	11.5	14.2	0.32	0.45

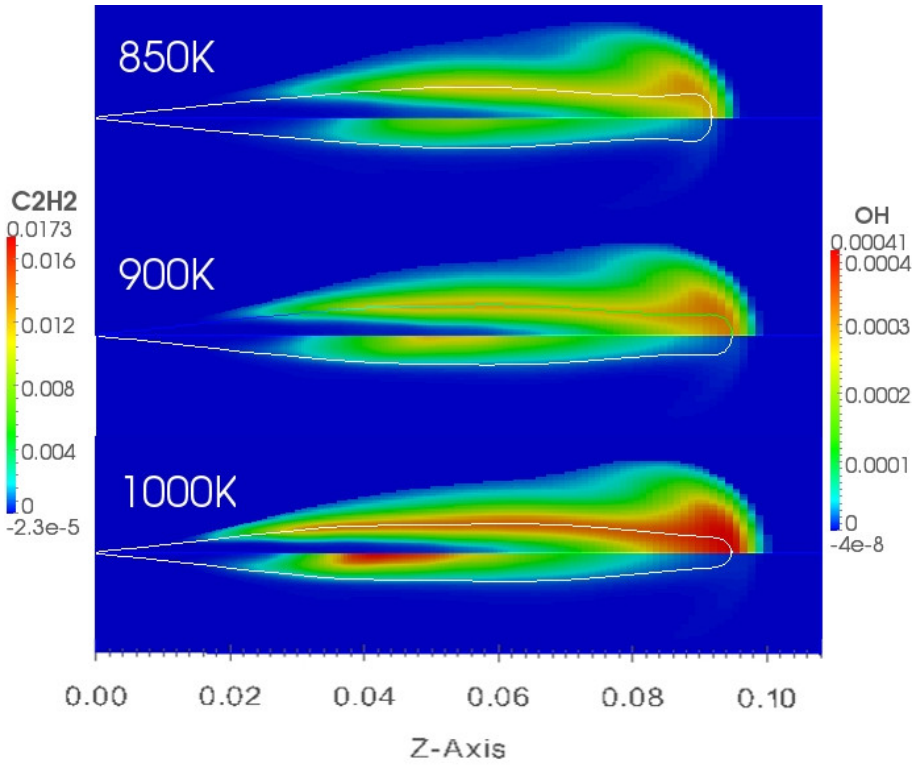

Figure 6.39. Comparison of C_2H_2 and OH fields for different ambient temperatures. The C_2H_2 and OH fields are respectively shown in the bottom and in the top half of each frame.

In fig. 6.39 distributions of C_2H_2 and OH at 4 ms are reported for the three cases. The flame structure is similar: the flame length is slightly increasing with decreasing temperature, even if at 4 ms it is only intuitable by the development of the profiles of the stoichiometric mixture fraction. With increasing temperature, maximum flame temperature rises approximately of the same quantity and thanks to the minor LOL, with increasing temperature, the reaction and the high temperature zones extend closer to the injector. Furthermore, coherently with experimental measurements, as the temperature increases, the value of Z at LOL grows, leading to a richer premixed combustion. Indeed, values of C_2H_2 mass fraction increase and are distributed over a larger region further upstream in the jet. Moreover, in agreement with the experimental observations, the values of the OH mass fractions are higher, due to the increase of reaction rates with increasing temperature.

Distributions in physical domain of computed and experimental f_v are reported in fig. 6.40. The axial trends are shown in fig. 6.41. In terms of both absolute values and distributions, a good match can be observed. Variation with ambient temperature is correct and also the shift upstream of the peaks with increasing temperature is properly captured, although their positions are slightly downstream with respect to the experimental one and distributions are axially more extended. This, for the two cases at higher temperature, seems to be due to the overestimation of LOL and, for all cases, perhaps, to a not perfect balance of the constants of the models of formation and oxidation or to a too lower oxidation reactivity. For the case at 850 K, there is a deviation from the experimental values more consistent than the other cases. A possible reason is that it is the unique case in which the

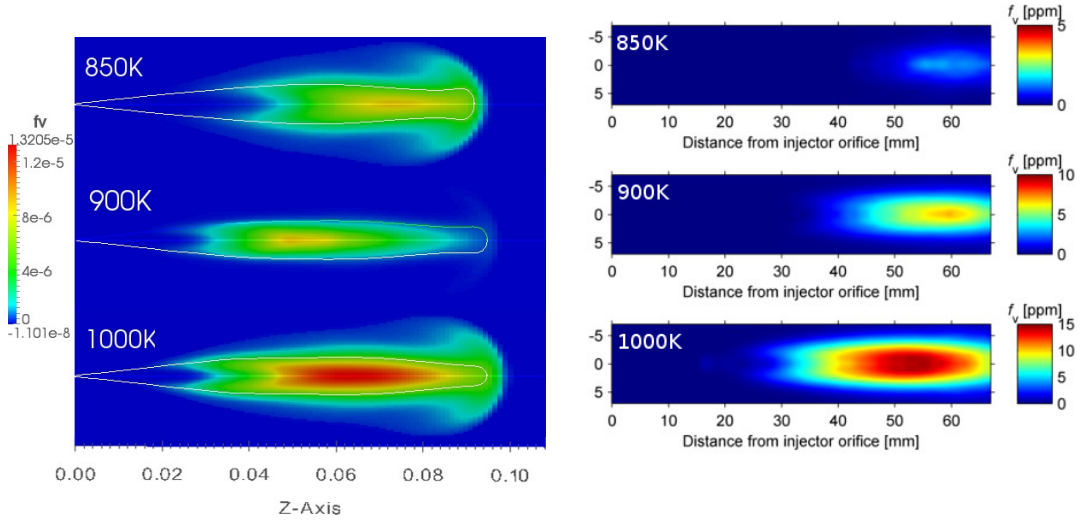

(a) (b)

Figure 6.40. Soot volume fraction computed (a) with the model of Moss and measured (b) by [69] at different ambient temperatures.

LOL is underestimated. In fact, the on-set axial location of f_v is further upstream than the experimental value.

Consequently, also the trend of variation of the total soot mass is correct: fig. 6.42 shows absolute and normalised values and some results are summed up in tab. 6.17.

Table 6.17. Soot data for different ambient temperatures computed with Moss and multiple RIF models. Normalized quasi-steady soot values are reported in brackets.

	Exp. soot on-set time [ms]	Comp. soot on-set time [ms]	Exp. quasi-steady soot value [µg]	Comp. quasi-steady soot value [µg]
850 K	1.14	0.95	2(0.143)	42.4 (0.86)
900 K	0.73	0.75	14 (1)	63 (1)
1000 K	0.47	0.5	42 (3)	93.4 (1.48)

Compared to the total soot mass obtained with single flamelet computations, trends resulted from multiple RIF simulations show more variations and are more aligned with the experimental ones, although still somehow underestimated. Certainly, this might be due to the lifted flame, even if it does not allow to fully capture the magnitude of the changes with temperature of the soot produced. This drawback can be attributed, at least partially, to the semi-empirical nature of the model of soot, that represents the complex kinetics of soot in a comprehensive manner and that can not take into account the effect of temperature on the many stages of the chemical processes that leads to the formation of soot.

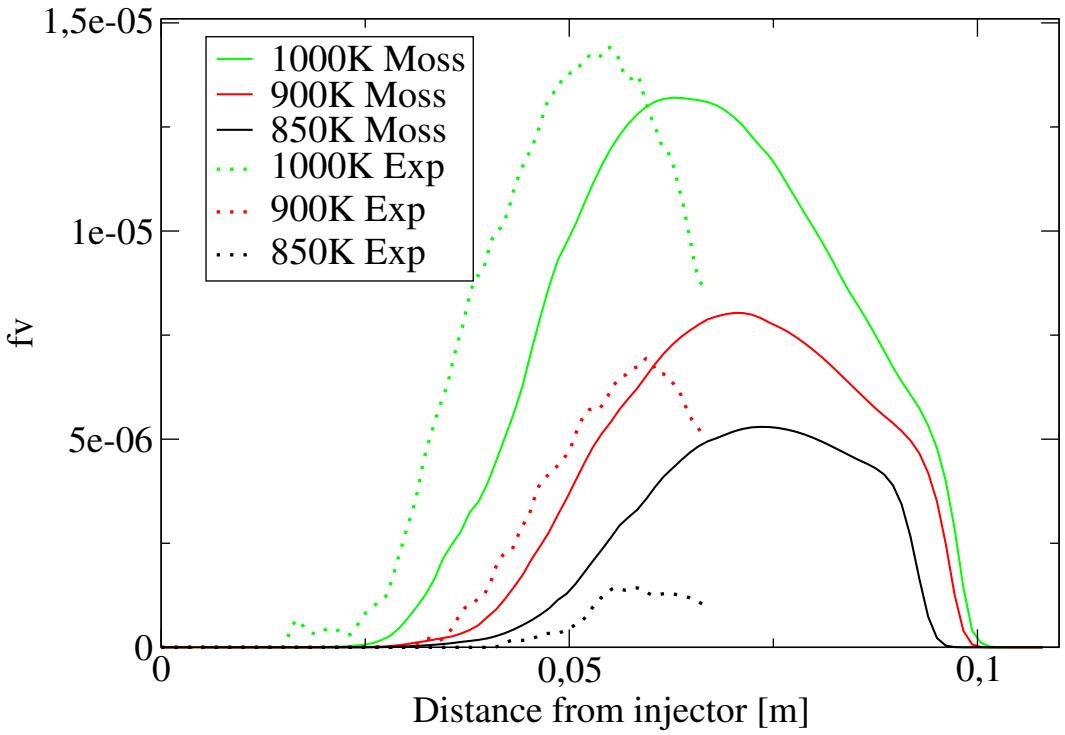

Figure 6.41. Axial f_v computed with multiple RIF and the model of Moss for different ambient temperatures. Experimental trends (dot lines) are reported for comparison.

Influence of oxygen concentration

Tab. 6.18 summarizes the main global characteristics of the flames, experimental and computed, for the three different initial oxygen concentrations.

Table 6.18. Measured and computed with multiple RIF LOL and ignition delay for different oxygen concentrations.

	Measured LOL [mm]	Computed LOL [mm]	Measured ID [ms]	Computed ID [ms]	Z_{stoich}	Computed T_{max} [K]
13%	20.4	19.2	0.47	0.8	0.0393	1968
15%	16.1	17.2	0.4	0.6	0.045	2103
21%	9.9	13.9	0.28	0.45	0.0614	2450

Even with multiple RIF as with single RIF, changes in the ignition delay and LOL are captured correctly, although for the case with 13% of O_2, the LOL is slightly underestimated and it is overestimated for the case with 21% of O_2

Ignition delay is always overestimated for all cases. Considering heat release rates, compared to simulations with one flamelet, similar trends are observed, with lower errors for the ignition delays and growing oscillations with increasing ambient oxygen concentration, associated with the higher reactivity of the individual flamelets, with a faster heat release.

Variations of flame structure are similar to the case with one flamelet: increasing

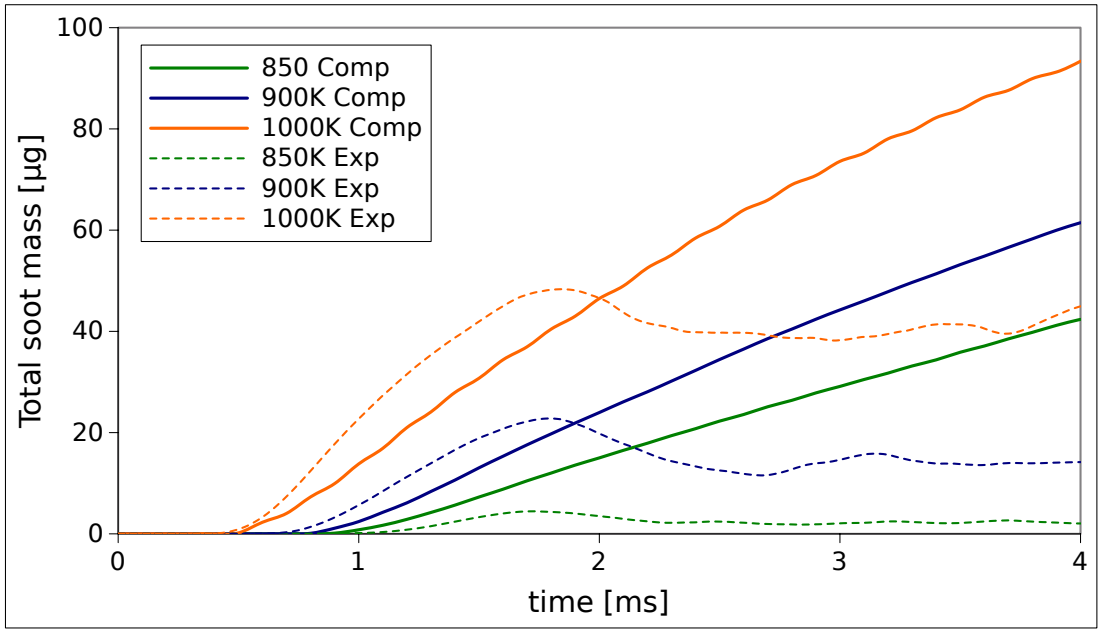

(a) Absolute

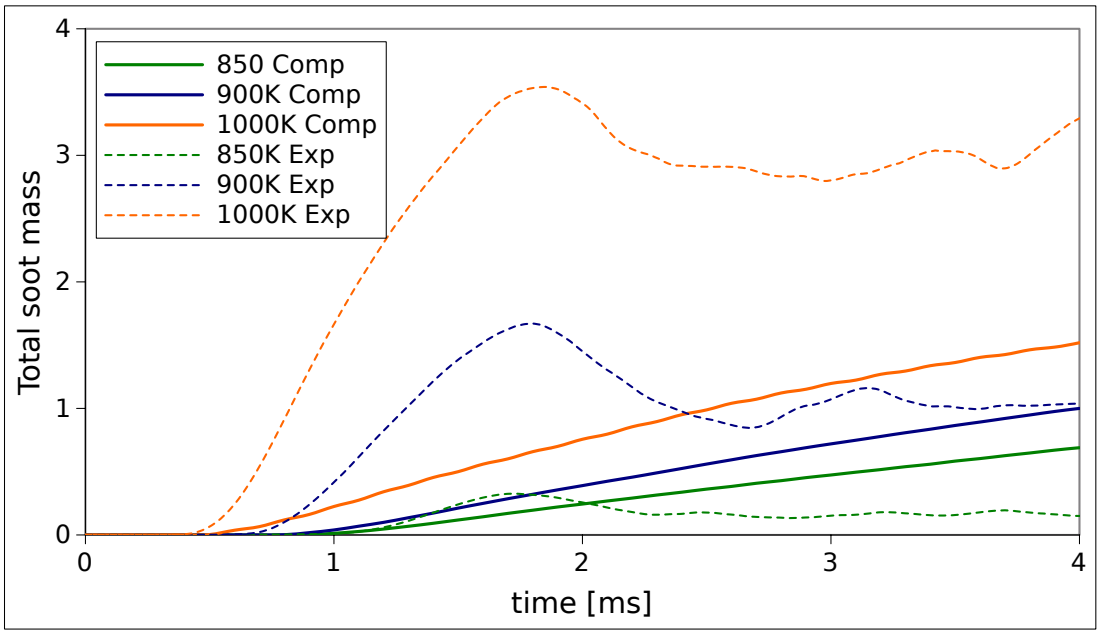

(b) Normalized

Figure 6.42. Comparison of total soot mass computed (full lines) with the model of Moss with the experimental values (dashed lines) taken from [69] for different ambient temperatures.

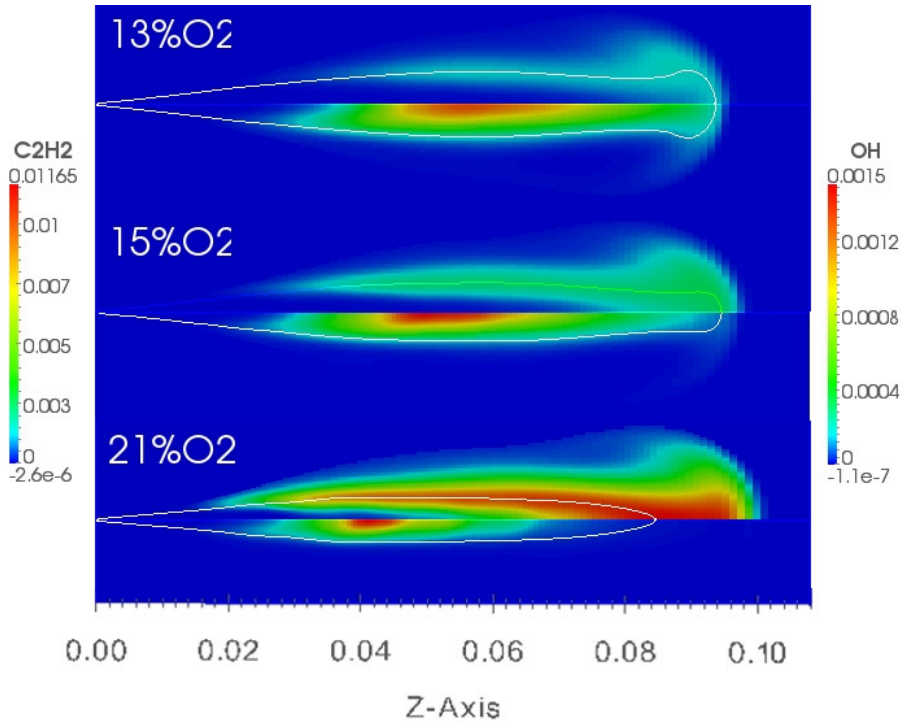

Figure 6.43. Comparison of C_2H_2 and OH fields for different oxygen concentrations. The C_2H_2 and OH fields are respectively shown in the bottom and in the top half of each frame.

oxygen concentration, Z_{stoich} increases and flame becomes gradually smaller both axially and radially. In this way, regions where acetylene is present are smaller and more shifted towards the injector, but with higher concentration of this soot precursor (fig. 6.43). At the same time OH concentration increases a lot, due to the greater temperature, accelerating the oxidation of soot. These conditions lead to results related to soot in agreement with the experimental observations, as can be deduced from fig. 6.44.

With decreasing oxygen amount in the air, sooting regions, in terms of both soot particle number density and soot volume fraction, are characterized by lower concentration of soot but are shifted further downstream and more extensive, radially and axially (for the case with 13% O_2 this latter statement is less visible because the flame at 4 ms has not yet reached a stable position).

f_v axial trends are reported in fig. 6.45. Trends of growth and oxidation are correct, more pronounced with an increasing oxygen concentration, although for all three cases at the on-set soot location initial growth seems to be a bit slowed. In terms of variations, trend is correct, even if, compared with temperature changes, they are quite overestimated.

Total soot mass trends are correctly predicted, as inferred from fig. 6.46. There is some overestimation in the decrease of soot mass in the switch to the condition to 21% O_2. This can be attributed, in part, to the fact that the experimental data in this condition is more representative of the effective total mass present in the jet, because the flame is almost completely within the field of view of experimental detection. In fact, this is also the case in which there is the greatest agreement with the experimental data (see also the tab. 6.19).

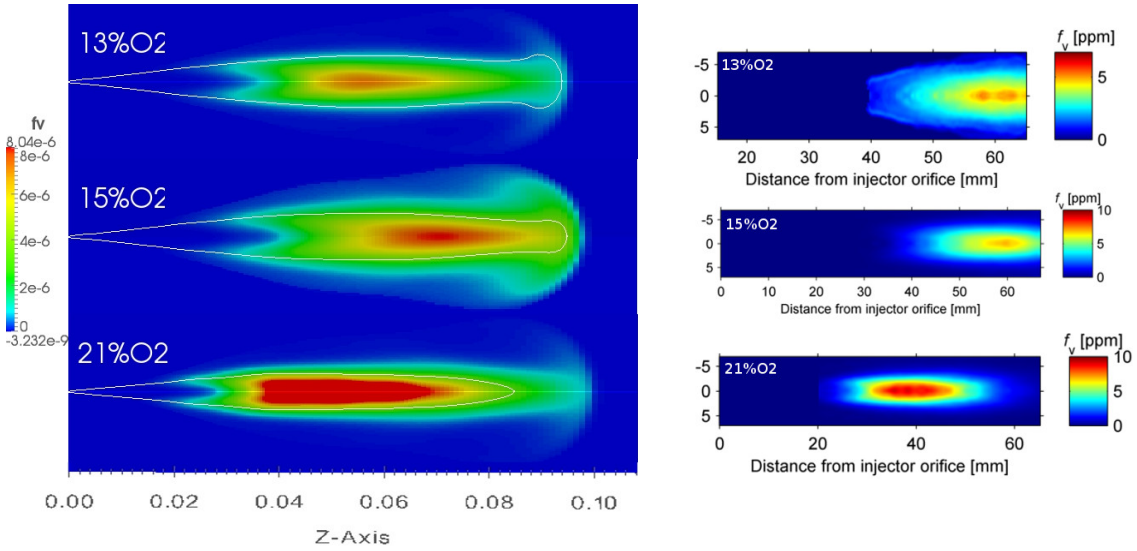

(a) (b)

Figure 6.44. Soot volume fraction computed (a) with the model of Moss and measured (b) by [69] at different oxygen concentrations.

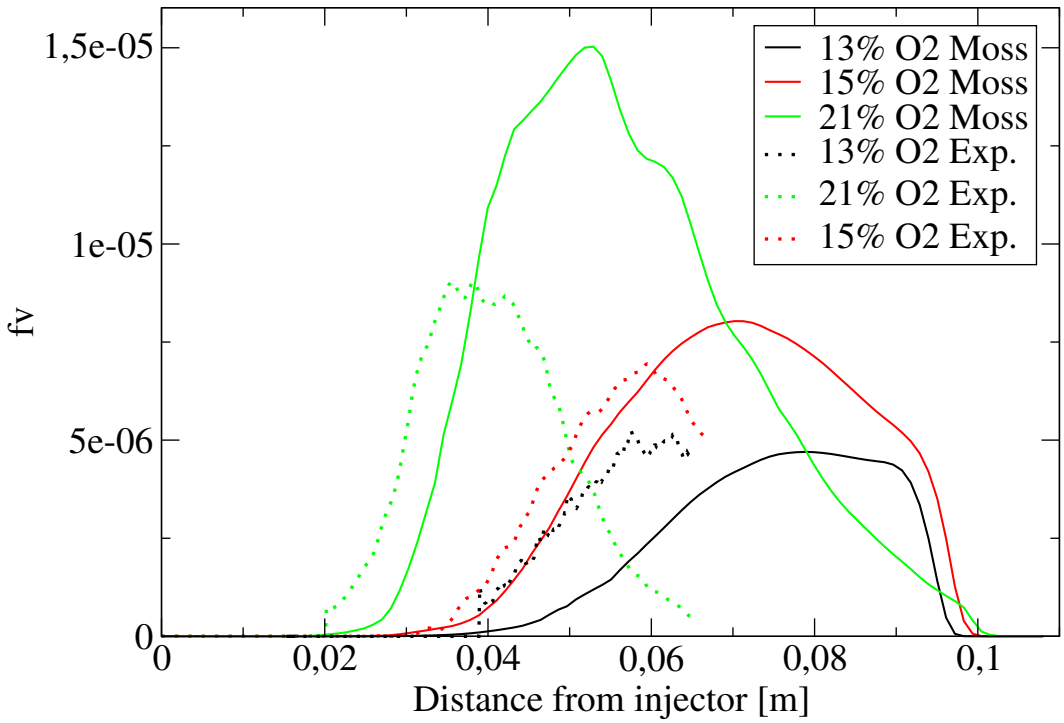

Figure 6.45. Axial f_v computed with multiple RIF and the model of Moss for different oxygen concentrations. Experimental trends (dot lines) are reported for comparison.

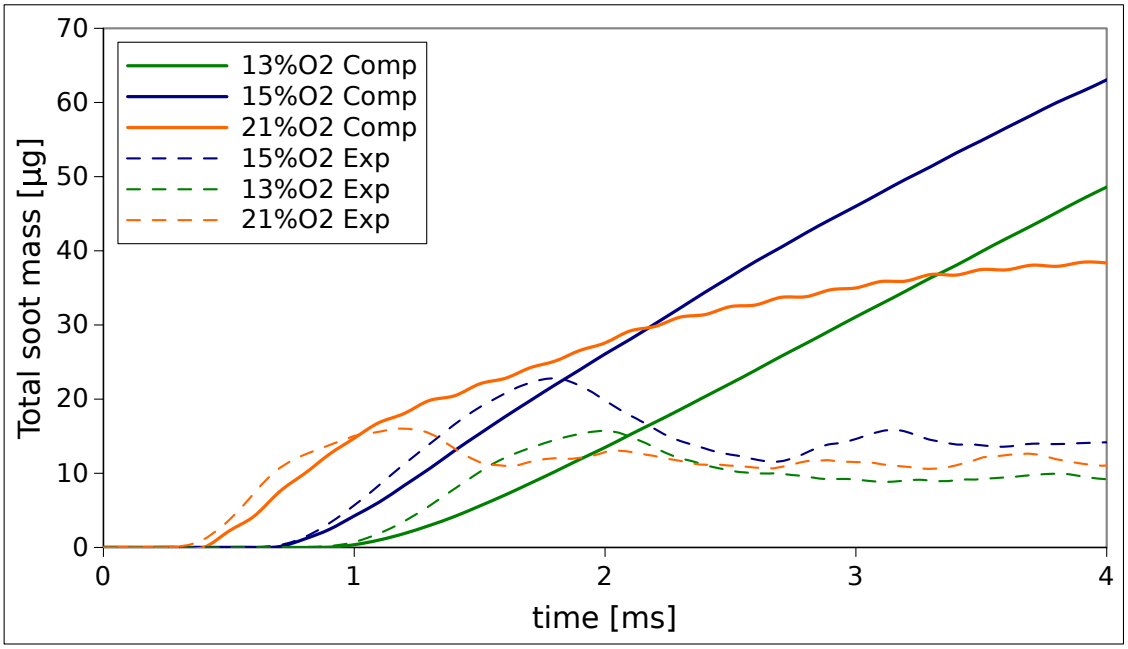

(a) Absolute

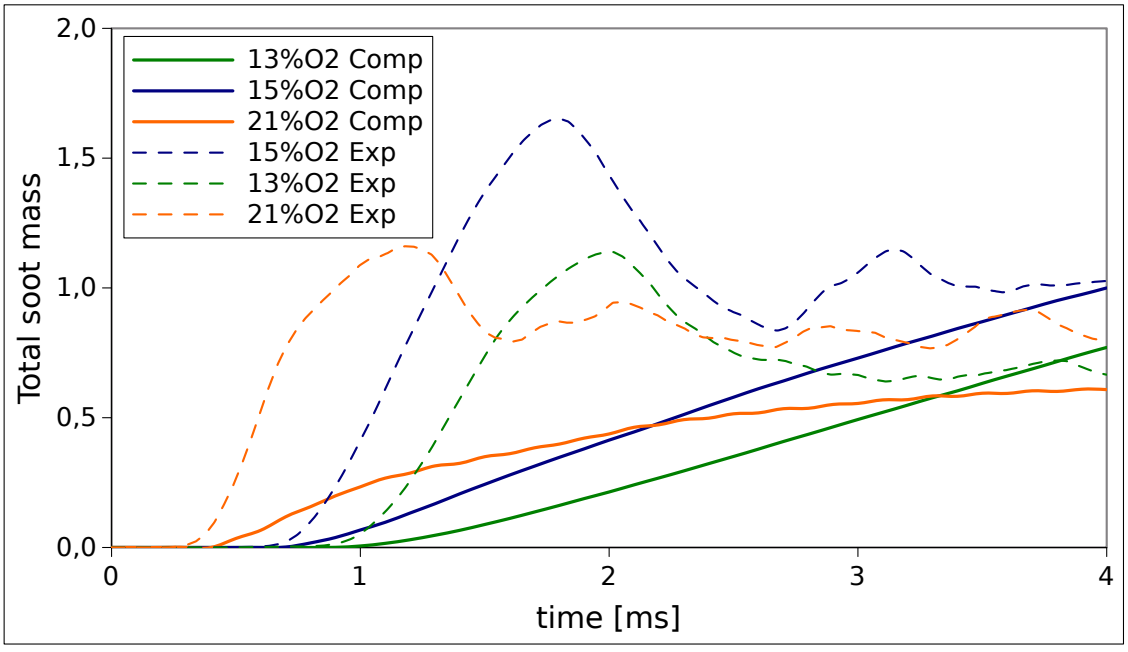

(b) Normalized

Figure 6.46. Comparison of total soot mass computed (full lines) with the model of Moss with the experimental values (dashed lines) taken from [69] for different oxygen concentrations.

Table 6.19. Soot data for different oxygen concentrations computed with Moss and multiple RIF models. Normalized quasi-steady soot values are reported in brackets.

	Exp. soot on-set time [ms]	Comp. soot on-set time [ms]	Exp. quasi-steady soot value [µg]	Comp. quasi-steady soot value [µg]
13%	0.97	1	10 (0.71)	48.6 (0.77)
15%	0.73	0.75	14 (1)	63 (1)
21%	0.36	0.4	11 (0.786)	38.4 (0.6)

Influence of ambient density

Operating conditions and main features of the two spray-H cases are summed up in tab. 6.20.

Table 6.20. Measured and computed with multiple RIF LOL and ignition delay for different ambient densities.

	Measured LOL [mm]	Computed LOL [mm]	Measured ID [ms]	Computed ID [ms]
14.8 kg/m^3	23.4	24.4	0.73	0.9
30 kg/m^3	11.9	13.8	0.38	0.45

Observations about ignition delay and heat release rate are not reported because they are analogous to those made for cases with variation of temperature and oxygen concentration. LOL is computed with a good degree of accuracy although a slight overestimation for both cases is observed. The maximum temperatures are comparable, even though the temporal evolution of the lower density case is more delayed in time, not only for the greater ignition delay but also for the lesser reaction rates. Correctly, upstream of LOL, mixture fraction is greater with lower density, but at the axial location of lift-off values are similar.

In fig. 6.47, C_2H_2 and OH fields are shown. It is important to note that in this way, compared to simulations with one flamelet, now also the acetylene mass fractions are higher for the case at higher density, thanks to the ability to predict the LOL. An opposite situation occurs, on the other hand, for OH, perhaps due to the richer conditions that are generated in the flame with higher density, with iso-contour profiles of Z closer together.

As can be inferred from fig. 6.48 and fig. 6.49, qualitative variations of f_v in terms of values are corrected and the distributions match in an acceptable way with the experimental ones. Absolute values are largely overestimated, although, compared to results obtained with a single flamelet, they are decreased. This aspect is underlined by total soot mass trends, shown in fig. 6.50 for which the values are more than halved. More important is that, also in this case, trend of variation with density is corrected.

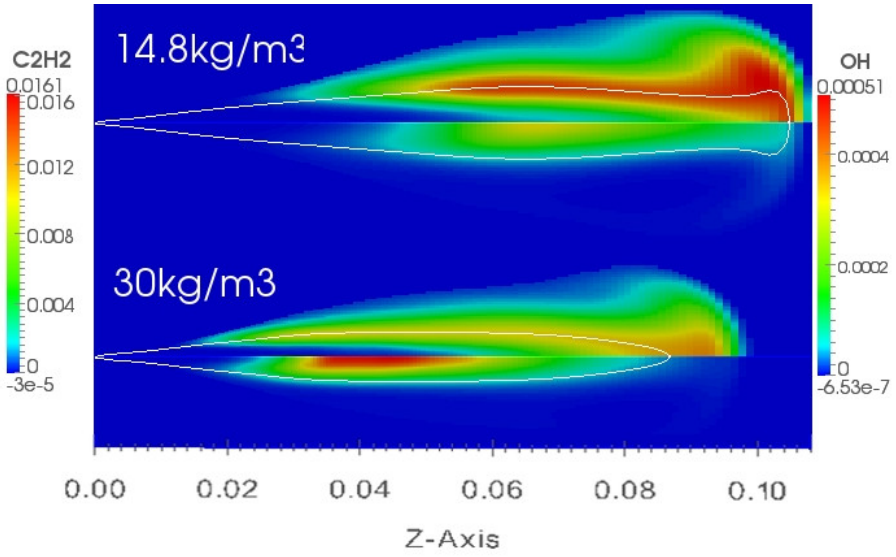

Figure 6.47. Comparison of C_2H_2 and OH fields for different ambient densities. The C_2H_2 and OH fields are respectively shown in the bottom and in the top half of each frame.

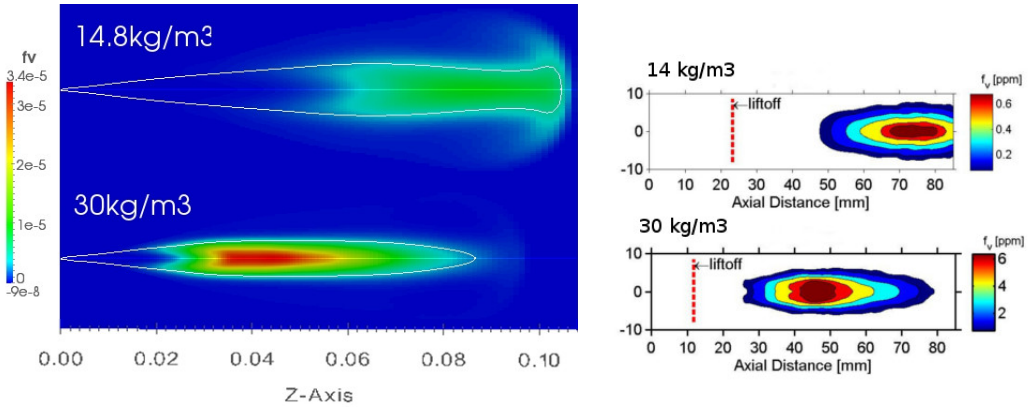

(a) (b)

Figure 6.48. Soot volume fraction computed (a) with the model of Moss and measured (b) by [69] at different ambient densities.

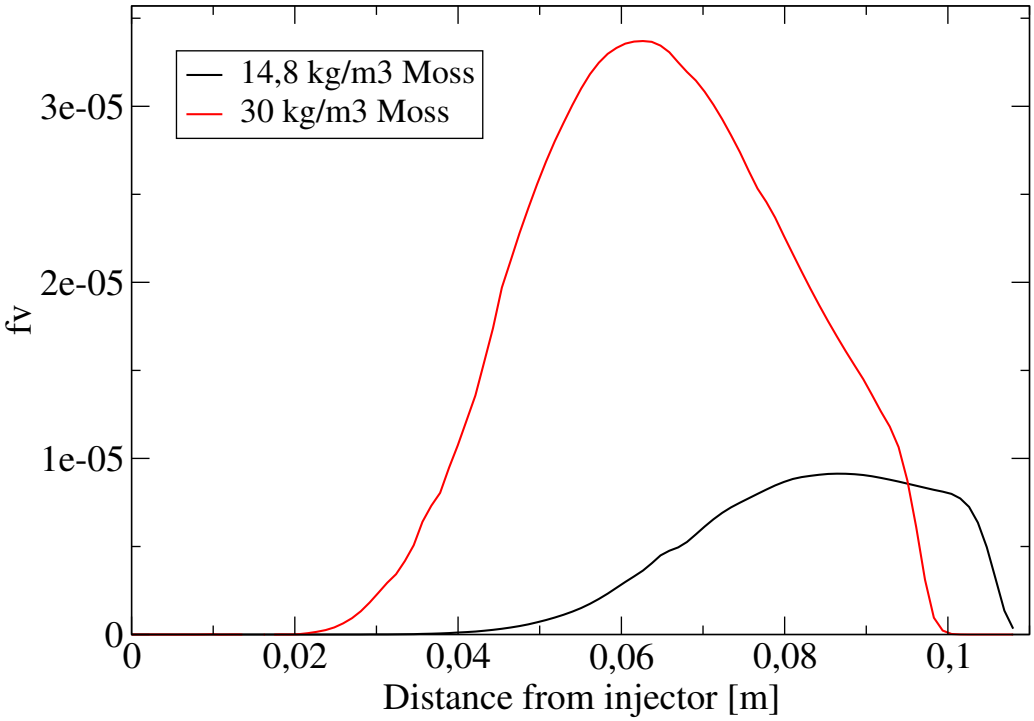

Figure 6.49. Axial f_v computed with multiple RIF and the model of Moss for different ambient densities.

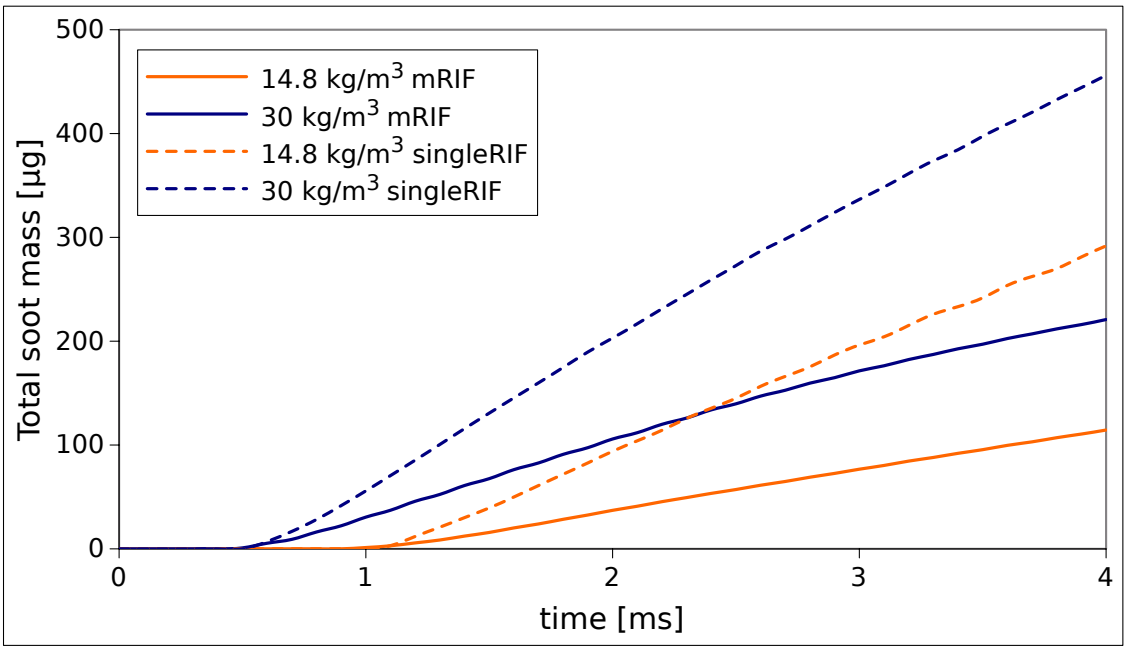

Figure 6.50. Total soot mass computed with the model of Moss and multiple RIF approach (full line) for different ambient densities. Values obtained with single RIF model are reported on the picture in dashed lines.

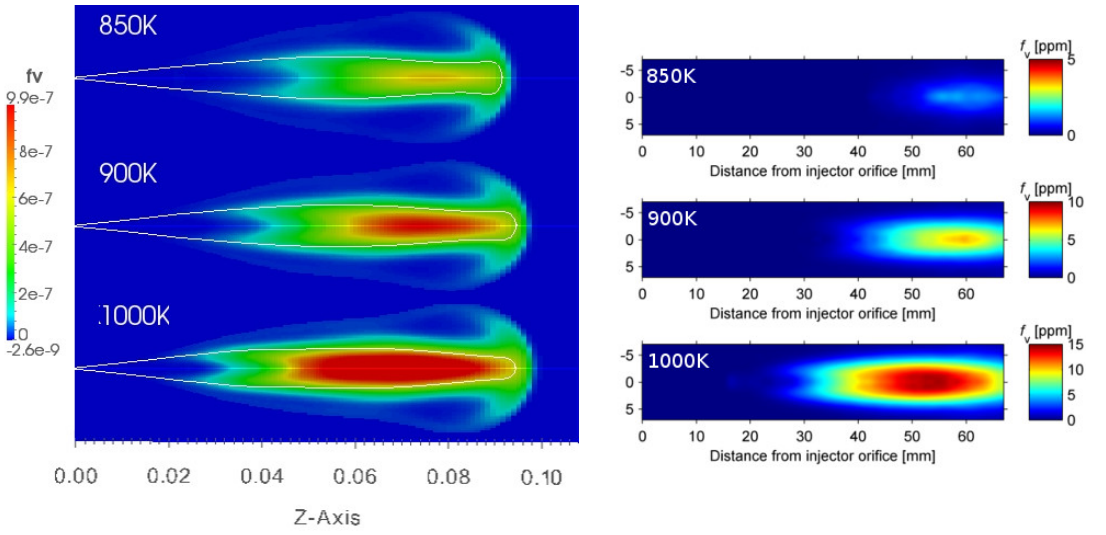

Figure 6.51. Soot volume fraction computed (a) with the model of Lindstedt and measured (b) by [69] at different ambient temperatures.

6.3.3 Validation of soot models: Lindstedt

Influence of ambient temperature

As already observed for the simulations with only one flamelet, Lindstedt model shows a nucleation more accentuated. No differences are detected in term of particle number density fields comparing with the model of Moss, although the peak predicted with the model of Lindstedt is slightly higher (5e+17 vs. 2e+17 for Moss). At the same time Lindstedt model computes a soot mass yield much lower. Lindstedt model tends to underestimate the amount of soot in the jet: beyond the absolute values, what is more important to note is the correct trend of variation of f_v and soot mass with the temperature changes: fig. 6.51 clearly shows this aspect and fig. 6.52 presents the f_v axial profiles normalised with the peak value in reference conditions, for the two models compared with the experimental ones.

There is, again, a marked overall improvement compared to simulations with a single flamelet: now axial location of on-set and peak of f_v are in better agreement with experimental trend. Furthermore, the variations with temperature are more amplified, although they are still lower than those experimental, especially for the case at low temperature. It is likely that there is not a single reason for this behaviour, and it is difficult to separate the effects associated with the computation of the combustion chemistry from those due only to the soot model. Normalized variations are very similar for the two soot models, even if Moss model gets a slightly better result for the case at 1000 K. The similarity in the patterns suggests that both models capture the soot processes in a similar way, despite the differences in the modelling of these. They seem to overestimate the axial length of sooting region and the position of appearance and peak of f_v, particularly Lindstedt. This could be due, as already noted, to a bit limited reactivity of surface growth and oxidation models.

Such observations are reflected in the results of the total soot mass, which are reported in tab. 6.21 and in fig. 6.53. Trend of variations with temperature changes is

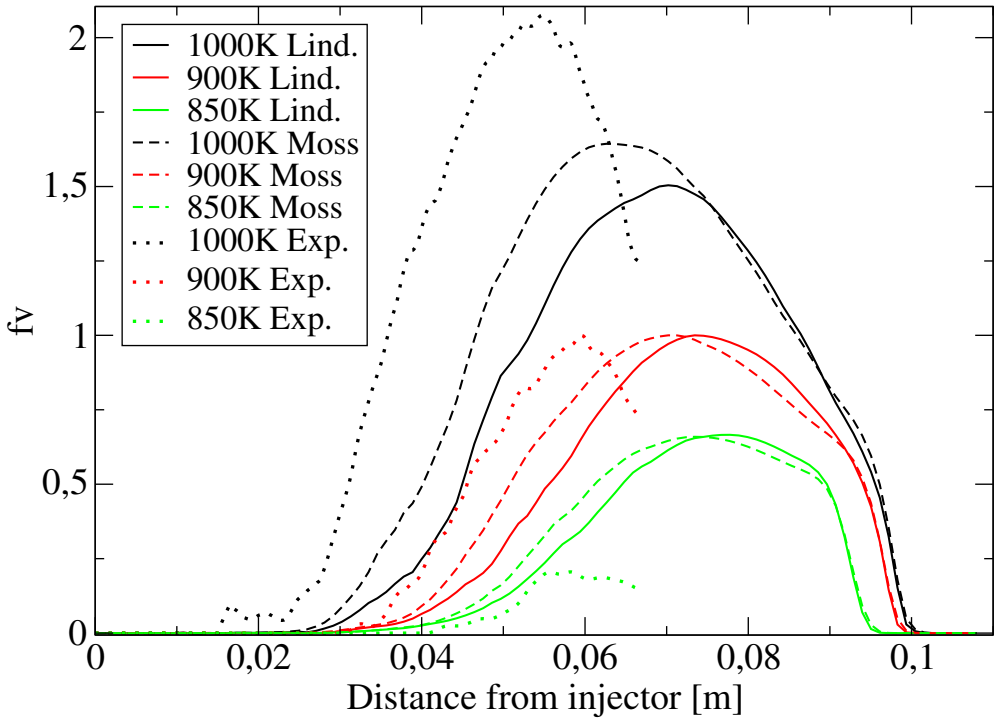

Figure 6.52. Axial f_v computed with multiple RIF and Lindstedt and Moss models for different ambient temperatures. Experimental trends (dot lines) are reported for comparison.

Table 6.21. Soot data for different ambient temperatures computed with Lindstedt and multiple RIF models. Normalized quasi-steady soot values are reported in brackets.

	Exp. soot on-set time [ms]	Comp. soot on-set time [ms]	Exp. quasi-steady soot value [µg]	Comp. quasi-steady soot value [µg]
850 K	1.14	1.6	2(0.143)	3.9 (0.66)
900 K	0.73	1.2	14 (1)	5.9 (1)
1000 K	0.47	0.95	42 (3)	8.6 (1.45)

correct and are aligned with those of Moss. They are quite overestimated, especially for the case at 1000 K. Lindstedt model tends to provide a worst estimate of the soot on-set time doing a direct comparison with experimental detection, but, given the overestimation in the ignition delays, it describes the timing of the soot kinetics slightly better.

Influence of oxygen concentration

Sooting regions are more extend both axially and radially and shifted downstream with decreasing oxygen concentration. Maximum of n_{soot}, in turn, decreases, showing an increased nucleation process. More significant is the analysis of soot volume fraction results since it is possible compare them to experimental ones: as usual, distributions in physical domain of f_v and its axial normalised trends are reported in fig. 6.54 and fig. 6.55 respectively.

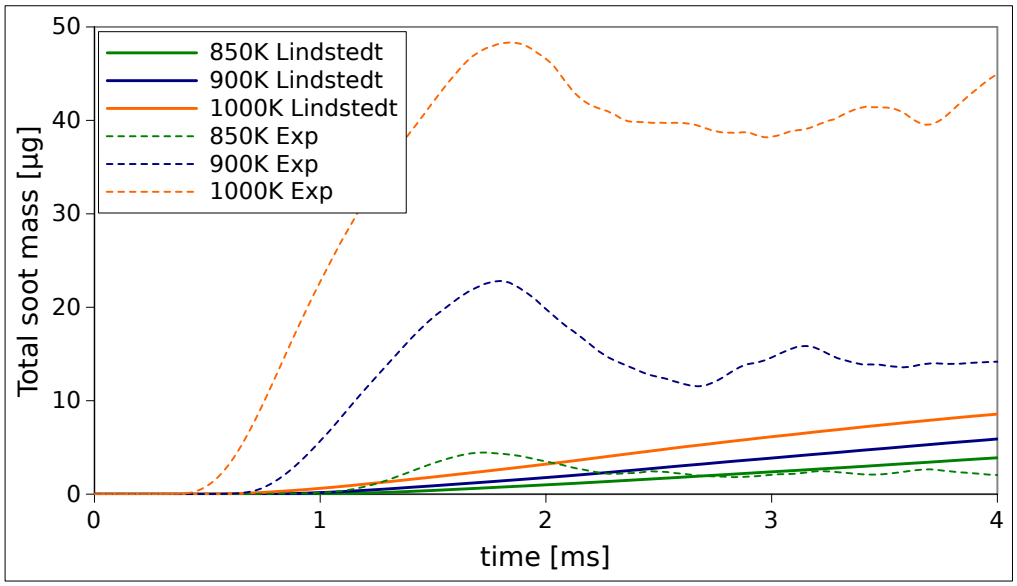

(a) Absolute

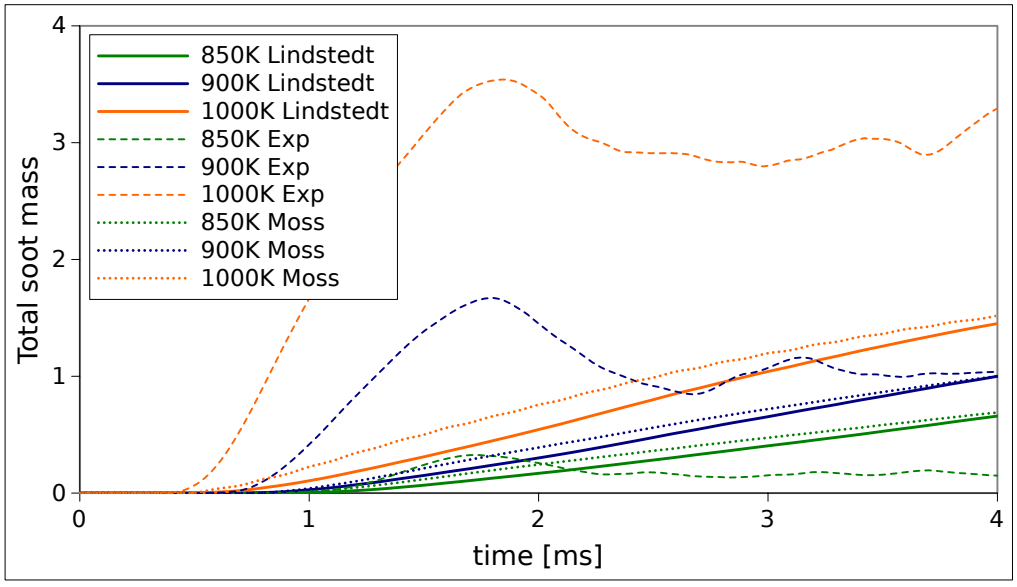

(b) Normalized

Figure 6.53. Comparison of total soot mass computed (full lines) with the model of Lindstedt with the experimental values (dashed lines) taken from [69] for different ambient temperatures.

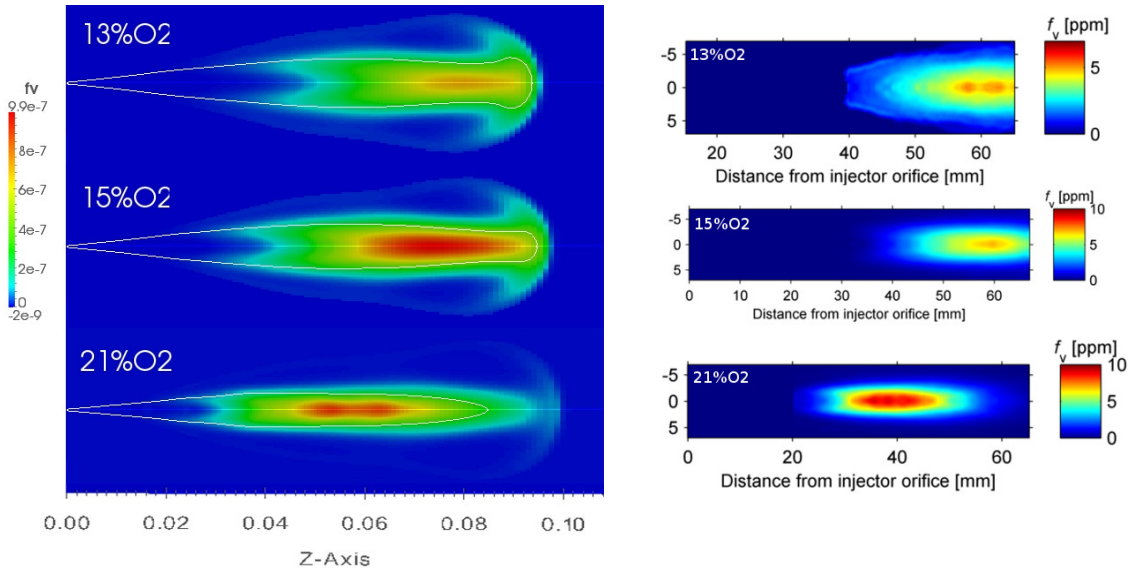

(a) (b)

Figure 6.54. Soot volume fraction computed (a) with the model of Lindstedt and measured (b) by [69] at different oxygen concentrations.

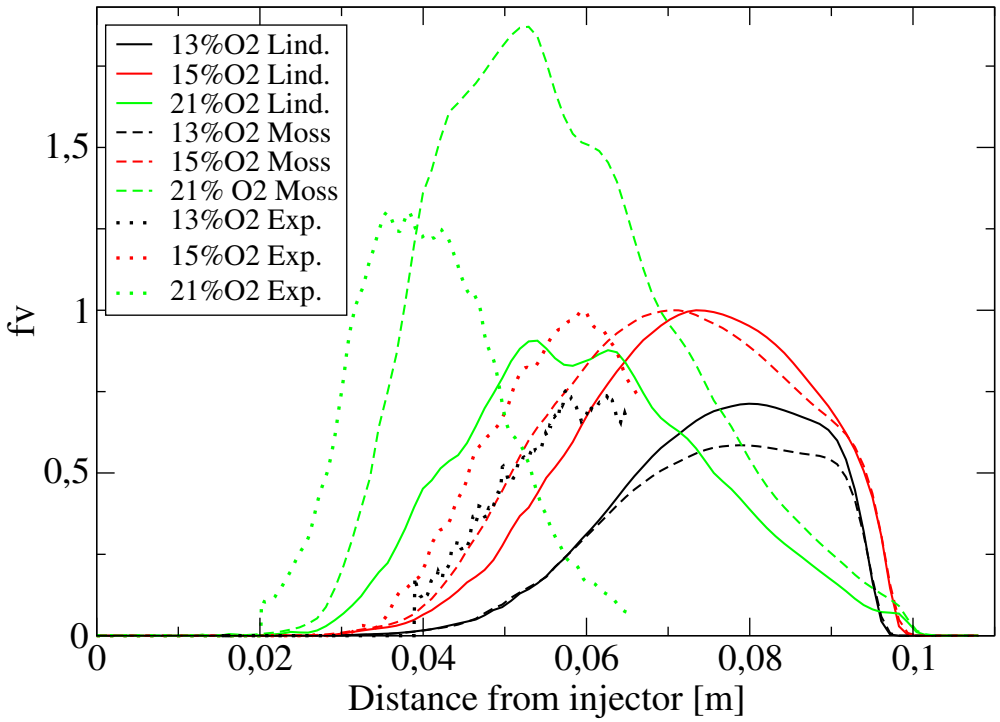

Figure 6.55. Axial f_v computed with multiple RIF and the Lindstedt and Moss models for different oxygen concentrations. Experimental trends (dot lines) are reported for comparison.

The first important observation is that, in this case, Lindstedt model, does not provide the correct variation of f_v changing oxygen concentration from 15% to 21%: peak value, instead of growing, slightly decreases. This result is completely different from that of Moss, which overestimates the normalised increment: a reasonable justification is that now, with a more correct computation of the flame, and so smaller regions for soot to nucleate and grow, and, on the other hand, with more oxygen available in this condition, the oxygen contribution on soot oxidation seems to become excessive and it does not allow Lindstedt model to offer an adequate response with the increase of the amount of oxygen, at least as regards the distribution of f_v. On the other hand, the trend of the peak position is correct and it is interesting to note, however, that Lindstedt model, unlike Moss, succeeds to simulate the double peak shown by the axial f_v profile for 21% O_2 condition.

Observing the results in tab. 6.22 and in fig. 6.56, it can be seen how the trend of variation of the total soot mass produced is correct. The overestimation in the decrease of global mass with increasing the ambient oxygen concentration can be interpreted in the light of the above considerations.

Table 6.22. Soot data for different oxygen concentrations computed with Lindstedt and multiple RIF models. Normalized quasi-steady soot values are reported in brackets.

	Exp. soot on-set time [ms]	Comp. soot on-set time [ms]	Exp. quasi-steady soot value [µg]	Comp. quasi-steady soot value [µg]
13%	0.97	1.6	10 (0.71)	5.07 (0.86)
15%	0.73	1.2	14 (1)	5.9 (1)
21%	0.36	0.9	11 (0.786)	2.6 (0.44)

Influence of ambient density

Also for this last case analysed, comparisons between distributions of f_v in physical domain computed and experimental are reported in fig. 6.57: they match with a good approximation experimental results, in terms of both position and of absolute values. The significant aspect is this correct trend, even if the magnitude of variation is rather underestimated: in fact, by changing the density from 14.8 kg/m^3 to 30 kg/m^3, the peak of the experimental f_v varies by an order of magnitude (about 0.6 ppm vs. 6 ppm). The computed one, on the contrary, differs by about 3 ppm (9 ppm versus 2.5 ppm).

Normalized trends of axial f_v for the models of Lindstedt and Moss are reported in fig. 6.58. No significant differences are detected, although Moss model provides a greater variation than Lindstedt one.

These results related to soot volume fraction are reflected in total soot mass trends reported in fig. 6.59. Lindstedt model captures properly the variation with density and, as before, absolute values are considerably lower than those of Moss and likely closer to the effective ones. This confirms that the incorrect trend obtained with one flamelet is due to the faults in the computation of the flames. Normalized

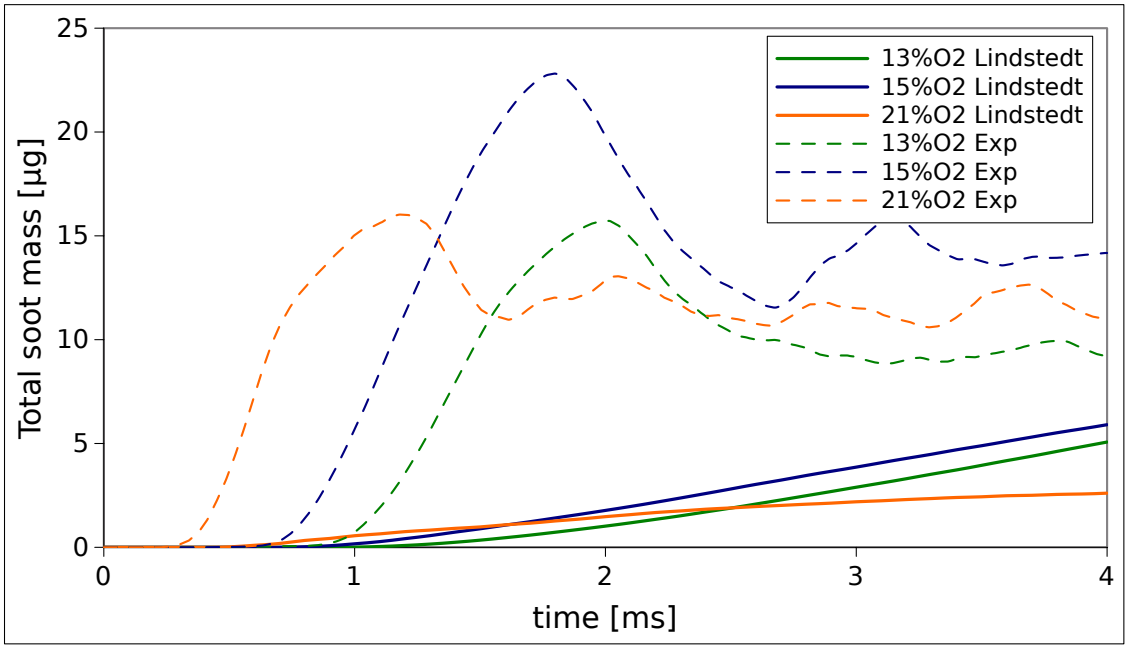

(a) Absolute

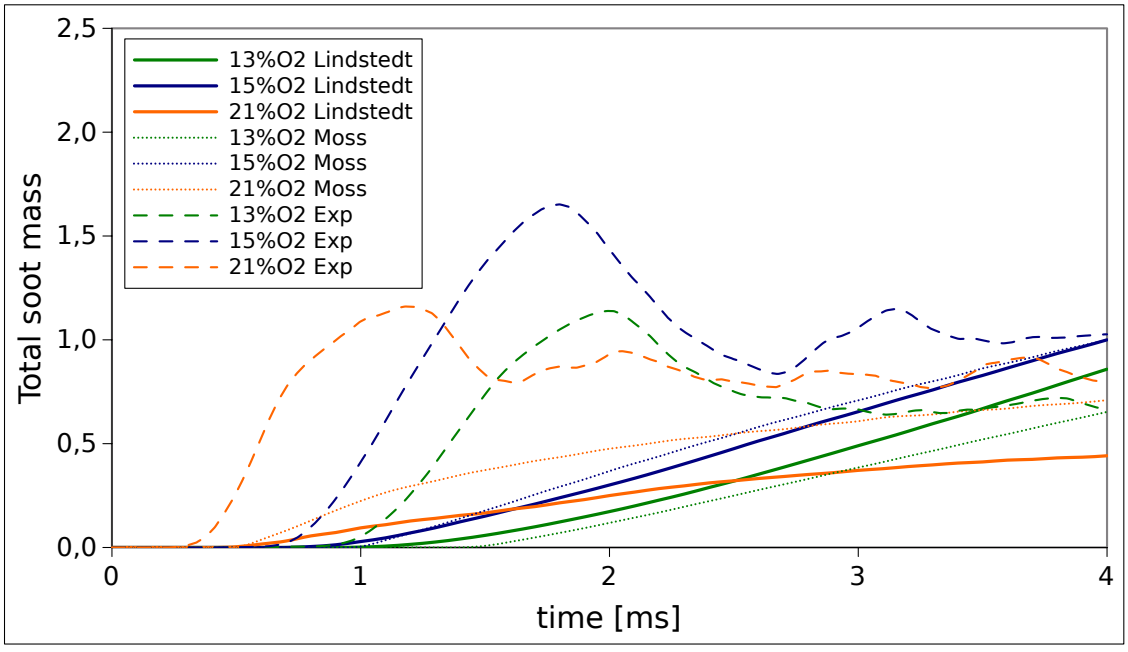

(b) Normalized

Figure 6.56. Comparison of total soot mass computed (full lines) with the model of Lindstedt with the experimental values (dashed lines) taken from [69] for different oxygen concentrations.

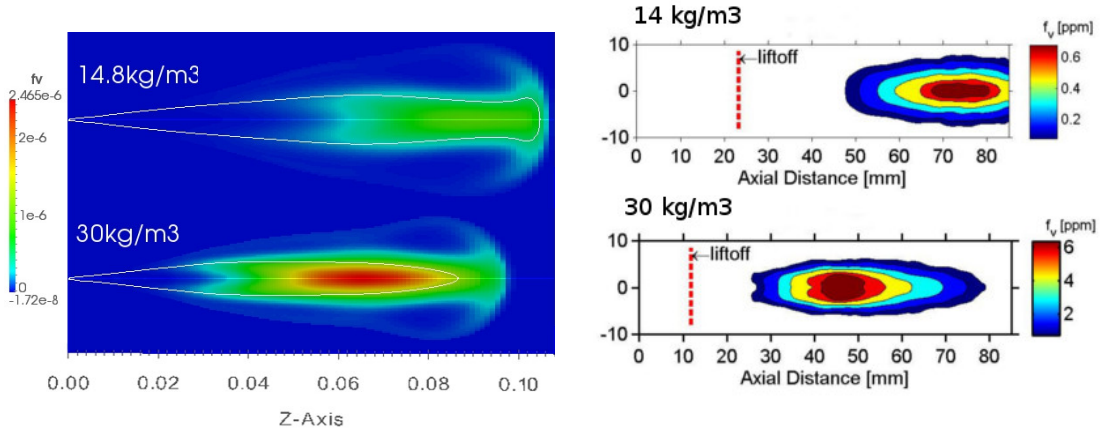

(a) (b)

Figure 6.57. Soot volume fraction computed (a) with Lindstedt model and measured (b) by [69] at different ambient densities.

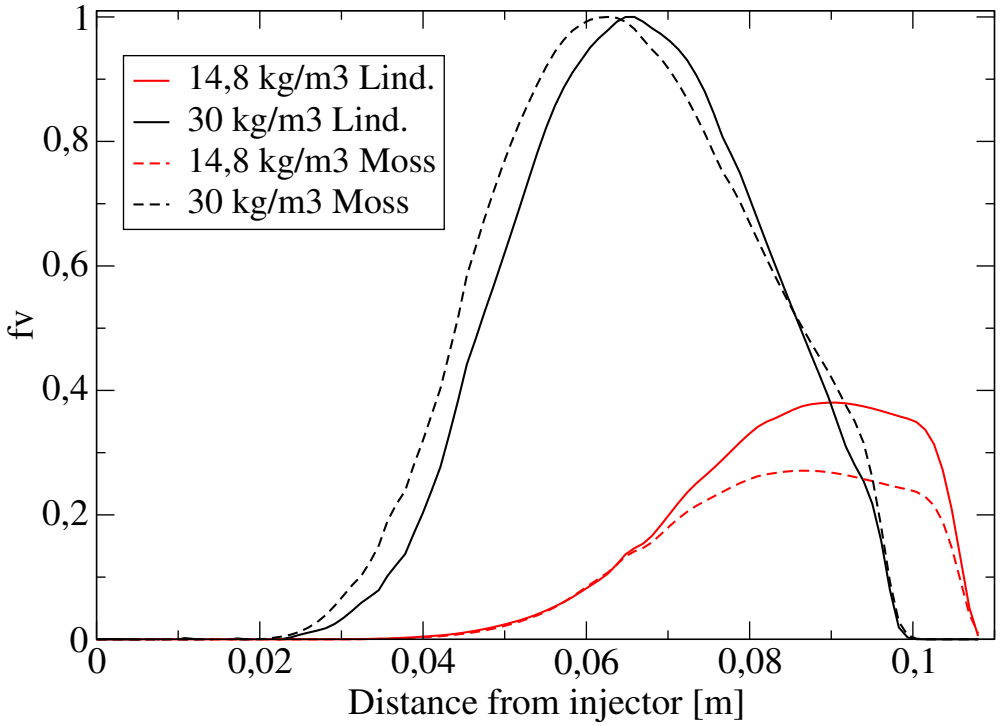

Figure 6.58. Axial f_v computed with multiple RIF and Lindstedt and Moss models for different ambient densities.

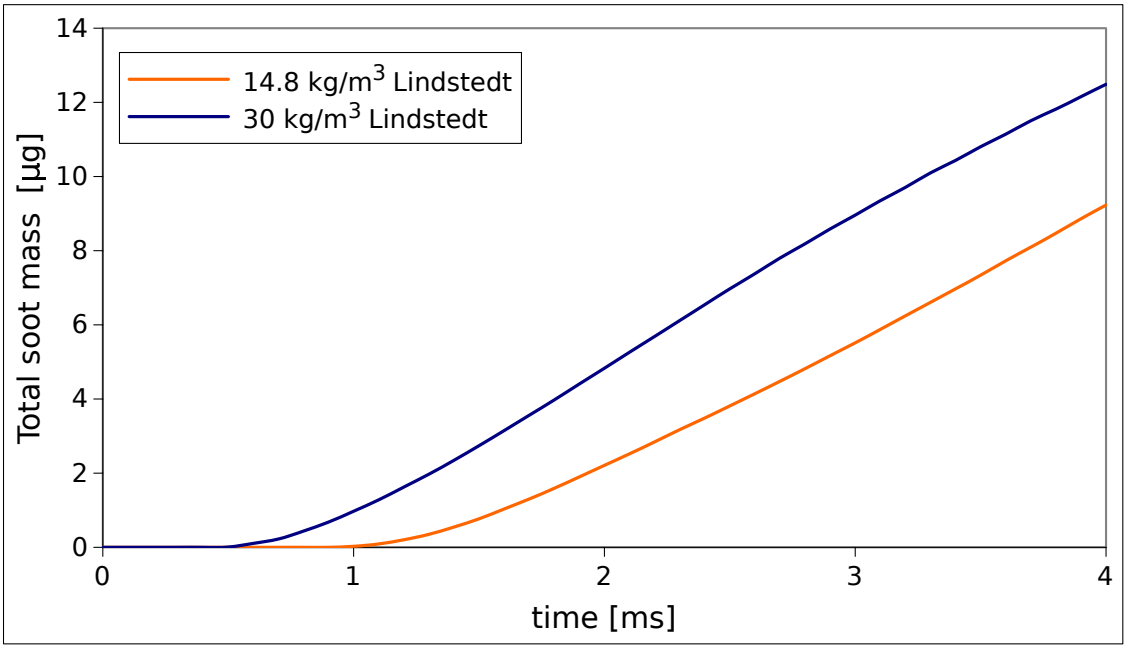

(a) Absolute

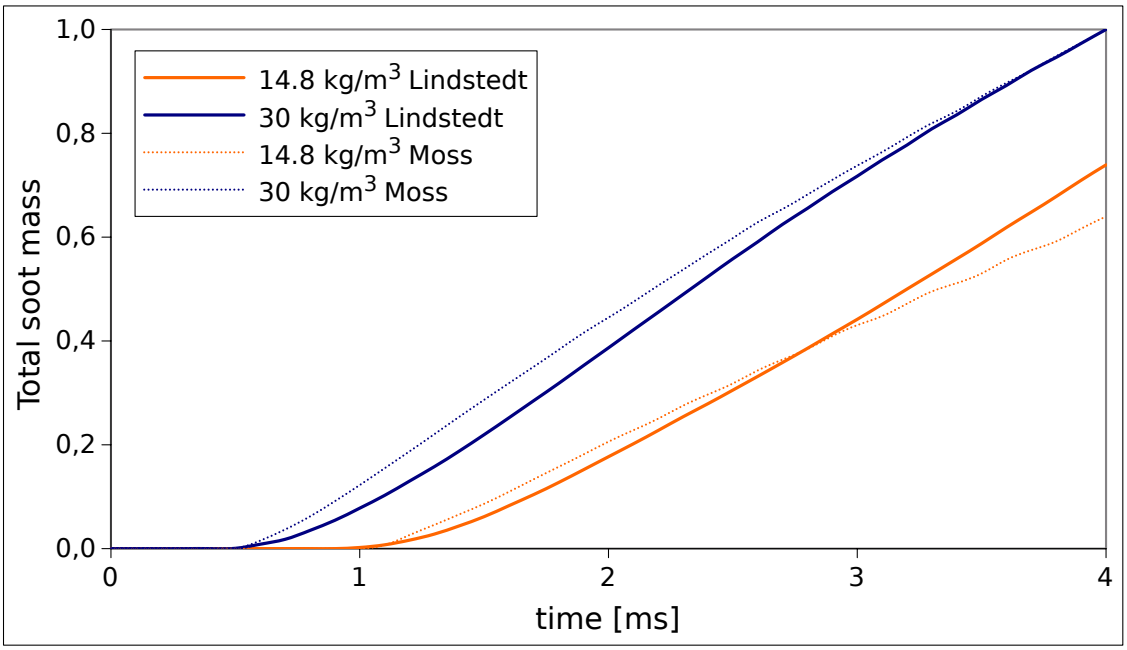

(b) Normalized

Figure 6.59. Comparison of total soot mass computed (full lines) with Lindstedt and Moss (dashed lines) models for different ambient densities.

variation provides by Lindstedt is smaller, and, seen previous results, it is believed that Moss gives a more correct trend in respect of real soot mass.

6.4 Conclusions of the constant volume vessel validations

In the end of the validation of the soot models in the constant volume vessel, the following conclusion can be drawn:

- the preliminary validation at reference conditions shows that the model of Wen is not able to correctly predict the soot trend, due to the direct dependency of the mass growth to the surface which does not seem adequate for the conditions simulated in this work. On the contrary, both the models of Moss and Lindstedt point out a correct soot trend over time.
- The validation with the single flamelet approach carried out for the model of Moss and Lindstedt shows that they provide correct responses to ambient conditions variations, even though the actual flame structure is not correctly computed. In particular, the model of Moss has shown variations with ambient conditions in better agreement with measured detections and, contrary to the model of Lindstedt, a correct axial f_v peak with all oxygen concentrations.
- Using a multiple flamelet approach, which in turn is able to better represent the physical flame structure, particularly the fundamental lift-off length, soot results provided by the models of Moss and Lindstedt are generally in good agreement with experimental data. In detail, improvements are both in quantitative term and in the location of soot field inside the jet. This proves that an accurate modeling of flame propagation process provides the basis of a good soot prediction.

In conclusion, a multiple RIF combined with the model of Moss provides the best and encouraging results at the simulated conditions and for this reason it will be applied to IC engine simulations in the next chapter.

Chapter 7

Results and discussion: engine validation

Complex injection strategies play a fundamental role to reduce pollutant emissions and combustion noise and to increase efficiency of DI Diesel engines. In recent decades, the advent of high pressure common-rail systems with the electronically controlled fuel injection and the introduction of piezo-actuated injectors, have allowed the adoption of multiple injections and profiles of injection laws designed to control the amount of fuel burning during the premixed phase, e.g. ramp or boot injections [89]. Within this context, it is therefore important to assess the ability of spray, combustion and pollutant formation CFD models to give adequate results for such combustion modes.

In this chapter soot model of Moss with single RIF approach is tested on an engine case with different amount of fuel delivered during the post-injection event. Lindstedt model has not been tested in this condition because Moss has given slightly better results in constant volume vessel.

First, experimental and numerical characterizations of the case are presented, focusing on differences with the simulations in the SANDIA bomb and then results are discussed.

7.1 Experimental set-up

A single cylinder research engine derived from a 2-L series PSA engine is simulated. Its mean features are reported in tab. 7.1

Table 7.1. Engine characteristics

Bore [mm]	Stroke [mm]	CR	swirl number [AVL]	injection system	IVC cad ATDC	EVO cad ATCD
85	88	15.5	1.24	Continental common rail	-150	100

A large amount of experimental data in terms of in-cylinder pressure, pollutant

emissions, fuel consumption and other parameters have been acquired for different operating points by the research group of Continental Automotive GmbH. Exhaust gases (HC, CO, CO_2, NOx) were measured with a Horiba MEXA 8420, oxygen concentration by an ETAS Lambda-meter LA4 and PM emissions with an AVL 415S smoke-meter while in-cylinder pressure was detected with a Kistler 6043ASP pressure transducer [89]. To assess the ability of Moss soot model to provide the correct trend for soot discharged from engine, varying the amount of fuel in the post-injection, an operating point with different injection strategies is analysed: the rated power point (RPP) is characterized by full engine load, no external EGR and an engine speed of 4000 rpm. In the present work, the different conditions examined are characterized by a constant injected fuel mass per cycle (about 47 mg per stroke), but a progressively decreasing mass of fuel in the main injection and an accordingly increasing injected one in post-injection. The base case, named 2380, is characterized by the single main injection, and by an indicated mean effective pressure (IMEP) equal to 16.5 bar. Injection timing and SOI of the post-injection were varied in order to obtain the same engine load for all cases. Fuel amount, SOI and the end of injection, EOI, of each injection event for the different cases are listed in tab. 7.2

Table 7.2. Characteristics of injections for RPP points.

Point	post injection			main injection		
	mass injected [mg]	SOI cad ATDC	EOI cad ATDC	mass injected [mg]	SOI cad ATDC	EOI cad ATDC
2380	0	–	–	47.3	-11.8	20.4
2377	1	27.2	30.6	46	-11.3	20.1
2378	3	27.2	32.7	44.1	-11.4	18.8
2374	5	25.5	32.5	42.5	-11.3	18.2
2375	7	24.7	32.9	40.6	-11.5	17.5
2376	9	24.4	34	38.7	-11.6	15.8

Henceforth, for greater clarity in the images and data reported, different operating points will be indicated with the corresponding mass of fuel injected in the post-injection.

7.2 Mesh set-up

For each engine simulations, a sector of the combustion chamber with an angle of 45° has been considered, as the injector consists of eight equally spaced orifices. The mesh consists of 16380 hexahedral or polyhedral cells at TDC and 72270 at IVC. It is spray-oriented, i.e. the grid direction is arranged in such a way that the spray axis is as perpendicular as possible to the cells. In fact, as referred by Lucchini et al. in [70], the relative orientation of the grid to the spray axis influences the exchanges of mass, momentum and energy between the spray liquid phase and the gas phase through the number of the nearest nodes and the consequential gas phase mass involved. The engine mesh at TDC is shown in fig. 7.1.

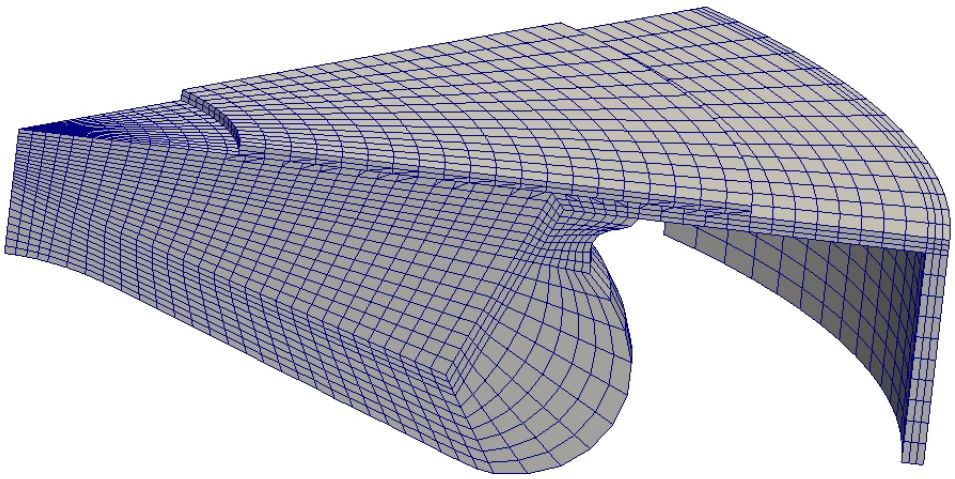

Figure 7.1. Computational engine mesh at TDC

An automatic mesh generation utility developed by the ICE group of Politecnico di Milano [90] has been used in this work to create the spray-oriented mesh of the engine combustion chamber. The utility takes as input data the STL profile of half section of the combustion chamber, the injector position, the injection angle and several mesh parameters such as number of cells and grading in different mesh regions, dimensions of the compensation volumes to match the actual compression ratio, etc. A Python program automatically recognizes the points of the profile and generate a 2D mesh which is then extruded to obtain a 3D wedge mesh. The utility also allows manual modifications of main points, in order to change eventual aspects of the mesh automatically generated and make it more suitable for a better simulation.

7.3 Simulation set-up

Simulations are performed starting from the IVC up to the EVO. It is essential, first of all, to identify the appropriate thermodynamic conditions and the chemical composition of the mass in cylinder at the closure of the intake valves, because no experimental data related to chemical species concentration and temperature are available at IVC. Thus, a one-dimensional thermodynamic model developed by the ICE group of Politecnico di Milano is employed to determine such initial conditions, by imposing an internal EGR, the portion of exhaust gases which remains in the cylinder after the closure of exhaust valves, equal to 7%. This value was derived by previous analyses on this engine at the same operating point conducted with a similar research code, GASDYN [91, 92]. Pressure and temperature are set so that the pressure curve calculated by the thermodynamic model are as close as possible to the experimental ones. Determined initial conditions are reported in tab. 7.3 and 7.4, in which also temperature of liner, cylinder head and piston selected are listed. These values, in the absence of experimental measurements, are chosen on the basis of experience: they are typical values for this type of engines.

Table 7.3. Initial conditions (IVC) for RPP simulations: pressure and temperature.

pressure [bar]	temperature [K]	liner temp. [K]	cyl. head temp. [K]	piston temp. [K]
2.855	441.5	450	500	550

Table 7.4. Initial conditions (IVC) for RPP simulations: chemical composition (mass fractions).

O_2	N_2	CO_2	H_2O
22.15%	77.46%	0.98%	0.41%

RIF combustion and Moss soot models are employed for the simulations: a single flamelet is used for each injection event, taking into account only the corresponding injected mass. Despite the previous results obtained in the constant volume chamber, the choice to use only one flamelet is basically motivated by the fact that, in conditions similar to those of the engine simulated in this work, the flame does not seem to present a significant lift-off. The result that would be achieved with more flamelets therefore, would not be very different, with, on the other hand, a much higher computational cost.

Simulated fuel is n-dodecane, because not only it has a cetane number similar to that of Diesel fuel, but also because previous analysis [89, 93] have shown that measured gaseous species concentrations derive from a Diesel fuel with an H/C ratio very close to the one of n-dodecane. Therefore, the same kinetic mechanism used for SANDIA vessel simulations is employed here and in general the same settings of constants and tolerances of the different sub-models indicated previously, were used. Nevertheless, as it will be explained in the next section, the preliminary simulations of the reference operating point (RPP 2380), necessary to correctly set the case, have shown an underestimation of pressure peak and pressure during the expansion stroke. It is believed that this drawback can be attributed to the generation of an excessively rich mixture during the injection, i.e. to a not correct simulation of the spray. This produces a high amount of CO which then is not completely oxidized to CO_2. Therefore, a more in depth investigation addressed to increase the mixing of the injected fuel with charge air was carried out. A brief parametric analysis have led to a variation of some constant values, related to spray models and mixture fraction Schmidt numbers used in Z (Sc_Z and $Sc_{Z''^2}$) and in the flamelet markers transport equations (Sc_t). Final selected values are reported in tab. 7.5.

Table 7.5. Selected values of Schmidt numbers and spray constants for RPP simulations.

Sc_Z	$Sc_{Z''^2}$	Sc_t	B_1	C_τ	C_{RT}	C_{BU}
0.7	0.7	0.7	23.5	0.2	0.2	25

The reduction of Schmidt numbers should provide a greater diffusivity of mixture fraction, while, for what concerns the spray constants, they should be adjusted to

match the experimental data of spray angle and penetration, atomization length and influence of turbulence and cavitation phenomena inside the nozzle on secondary break-up. Unfortunately, no such informations are available and standard values derived from literature have been selected as initial set-up. Therefore, these values have been varied parametrically, trying to achieve a better performance in terms of spray simulation with a less rich combustion and a slower amount of CO generated. Nevertheless, not huge changes were made to the initial values and the results have been a little improved although during the last phase of expansion stroke an underestimation of pressure and an excessive concentration of CO are still observed. This problem should be further investigated and improved spray set-up can be found.

7.4 Results and discussion

The first operating point simulated is the RPP 2380, that is the one with only main injection and no post-injection. In fig. 7.2 computed in-cylinder pressure and rate of heat release (ROHR) respectively are compared with the experimental ones. Pressure and ROHR traces for the other operating points will not be reported because they are very similar to the one of the reference case and the same considerations can be made. Computed and experimental pressures match quite well but, as mentioned above, there is an underestimation of computed pressure during the last part of expansion stroke. It is possible to see the same trends also for ROHR traces: in the simulation a small amount of heat seems not be released by combustion. In fact, the trend of CO, after an initial peak in correspondence of the EOI, begins to decrease due to its oxidation to CO_2 but at the EVO the molar concentration is still too high compared to the experimentally measured: about 1.5% against 0.02%. Certainly, the extreme conditions simulated (full load and high speed engine) exacerbate this problem with less air and less time available for the oxidation of the fuel and soot. The ROHR shows also a small overestimation of the ignition delay, as already observed for the SANDIA vessel, with a higher portion of fuel burned during the premixed combustion.

For the reference case in fig. 7.3 temperature distribution at 15° ATDC and CO distributions at 15° and 40° ATDC are shown. The spread of the cone spray appears to be too low and therefore the jet is not able to entrain sufficient amount of air mass to achieve the values of appropriate equivalence ratio. This leads to the generation of a fuel rich area, first into the jet and then, at the end of injection, in the piston bowl, with high concentrations of CO, which is then only partially oxidized during the second part of the expansion. Several other factors, in addition to the already mentioned difficulties in setting the spray model, which seems to be still the main cause, may contribute to this result. Certainly the reported uncertainty of initial and boundary conditions and of the effective duration of injection events contribute, but perhaps the mesh not sufficiently fine and the kinetic mechanism not reactive enough for engine conditions, may play a role. These are all aspects that would require more in-depth investigations, possibly in future works.

Despite this problem in combustion computation, it has been decided to perform anyway the simulations for other operating points and to analyse the results concerning the soot, in order to draw some further considerations.

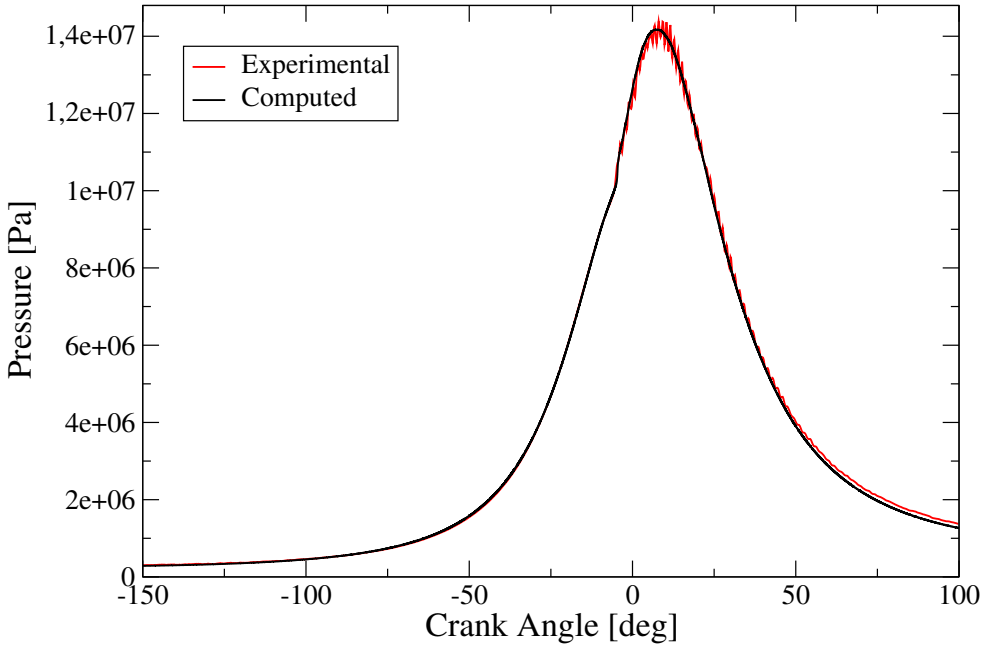

(a) Pressure

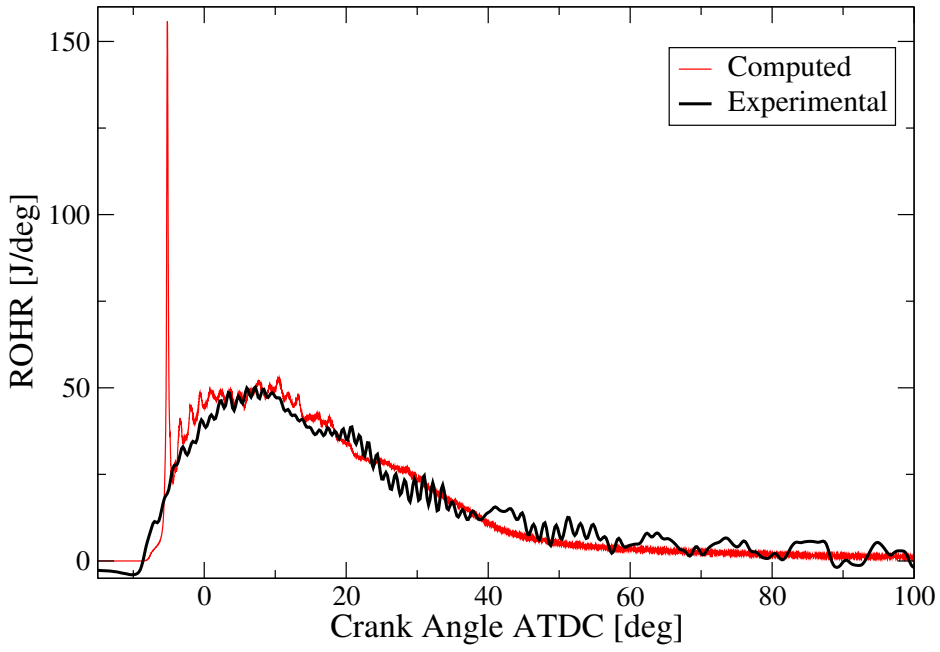

(b) ROHR

Figure 7.2. Pressure and ROHR for engine case with only main injection.

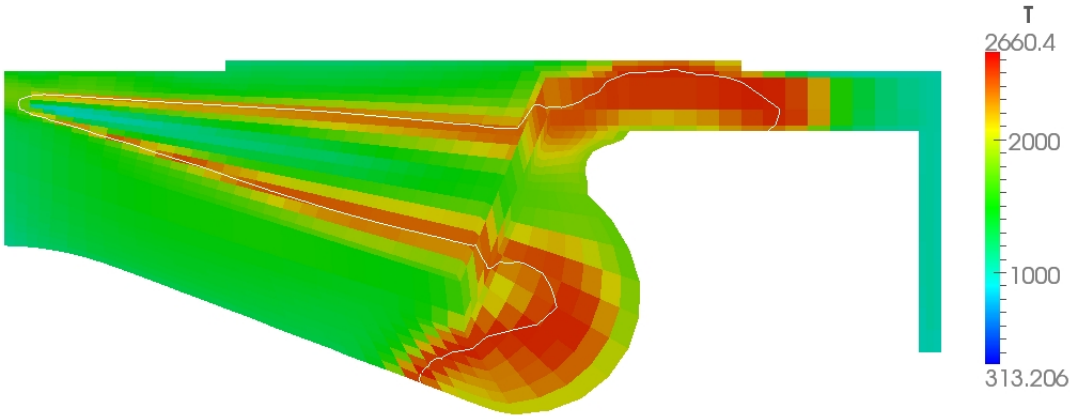

(a) Temperature at 15°

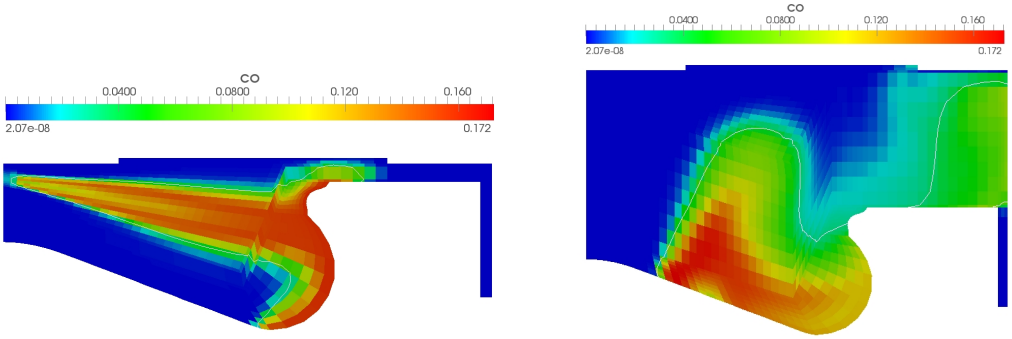

(b) CO at 15°

(c) CO at 40°

Figure 7.3. Temperature field at 15° and CO fields at 15° and 40° for the engine case with only main injection.

In fig. 7.4 normalized emission trends of soot volume fraction, experimental and computed, as function of the amount of fuel in the post-injection, are reported. Experimental data show that there is an optimum value of fuel mass in post-injection, between 3 mg and 5 mg, in terms of minimization of soot yield. Computed trend is correct only for the first amounts of fuel injected (up to about 5 mg): with increasing the amount of fuel transferred from the main to the post, soot emissions decrease. Nevertheless, exceeded 5 mg in post-injection, experimental soot begins to grow while the computed one continues to decrease. Data of the in-cylinder evolution of soot was not detected, but computed ones for different operating points can be compared.

In fig. 7.5 mean soot volume fraction as function of crank angle degrees is shown, for clearness, only for the reference case and for the operating points with 3 mg and 9 mg of fuel in post-injection. Since the SOI for all cases is similar, the on-set time of soot is about the same, but with increasing the mass of fuel in main injection, the growth of soot continues for more time, leading to a higher quantity produced at the end of this first injection event. Immediately after, the amount of soot decreases very rapidly for the effect of oxidation at high temperature but when post-injection

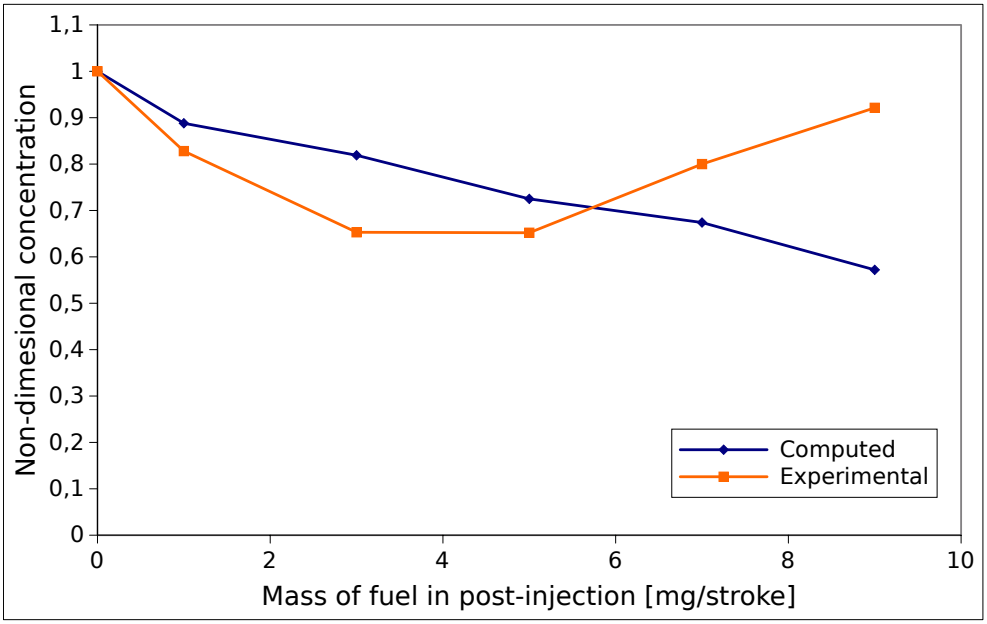

Figure 7.4. Non-dimensional concentrations of soot for RPP operating points.

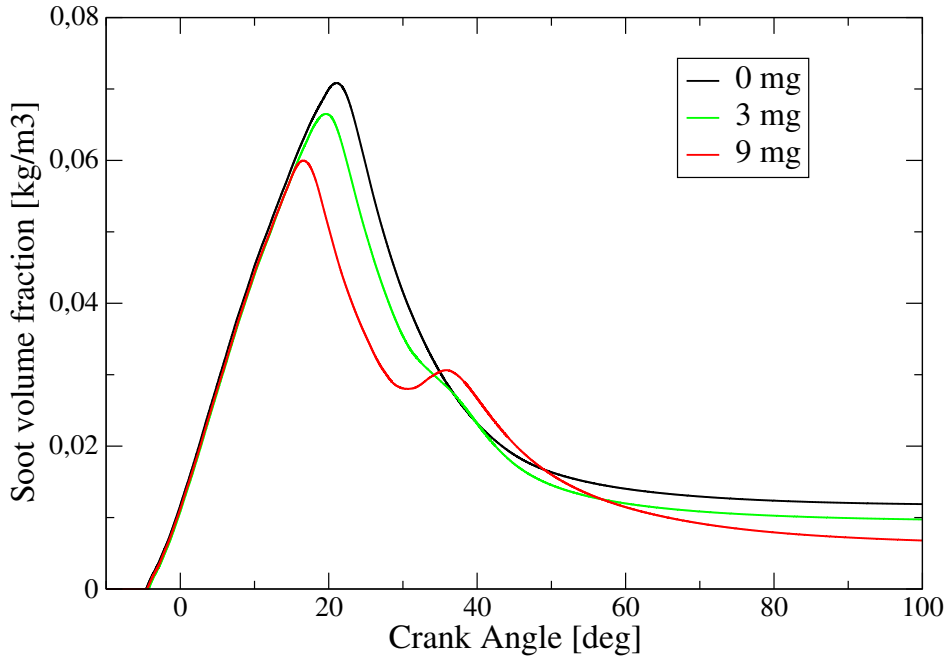

Figure 7.5. f_v in-cylinder evolutions for 0, 3 and 9 mg in post-injection cases.

occurs, additional soot is formed. With small quantities of fuel in post-injection, for example 3 mg or 5 mg, the new soot mass produced is less than the one which is meanwhile oxidised and global soot mass continues to decrease. When, however, the share of fuel due to the post-injection increases further, the net result is the opposite: locally a new smaller rise of soot mass in-cylinder occurs and it reaches higher values than the ones of the cases with no post-injection or a smaller amount of fuel in it. Computed trends show that, on the other hand, after this second peak, the rate of soot oxidation is gradually higher with the increase of fuel amount in the post-injection, due to the greater temperature rise. Given the experimental measurements and results of previous works [89, 93], it can be deduced that in the actual case, when the mass in post-injection exceeds 3-5 mg, the effect of further soot mass formed overcompensates the increase in the oxidation rate: the net result is that final soot emissions return to grow. Computed trends of the present work show that, on the contrary, this trade-off is resolved for all cases in favour of a lower soot mass at the EVO.

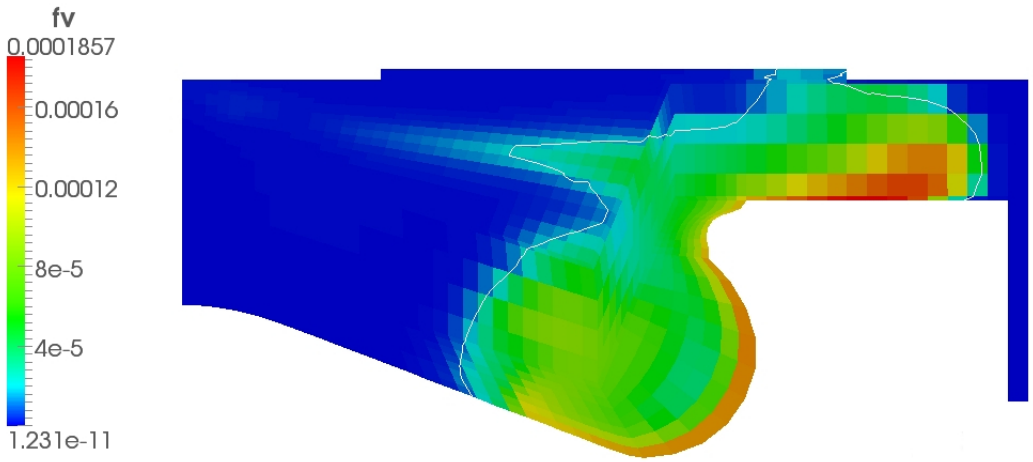

(a) only main

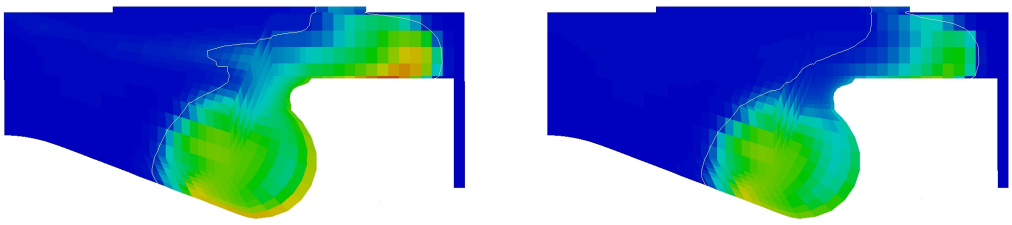

(b) 3 mg

(c) 9 mg

Figure 7.6. f_v fields for the cases with 0, 3 and 9 mg of fuel in post-injection at 25°.

Fig 7.6 shows the computed distributions of soot volume fraction for the aforementioned cases at 25° ATDC, when all three main injections have just finished. With decreasing the mass injected, a reduction in soot concentration can be observed. Also lower values of mixture fraction and CO and higher temperatures, due to the

less rich combustion, are computed. As seen before, main injection generates a zone in the piston bowl the fuel richer the greater is the amount of mass injected, which tends to be slowly oxidised.

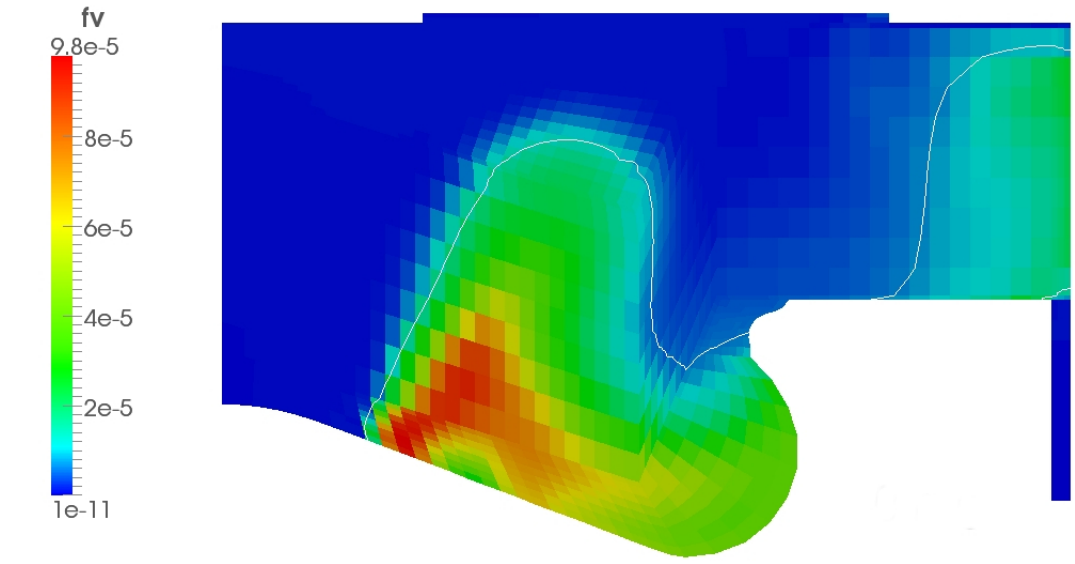

(a) only main

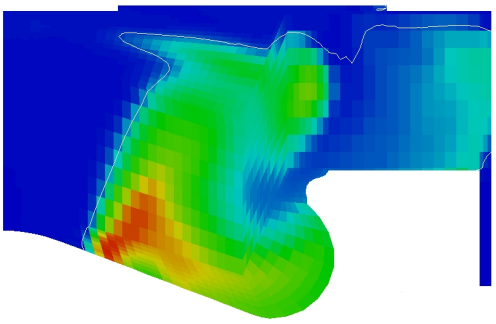

(b) 3 mg

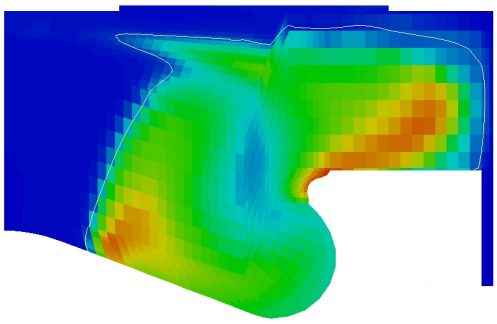

(c) 9 mg

Figure 7.7. f_v fields for the cases with 0, 3 and 9 mg of fuel in post-injection at 40°.

In fact, if soot distributions at 40° ATDC are reported in fig.7.7, it is possible to see in the bowl the soot formed before during the main and, for the two cases with post-injection, also the new soot formed closer to the cylinder head and in the squish zone. Properly, the concentration of the more recent soot, increases with the amount of fuel in the post-injection and for the case with 9 mg, it is even higher than that produced by the main injection. Nevertheless, due likely to the lower mass injected, the area affected by the second spray, is less rich than the previous one, leading to its more easy oxidation by the surrounding air. Moreover, the second injection event and the leaner mixture in the bowl cause a higher and more homogeneous temperature, which allow an enhancement in soot oxidation. Moreover, not having available experimental data related to the spray, the same spray model set-up has been used to simulate main and post-injection. However, during the post-injection, the injector needle is not completely lifted and it is very likely that the configuration of the spray is actually different from that of the main-injection.

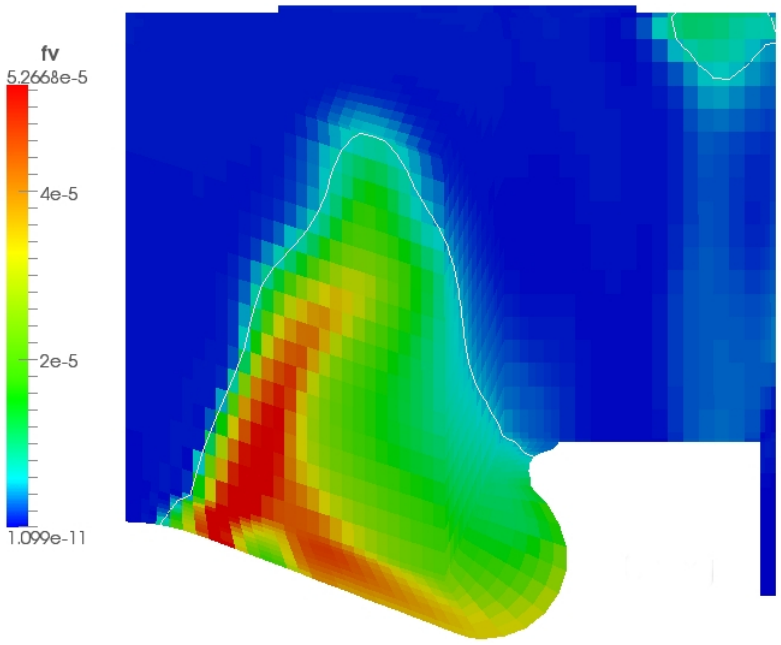

(a) only main

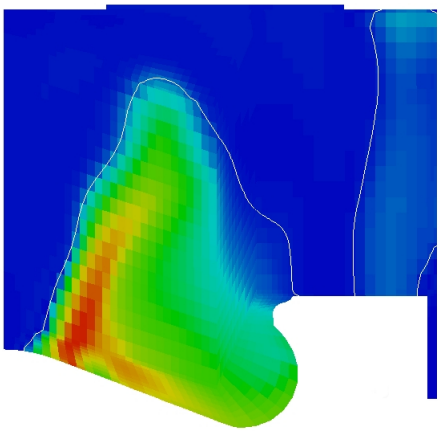

(b) 3 mg

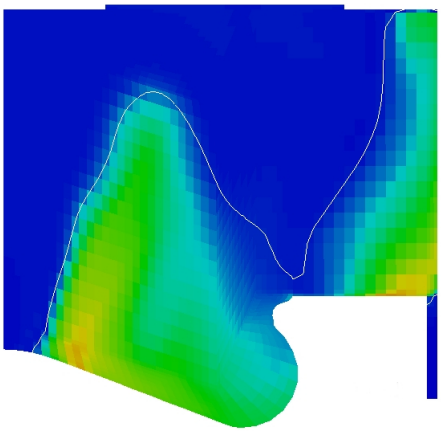

(c) 9 mg

Figure 7.8. f_v fields for the cases with 0, 3 and 9 mg of fuel in post-injection at 60°.

Indeed, in fig. 7.8 soot distributions at 60° ATDC are shown: soot formed during the post-injection has completely disappeared for the operating point with 3 mg, whereas, for the other case, it is still observable, but has undergone a considerable reduction due to oxidation. Finally, therefore, by observing these results, it seems that the erroneous second part of the trend in the soot mass varying the quantity of fuel in post-injection, is attributable to the fact that splitting of injection in two separate events and progressively decreasing the mass in the main injection, tends to make the spray of the latter gradually less rich. In this way, the influence of the problem in combustion computation described before seems to decrease: rich zones in the piston bowl are so more easily oxidized, thanks also to the mixing induced by the flow field caused by the post-injection. It is difficult, as usual, to separate the effects on soot of the spray and combustion modeling from those of the soot model itself. However, it has been seen in the previous chapter that Moss model

tends to underestimate the reduction of soot mass with decreasing temperature. Thus, a possible factor that contributes to such soot results in engine simulations, is an overestimation of the oxidation in the higher temperature regions affected by post-injection and at the same time, its underestimation and an overestimation of the soot mass growth in the lower temperatures zones in the bowl. Certainly, in order to evaluate the correctness of this last consideration, a better combustion computation is required and it must be object of further investigations.

Conclusions

In this work, validation of three semi-empirical soot models, developed by Moss [1], Lindstedt-Leung [2, 3] and Wen [5] and implemented coupled with pre-existing RIF combustion model by the authors in the Lib-ICE, the set of applications and libraries worked out for IC engines by the ICE Group of Politecnico di Milano, has been presented. Validation was basically carried out in a constant volume vessel by comparing the computed results with measurements of SANDIA National Laboratories (SNL) [69] over a wide range of operating conditions. Initially, the three soot models have been tested on a selected reference case with single RIF model. Then a parametric analysis, varying initial vessel temperature, oxygen concentration e density, has been conducted for Moss and Lindstedt models, first with a single RIF approach and later with a multiple flamelet one, the Eulerian Particle flamelet model. Finally, model of Moss was employed to carried out a brief analysis on a research engine with different injection profiles.

Results obtained from different validations performed, lead to the following schematic conclusions:

- the single RIF model does not reproduce the lift-off of Diesel flame e this seems to be the most influential drawback for soot computation. Despite this aspect, for reference conditions, Moss and Lindstedt models provide acceptable time evolutions for distributions of soot volume fraction in physical domain and for total soot mass in the jet, with a growth that gradually decreases as time passes. Wen model, instead, excessively delays the appearance of the soot and, at the same time, shows an uncontrolled growth of soot, in contrast with the experimental trend. Therefore, this model is believed to be inadequate to reproduce soot processes in the simulated conditions of this work. Parametric analysis has been conducted only for the other two models.

- Moss and Lindstedt models in general, even with only one flamelet, provide the correct trends for particle number density, soot volume fraction and total soot mass varying initial ambient conditions. Distributions and peak position of f_v into the jet are not in complete agreement with experimental ones but the absence of lift-off heavily affects the results. The best computation results were found for conditions with variable oxygen concentration: f_v and soot mass variations are in good agreement with the experimental ones. Results obtained varying ambient temperature are rather underestimated. Lindstedt model provides uncorrected soot results at quasi-steady condition for different ambient densities respect to what it was expected from literature. Nevertheless, as confirmed by simulations with multiple flamelets, this results are due to the

wrong computation of flame structure with single RIF.

- Using the Eulerian Particle Flamelet model with 20 flamelets, the structure of the flame, as expected, is more correct and for all different cases simulated, the LOL is predicted with sufficient accuracy. The improvement in soot results is considerable. In reference conditions, Moss model provides time evolutions, distributions in the jet and absolute values for soot volume fraction in very good agreement with experimental data. Even the soot mass computed shows significant improvements, for both absolute values and time trends. Similar considerations can be done for Lindstedt, although distributions in the CFD domain and the on-set soot axial position are slightly less correct than for Moss.

- For both models, with multiple flamelet approach, also the results with variable ambient conditions improve: computed and experimental normalized variations, in general, agree in a better way with respect to single RIF. Moss model provides the correct trends for all tested conditions, although variations with temperature and density, both for f_v and soot mass, are still underestimated while changes in soot mass with varying ambient oxygen concentration are very good. Lindstedt model gives results similar to those of Moss, even if, in general, tends to provide slightly less good variations. It further overestimates the axial position of f_v peak and it does not capture the correct trend of its absolute value increasing oxygen concentration: it decreases when amount of oxygen rises from 15% to 21%, contrary to the experimental trend.

- For what concerns the results of engine simulations, the trend of soot emitted is correct only when small amounts of fuel are delivered in the post-injection. When post-injection consists of more than 5 mg of fuel, soot mass, rather than growing, continues to decrease. Nevertheless, observing the time development of mixture fraction and temperature fields in the cylinder, it seems that the model of soot correctly reacts to the occurring conditions, and the main cause to these wrong results is the too fuel rich mixture that forms during the injection. This is likely due to the lack of experimental data for a correct calibration of the model spray constants for these critical conditions of full load and high-speed engine.

All results show that, as widely discussed in literature, to obtain good predictions for soot, first of all it is essential an extreme accuracy in the modelling of all the complex processes involved in Diesel combustion. Indeed, as it was shown, by using a more accurate combustion model, the multiple RIF model, encouraging results has been obtained. Particularly, the model proposed by Moss has been demonstrated to provide the best results and to react correctly to variations of ambient conditions. Better agreement with experimental data can be achieved by setting the values of the model constants, which is highly recommended for the industrial use of the soot models.

The aforementioned conclusions lead to the following possible future developments of this work:

- the RIF model should be improved in order to properly calculate the ignition delay, which affect the soot on-set time and the heat release of the autoignition. Since chemistry is separately resolved in each flamelet, flamelet interaction might provide better results in terms of chemistry evolutions and all related phenomena. Nevertheless, to date, implemented interaction models do not provide significant improvements respect to the multiple RIF model with no interaction employed in this work. Therefore, developments in this sense are desirable.

- In the context of semi-empirical models, the extremely complex soot kinetics is modelled with few simplified reactions steps, causing likely the underestimation of response to variations of ambient conditions observed. A possible development of semi-empirical soot models analysed is to extend the range of ambient conditions within they are able to accurately predict variations of soot, including some further semi-global step to improve the modelling of complex soot kinetics. Moreover, the flamelet approach applied to soot might been improved in order to overcome the drawback of transportation of soot parcels outside the flame.

- As it was outlined with the engine simulations, spray model should be adjusted in order to provide correct leaner mixture at full-load, high-speed conditions.

List of abbreviations

AHRR	Apparent Heat Release Rate
ASI	After Start of Injection
ASI	After Top Dead Centre
CAD	Crank Angle Degrees
CFD	Computational Fluid Dynamics
CR	Compression Ratio
DAC	Dynamic Adaptive Chemistry
DI	Direct Injection
DIC	Diagonal Incomplete Cholesky
DICI	Direct Injection Compression-Ignited
DICI	Diagonal Incomplete Lower-Upper
DRG	Direct Relation Graph
ECN	Energy Combustion Network
EGR	Exhaust Gas Recirculation
EOA	Ellipsoid Of Accuracy
EOI	End Of Injection
EPFM	Eulerian Particle Flamelet Model
EVO	Exhaust Valve Opening
HACA	H-Abstraction-C2H2-Addition
HCCI	Homogeneous Charge Compression Ignition
IC	Internal Combustion
ID	Ignition Delay
IMEP	Indicated Mean Effective Pressure

ISAT	In-situ Adaptive Tabulation
IVC	Intake Valve Closing
LOL	Lift-Off Length
LTC	Low Temperature Combustion
ODE	Ordinary Differential Equation
OpenFOAM	Open source Field Operation and Manipulation
PAHs	Poly-cyclic Aromatic Hydrocarbons
PBiCG	Pre-conditioned bi-Conjugate Gradient
PCCI	Premixed Charge Compression Ignition
PCG	Pre-conditioned Conjugate Gradient
PDE	Partial Differential Equation
PDF	Probability Density Function
PISO	Pressure Implicit with Splitting Operators
PLII	Planar Laser Induced Incandescence
PM	Particulate Matter
RANS	Reynolds Averaged Navier Stokes
RIF	Representative Interactive Flamelet
ROA	Region Of Accuracy
ROHR	Rates Of Heat Release
ROI	Region Of Interest
RPP	Rated Power Point
SIBS	Semi-Implicit Bulirsch-Stoer
SIMPLE	Semi-Implicit Method for Pressure-Linked Equations
SNL	Sandia National Laboratories
SDR	Scalar Dissipation Rate
TDAC	Tabulation of Dynamic Adaptive Chemistry
TDC	Top Dead Centre
TDRG	Tabulation of Direct Relation Graph

Bibliography

[1] J. B. Moss, C. D. Stewart, and K. J. Young. "Modeling soot formation and burnout in a high temperature laminar diffusion flame burning under oxygen-enriched conditions". In: *Combustion and Flame* 101 (1995), pp. 491–500.

[2] K. M. Leung, R. P. Lindstedt, and W. P. Jones. "A simplified reaction mechanism for soot formation in nonpremixed flames". In: *Combustion and Flame* 87 (1991), pp. 289–305.

[3] H. Bockhorn. *Soot Formation in Combustion: Mechanism and Models*. Ed. by Springer. 1st ed. Berlin, 1994.

[4] S. J. Brookes and J. B. Moss. "Predictions of soot and thermal radiation properties in confined turbulent jet diffusion flames". In: *Combustion and Flame* 116 (1999), pp. 486–503.

[5] Z. Wen et al. "Modeling soot formation in turbulent kerosene/air jet diffusion flames". In: *Combustion and Flame* 135 (2003), pp. 323–340.

[6] L. M. Pickett and Dennis L. Siebers. "Soot in diesel fuel jets: effects of ambient temperature, ambient density, and injection pressure". In: *Combustion and Flame* 138 (2004), pp. 114–135.

[7] J. E. Dec. "A conceptual model of di diesel combustion based on laser-sheet imaging". In: *SAE Technical Papers* (1997).

[8] M. P. B. Musculus, P. C. Miles, and L. M. Pickett. "Conceptual models for partially premixed low-temperature diesel combustion". In: *Progress in Energy and Combustion Science* 39 (2013), pp. 246–283.

[9] F. Brusiani et al. "Influence of Cylindrical, k, and ks diesel nozzle shape on the injector internal flow field and on the emerging spray characteristics". In: *SAE Technical Papers* 1 (2014).

[10] J. M. Desantes et al. "Measurements of spray momentum for the study of cavitation in diesel injection nozzles". In: *SAE Technical Papers* (2003).

[11] J. Kong and C. Bae. "Effect of a conical nozzle orifice on the combustion and emissions in a direct-injection compression ignition engine under low-load conditions". In: *Proceedings of the Institution of Mechanical Engineers, Part D: Journal of Automobile Engineering* 229 (2015), pp. 3–13.

[12] S. Som et al. "Effect of nozzle orifice geometry on spray, combustion, and emission characteristics under diesel engine conditions". In: *Fuel* 90 (2011), pp. 1267–1276.

[13] G. Ferrari. *Motori a combustione interna*. Ed. by Il Capitello. 4th ed. Torino, 2008.

[14] G. Stiesch. *Modeling engine spray and combustion processes*. Ed. by Springer. 1st ed. Berlin, 2003.

[15] S. Rakshit. "High speed flow simulation in fuel injector nozzles". Master thesis. 2012.

[16] S. Singh, Mark P. B. Musculus, and R. D. Reitz. "Mixing and flame structures inferred from OH-PLIF for conventional and low-temperature diesel engine combustion". In: *Combustion and Flame* 156 (2009), pp. 1898–1908.

[17] D. R. Tree and K. I. Svensson. "Soot processes in compression ignition engines". In: *Progress in Energy and Combustion Science* 33 (2007), pp. 272–309.

[18] M. Y. Choi et al. "Simultaneous optical measurement of soot volume fraction and temperature in premixed flames". In: *Combustion and Flame* 99 (1994), pp. 174–186.

[19] D. Siebers, B. Higgins, and L. M. Pickett. "Flame lift-off on direct-injection diesel fuel jets: Oxygen concentration effects". In: *SAE Technical Papers* (2002).

[20] P. Eastwood. *Particulate Emission from Vehicles*. Ed. by John Wiley & Sons Ltd. Chichester, 2008.

[21] I. M. Kennedy. "Models of soot formation and oxidation". In: *Progress in Energy and Combustion Science* 23 (1997), pp. 95–132.

[22] B. S. Haynes and H. G. Wagner. "Soot formation". In: *Progress in Energy and Combustion Science* 7 (1981), pp. 229–273.

[23] M. Frenklach. "Reaction mechanism of soot formation in flames". In: *Physical Chemistry Chemical Physics* 4 (2002), pp. 2028–2037.

[24] D. Bryce et al. "Investigating the effect of oxygenated and aromatic compounds in fuel by comparing laser soot measurements in laminar diffusion flames with diesel-engine emissions". In: *Journal of the Institute of Energy* 72 (1999), pp. 150–156.

[25] H. Richter and J. B. Howard. "Formation of polycyclic aromatic hydrocarbons and their growth to soot: a review of chemical reaction pathways". In: *Progress in Energy and Combustion Science* 26 (2000), pp. 565–608.

[26] B. L. Wersborg, J. B. Howard, and G. C. Williams. "Physical mechanisms in carbon formation in flames". In: *Symposium (International) on Combustion* 14 (1973), pp. 929–940.

[27] S. J. Brookes and J. B. Moss. "Measurements of soot production and thermal radiation from confined turbulent jet diffusion flames of methane". In: *Combustion and Flame* 116 (1999), pp. 49–61.

[28] J. Warnatz and R. W. Dibble U. Mass. *Combustion: physical and chemical fundamentals, modeling and simulation, experiments, pollutant formation*. 2. ed. Berlin: Springer, 1999.

[29] R. N. Kleiveland. "Modelling of Soot Formation and Oxidation in Turbulent Diffusion Flames". Doctoral thesis. 2005.

[30] C. P. Fenimore. "Oxidation of soot by hydroxyl radicals". In: *Journal of Physical Chemistry* 71 (1967), pp. 593–597.

[31] R. Puri, R. J. Santoro, and K. C. Smyth. "The oxidation of soot and carbon monoxide in hydrocarbon diffusion flames". In: *Combustion and Flame* (1994), pp. 125–144.

[32] K. G. Neoh, J. B. Howard, and A.F. Sarofim. "Particulate carbon formation during combustion". In: *Plenum* (1981).

[33] P. F. Flynn et al. "Diesel combustion: An integrated view combining laser diagnostics, chemical kinetics, and empirical validation". In: *SAE Technical Papers* (1999).

[34] S. A. Skeen et al. "Extinction-based Imaging of Soot Processes over a Range of Diesel Operating Conditions". In: *Eight U.S. National Combustion Meeting*. Ed. by University of Utah Western States Section of the Combustion Institute. 2013.

[35] J. E. Dec and D. R. Tree. "Diffusion-flame/wall interactions in a heavy-duty di diesel engine". In: *SAE Technical Papers* (2001).

[36] J. E. Dec and P. L. Kelly-Zion. "The effects of injection timing and diluent addition on late-combustion soot burnout in a di diesel engine based on simultaneous 2-D imaging of OH and soot". In: *SAE Technical Papers* (2000).

[37] D. Siebers and B. Higgins. "Flame lift-off on direct-injection diesel sprays under quiescent conditions". In: *SAE Technical Papers* (2001).

[38] C. Idicheria and L.M. Pickett. "Effect of EGR on diesel premixed-burn equivalence ratio". In: *Proceedings of the Combustion Institute* 31 (2007), pp. 2931–2938.

[39] L. M. Pickett and D. L. Siebers. "An investigation of diesel soot formation processes using micro-orifices". In: *Proceedings of the Combustion Institute*. Vol. 29. 2002, pp. 655–662.

[40] C. A. Idicheria and L. M. Pickett. "Soot formation in diesel combustion under high-EGR conditions". In: *SAE Technical Papers* (2005).

[41] H.K Versteeg and W. Malalasekera. *An introduction to computational fluid dynamics*. Ed. by Pearson Education. Edinburgh, 2007.

[42] N. Peters. "Laminar flamelet concepts in turbulent combustion". In: *Symposium (International) on Combustion* 21 (1988), pp. 1231–1250.

[43] T. Poinsot and D. Veynante. *Theoretical and numerical combustion*. Ed. by Edwards. Philadelphia, 2005.

[44] N. Peters. *Turbulent combustion*. Ed. by Cambridge University Press. Cambridge, 2000.

[45] H. Barths et al. "Simulation of pollutant formation in a gas-turbine combustor using unsteady flamelets". In: *Symposium (International) on Combustion* 2 (1998), pp. 1841–1847.

[46] H. Barths et al. "Simulation of combustion in direct injection diesel engines using a Eulerian particle flamelet model". In: *Symposium (International) on Combustion* 28 (2000), pp. 1161–1167.

[47] H. Pitsch, E. Riesmeier, and N. Peters. "Unsteady flamelet modeling of soot formation in turbulent diffusion flames". In: *Combustion Science and Technology* 158 (2000), pp. 389–406.

[48] N. Peters. "Laminar diffusion flamelet models in non-premixed turbulent combustion". In: *Progress in Energy and Combustion Science* 10 (1984), pp. 319–339.

[49] H. Pitsch, Y. P. Wan, and N. Peters. "Numerical investigation of soot formation and oxidation under diesel engine conditions". In: *SAE Technical Papers* (1995).

[50] G. D'Errico et al. "Comparison of well-mixed and multiple representative interactive flamelet approaches for diesel spray combustion modelling". In: *Combustion Theory and Modelling* 18 (2014), pp. 65–88.

[51] P. A. Tesner et al. "The formation of soot from aromatic hydrocarbons in diffusion flames of hydrocarbon-hydrogen mixtures". In: *Combustion and Flame* 17 (1971), pp. 279–285.

[52] H. Hiroyasu, T. Kadota, and M. Arai. "Developement and use of a spray combustion modeling to predict Diesel engine efficiency and pollutant emissions". In: *Bulletin of the JSME* 26 (1983), pp. 569–575.

[53] I. M. Kennedy, W. Kollmann, and J. Y. Chen. "A model for soot formation in a laminar diffusion flame". In: *Combustion and Flame* 81 (1990), pp. 73–85.

[54] K. J. Young and J. B. Moss. "Modelling sooting turbulent jet flames using an extended flamelet technique". In: *Combustion Science and Technology* 105 (1995), pp. 33–53.

[55] M. Fairweather et al. "Predictions of soot formation in turbulent, non-premixed propane flames". In: *Symposium (International) on Combustion* 24 (1992), pp. 1067–1074.

[56] A. Kronenburg, R. W. Bilger, and J. H. Kent. "Modeling soot formation in turbulent methane-air jet diffusion flames". In: *Combustion and Flame* 121 (2000), pp. 24–40.

[57] D.E. Foster. "Application of a penomenological soot model to Diesel Engine Combustion". In: *Third International Symposyum COMODIA 94*. Ed. by Engine Systems Division of the JSME. 1994.

[58] M. Frenklach and H. Wang. *Detailed mechanism and modeling of soot particle formation*. 1994.

[59] M. Balthasar et al. "Detailed modeling of soot formation in a partially stirred plug flow reactor". In: *Combustion and Flame* 128 (2002), pp. 395–409.

[60] A. Kazakov, H. Wang, and M. Frenklach. "Detailed modeling of soot formation in laminar premixed ethylene flames at a pressure of 10 bar". In: *Combustion and Flame* 100 (1995), pp. 111–120.

[61] F. Mauss et al. *Soot formation in partially premixed diffusion flames at atmospheric pressure*. 1994.

[62] L. Gilyazetdinov. "The kinetic and formation mechanism of carbon black during thermo decomposition of hydrocarbons in the gas phase". In: *Khim. Tverd. Topl.* 3 (1972).

[63] J. B. Moss and C. D. Stewart. "Flamelet-based smoke properties for the field modelling of fires". In: *Fire Safety Journal* 30 (1998), pp. 229–250.

[64] K. J. Syed, C. D. Stewart, and J. B. Moss. "Modelling soot formation and thermal radiation in buoyant turbulent diffusion flames". In: *Symposium (International) on Combustion* 23 (1991), pp. 1533–1541.

[65] J. Nagle and R. F. Strickland-Constable. "Oxidation of carbon between 1000°C and 2000°C". In: Proceedings of the Fifth Conference on Carbon. Pergamon, 1962, pp. 154–164.

[66] K. B. Lee, M. W. Thring, and J. M. Beèr. "On the rate of combustion of soot in a laminar soot flame". In: *Combustion and Flame* 6 (1962), pp. 137–145.

[67] M. Bolla et al. "Modelling of soot formation in a heavy-duty diesel engine with conditional moment closure". In: *Fuel* 117 (2014), pp. 309–325.

[68] M. Bolla et al. "Soot formation modeling of n-heptane sprays under diesel engine conditions using the conditional moment closure approach". In: *Combustion Science and Technology* 185 (2013), pp. 766–793.

[69] Sandia National Laboratories. *ECN wb site*. 2014. URL: `http://www.sandia.gov/ecn/`.

[70] T. Lucchini, G. D'Errico, and D. Ettorre. "Numerical investigation of the spray-mesh-turbulence interactions for high-pressure, evaporating sprays at engine conditions". In: *International Journal of Heat and Fluid Flow* 32 (2011), pp. 285–297.

[71] R. D. Reitz. "Modeling atomization processes in high-pressure vaporizing sprays". In: *Atomisation Spray Technology* 3 (1987), pp. 309–337.

[72] C. Baumgarten. *Mixture formation in internal combustion engines*. Berlin: Springer, 2006.

[73] G. Taylor. "The instability of liquid surfaces when accelerated in a direction perpendicular to their planes". In: *Proceedings of the Royal Society of London A: Mathematical, Physical and Engineering Sciences*. Vol. 201. 1950.

[74] S. Hossainpour and A. R. Binesh. "Investigation of fuel spray atomization in a DI heavy-duty diesel engine and comparison of various spray breakup models". In: *Fuel* 88 (2009), pp. 799–805.

[75] C. S. Lee and S. W. Park. "An experimental and numerical study on fuel atomization characteristics of high-pressure diesel injection sprays". In: *Fuel* 81 (2002), pp. 2417–2423.

[76] OpenFOAM. *OpenFOAM Programmer Guide*. Version 2.2.2. The OpenFOAM Foundation. 2013. URL: `http://foam.sourceforge.net/docs/Guides-a4/ProgrammerGuide.pdf`.

[77] J. H. Ferziger and M. Peric. *Computational methods for fluid dynamics*. Ed. by Springer. Berlin, 1996.

[78] F. Liu et al. "A robust and accurate algorithm of the $\tilde{A}\ddot{Y}$-pdf integration and its application to turbulent methane-air diffusion combustion in a gas turbine combustor simulator". In: *International Journal of Thermal Sciences* 41 (2002), pp. 763–772.

[79] Z. Luo et al. "Development and validation of an n-dodecane skeletal mechanism for spray combustion applications". In: *Combustion Theory and Modelling* 18 (2014), pp. 187–203.

[80] H. J. Curran et al. "A comprehensive modeling study of iso-octane oxidation". In: *Combustion and Flame* 129 (2002), pp. 253–280.

[81] T. F. Lu and C. K. Law. "Strategies for mechanism reduction for large hydrocarbons: n-heptane". In: *Combustion and Flame* 154 (2008), pp. 153–163.

[82] R. Stoer et al. *Introduction to Numerical Analysis*. Ed. by Springer-Verlag. New York, 1980.

[83] T. Lucchini and G. D'Errico. "Diesel combustion simulations in Lib-ICE using the Multiple Representative Interactive Flamelet model". 2013.

[84] S. B. Pope. "Computationally efficient implementation of combustion chemistry using in situ adaptive tabulation". In: *Combustion Theory and Modelling* 1 (1997), pp. 41–63.

[85] T. Lu and C. K. Law. "A directed relation graph method for mechanism reduction". In: *Proceedings of the Combustion Institute*. Vol. 30. 2005, pp. 1333–1341.

[86] L. Liang, J. G. Stevens, and J. T. Farrell. "A dynamic adaptive chemistry scheme for reactive flow computations". In: *Proceedings of the Combustion Institute* 32 I (2009), pp. 527–534.

[87] F. Contino et al. "Coupling of in situ adaptive tabulation and dynamic adaptive chemistry: An effective method for solving combustion in engine simulations". In: *Proceedings of the Combustion Institute* 33 (2011), pp. 3057–3064.

[88] P. Colombi. "Developement and validation of a CFD combustion simulations in Direct Injected Diesel engines based on detailed chemistry and the unsteady diffusion flamelet assumption". Master thesis. 2012.

[89] G. Derrico et al. "Computational fluid dynamics simulation of diesel engines with sophisticated injection strategies for in-cylinder pollutant controls". In: *Energy and Fuels* 26 (2012), pp. 4212–4223.

[90] A. Della Torre et al. "Automatic mesh generation for Diesel Combustion Chamber with OpenFOAM". 2014.

[91] T. Cerri, A. Onorati, and E. Mattarelli. "1D engine simulation of a small HSDI diesel engine applying a predictive combustion model". In: *Proceedings of the Spring Technical Conference of the ASME Internal Combustion Engine Division*. 2006, pp. 371–381.

[92] A. Onorati, G. Ferrari, and G. D'Errico. "1D unsteady flows with chemical reactions in the exhaust duct-system of S.I. engines: Predictions and experiments". In: *SAE Technical Papers* (2001).

[93] G. D'Errico and T. Lucchini. "CFD simulations of RPP and ACP operating points using OpenFOAM® + Lib-ICE: methodology and results." 2011.

[94] F. Contino et al. "Simulations of advanced combustion modes using detailed chemistry combined with tabulation and mechanism reduction techniques". In: *SAE Technical Papers* (2012).

[95] Z. Ren et al. "The use of dynamic adaptive chemistry and tabulation in reactive flow simulations". In: *Combustion and Flame* 161 (2014), pp. 127–137.

[96] S. Singh, R. D. Reitz, and M. P. B. Musculus. "Comparison of the characteristic time (CTC), representative interactive flamelet (RIF), and direct integration with detailed chemistry combustion models against optical diagnostic data for multi-mode combustion in a heavy-duty DI diesel engine". In: *SAE Technical Papers* (2006).

[97] OpenFOAM. *OpenFOAM User Guide*. Version 2.2.2. The OpenFOAM Foundation. 2013. URL: `http://foam.sourceforge.net/docs/Guides-a4/UserGuide.pdf`.

[98] Juan Soulié. *C++ Language Tutorial*. cplusplus.com. 2007. URL: `http://www.cplusplus.com/doc/tutorial`.

[99] P.A Lakshminarayanan and Y. V. Aghav. *Modelling Diesel Combustion*. Ed. by Springer. Berlin, 2010.

[100] C. Hasse. "A Two-Dimensional Flamelet Model for Multiple Injections in Diesel Engines". Doctoral thesis. 2004.

[101] T. Lucchini et al. "Modeling internal combustion engines using the OpenFOAM® library". In: *Second OpenFOAM User Conference*. Ed. by ESI-OpenCFD. Berlin, 2014.

[102] G. D'Errico et al. "Diesel Engine Simulation with Tabulation of Dynamic Adaptive Chemistry and Adaptive Local Mesh Refinement". In: *International Multidimensional Engine Modeling User's Group Meeting*. Ed. by SAE Congress. Detroit, 2010.

[103] T. Lucchini and G. D'Errico. "Simulation od Diesel engine combustion using the Characteristic Time-Scale model with OpenFOAM® and Lib-ICE". 2013.

[104] T. Lucchini. "Representative Interactive Flamelet model (RIF): current state of the implementation in Lib-ICE". 2014.